5-24-2012

Studies of Lung Micromechanics via Hyperpolarized 3He Diffusion NMR

Adam Hajari
Washington University in St. Louis

WASHINGTON UNIVERSITY IN SAINT LOUIS

Department of Physics

Dissertation Examination Committee:
Jason Woods, Chair
Mark Conradi
Dmitriy Yablonskiy
James Miller
James Buckley
Sophia Hayes

Studies of Lung Micromechanics via Hyperpolarized ^{3}He Diffusion NMR

by

Adam James Hajari

A dissertation presented to the
Graduate School of Arts and Sciences
of Washington University in
partial fulfillment of the
requirements for the degree
of Doctor of Philosophy

May 2012

Saint Louis, Missouri

Abstract

While high quality MR Images of lungs are difficult to obtain with conventional proton MRI due to the organ's low tissue density, the advent of techniques in noble gas polarization have enabled MR investigations of the lung's more abundant air space rather than its tissue. In addition to high-resolution images of lung ventilation, lung morphometry via gas diffusion NMR provides information about the size and shape of the microscopic airways that account for over 95% of the lung's airspace. Consequently, gas diffusion NMR provides an important new tool for investigating changes in lung microstructure during macroscopic changes in lung volume.

Despite decades of research into the mechanisms of lung inflation and deflation, there is little consensus about whether macroscopic changes in lung volume occur due to changes in the size and/or shape of alveoli and alveolar ducts or by alveolar recruitment and derecruitment. In this dissertation lung morphometry is performed via ^{3}He diffusion MRI in order to measure the average alveolar depth and alveolar duct radius at multiple levels of both inspiration and expiration in *in vivo* human subjects and in explanted human and canine lungs. Average alveolar volume, surface area, and the total number of alveoli at each lung volume are calculated from the ^{3}He morphometric parameters. The results suggest that human lungs inflate/deflate primarily by recruitment/derecruitment of alveoli, and that individual alveolar ducts in both human and canine lungs increase in volume non-isotropically by accordion-like extension. The results further suggest that this change in alveolar duct volume is the primary mechanism of lung volume change in canine lungs but is secondary to alveolar recruitment/derecruitment in humans.

Acknowledgments

Many thanks to all of the people who have aided in this work and who have helped me during my time as a graduate student. My advisor, Jason Woods, provided patient guidance, thoughtful discussions, and was a constant source of motivation for moving this project forward. This work would not have been possible without his help. Mark Conradi has been a fountain of knowledge for all things physics and I am grateful to him for taking me into his lab early in my graduate career. I owe a great debt to my colleagues in the Department of Radiology. The core principles of this thesis are built upon work done by Dmitriy Yablonskiy and Alex Sukstanskii. Both men spent many patient hours looking over data with me and helping with the development a canine specific morphometric model. Jim Quirk, Yulin Chang, and Michelle Milne provided an immense amount mentoring throughout my time at Washington University, particularly early on when it was most needed.

Contents

List of Figures

List of Tables

Chapter 1: Introduction and Background

1.1 Introduction

The lung is composed of millions of small airways known as alveolar ducts, acting in concert during inspiration and expiration to affect macroscopic changes in total lung volume. While there is scientific consensus regarding the architecture of the lung and the approximate structure of its airways, the mechanisms of lung inflation and deflation at the fundamental pulmonary unit, the alveolar duct, remains poorly understood. Despite over fifty years of research into the topic, there is still no consensus about whether lung inflation occurs due to changes in the size and/or shape of alveoli and alveolar ducts or by the recruitment of new alveoli.

Much of what is known about lung microstructure comes from histological studies of lung tissue. In these studies, lungs are frozen or fixed at a static level of inflation prior to processing for histological assessment. A disadvantage to histological studies is that the tissue suffers from alteration during the fixation process. This, and the inability to reproduce the same measurements at different states of inflation/deflation in the same lung are significant limiting factors when studying lung dynamics. Additionally, interpretations of the results of histological studies can also be unclear. Macklem (35) points out that plots of surface area versus total lung volume from two different histology studies by Forrest (20) and Dunnill (15) could both be explained equally well by either isotropic expansion of alveolar ducts or alveolar recruitment. Another common technique for studying lung mechanics is subpleural microscopy. This technique is usually performed *in vivo*, but is limited to measurements of airways at the lung periphery which may behave differently from those in the bulk of the lung (2, 9). In addition, both methods sample only a small subset of total

alveoli and require inferences of a complex three-dimensional structure from a two-dimensional measurement. Furthermore, neither method is suitable for *in-vivo* studies of human lungs.

In recent years pulmonary MRI experiments employing hyperpolarized gases such as ^{3}He (11, 22, 27, 46, 49, 57, 65, 68) and ^{129}Xe (38, 44, 45) have proven important tools for performing non-invasive quantitative studies of lung microstructure. ^{3}He lung morphometry has been validated by comparison with histological measurements in humans (65, 68), mice (43, 62), and dogs (26), and has been used to quantitatively characterize changes in lung microstructure at various stages of emphysema in human subjects (48). As a tool for studying lung micromechanics, ^{3}He lung morphometry is advantageous because it takes into account three-dimensional structure, samples all ventilated parts of the lung, and is spatially resolved. The technique employs a multiple b-value (multiple gradient strength) ^{3}He diffusion MR experiment to measure anisotropic diffusion of hyperpolarized ^{3}He within alveolar ducts in images that cover the entire lung. Based on established relationships between anisotropic diffusion of helium within acinar airways and the alveolar duct geometry (57, 68), average values of alveolar duct radii, R, and alveolar depth, h, are obtained for the airways within each voxel of the MR image (Figure 1.6). The results can be used to calculate the average surface area and volume of individual alveoli as well as the total number of alveoli (68). Furthermore, these experiments are safe and suitable for *in-vivo* studies in humans (34).

In this dissertation ^{3}He lung morphometry is employed to study the micromechanics of lung deflation in explanted canine and human lungs and inflation and deflation micromechanics in *in vivo* human subjects. The ^{3}He lung morphometry results from the

canine lungs are supplemented with histological measurements of the same parameters measured via gas diffusion MR in order to demonstrate the suitability of ^{3}He lung morphometry for studying lung micromechanics.

The remainder of Chapter 1 provides a brief introduction to nuclear magnetic resonance (NMR) (particularly diffusion NMR and magnetic resonance imaging), noble gas polarization, and lung architecture. Chapter 2 provides details on the development and use of the mathematical morphometric models employed in ^{3}He lung morphometry. These mathematical models relate the MR diffusion data to precise alveolar geometric parameters, which are used to calculate alveolar volume, alveolar surface area, and the total number of alveoli. Chapter 3 introduces several well-established theories of lung micromechanics and discusses the findings and conclusions of past morphometric studies as they relate to the different theories for lung micromechanics. The theories of lung micromechanics introduced in Chapter 3 provide the context for interpreting the ^{3}He lung morphometry results. Chapter 4 provides details about the hyperpolarization and gas delivery equipment, the MR scanners and hardware, and ventilation systems used in the ^{3}He MR diffusion experiments. Chapter 5 describes the experimental methods. The experimental results are presented in Chapter 6 and the implications of these results to lung micromechanics are discussed in Chapter 7.

1.2 Nuclear Magnetic Resonance

Nuclear magnetic resonance (NMR) describes the interactions between an ensemble of nuclei with non-zero spin angular momentum and external magnetic fields. Spin is an inherently quantum mechanical property, and thus a thorough discussion of NMR requires a quantum mechanical description of spin dynamics. The goal of this section, however, is to

provide a *brief* description of the fundamentals of NMR, and for this purpose a classical description, or "vector model", of spin dynamics is better suited. For a more thorough handling of the topics covered in this section see references (8, 17, 21, 28, 52). In particular, references (32, 52) provide very good quantum mechanical development of fundamental topics in NMR.

1.2.1 Nuclear Spin, Magnetic Moment, and Precession

A nucleus with non-zero spin angular momentum, I, also possesses a non-zero nuclear magnetic moment, μ, proportional to its spin

$$\boldsymbol{\mu} = \gamma \boldsymbol{I} \qquad 1.1$$

where the proportionality constant, γ, is the nucleus's gyromagnetic ratio. As with nuclear charge and nuclear mass, the ground state nuclear spin and gyromagnetic ratio are both physical constants intrinsic to a particular combination of constituent protons and neutrons. The net magnetic moment, M, for a sample consisting of an ensemble of nuclei is the sum of all of the individual magnetic moments. Because a large collection of randomly oriented spins will lead to full cancelation of the net spin, the net magnetic moment for most collections of nuclei is zero.

In the presence of an external magnetic field a nucleus experiences a torque due to the external field's interaction with the nucleus's magnetic moment. This torque and the spin angular momentum together result in a precession of the moment about the external field. If the external field has magnitude B_0, then the moment precesses with angular frequency

$$\omega_0 = \gamma B_0 \qquad 1.2.$$

A full 2π precession of the moment sweeps out a cone of constant angle θ relative to B_0. For a nucleus with magnetic moment, μ, θ is initially given by the angle between μ and B_0 just after B_0 is turned on. Thus, again, the net moment from an ensemble of spins just after the external field is turned on is zero since each moment's phase and angle relative to B_0 are random. However, in addition to precession of μ about B_0, the presence of an external field also leads to a splitting of the ground state energy into $2I+1$ non-degenerate levels. For spin $I = 1/2$ (the most common value of ground state spin studied by NMR), there are two energy levels which are commonly referred to as spin-up and spin-down. For a spin-1/2 nucleus with gyromagnetic ratio γ in an external field B_0, the difference between the two energy levels is:

$$\Delta E = \hbar\omega_0 = \gamma\hbar B_0. \qquad 1.3$$

where $\hbar$ is Planck's constant divided by 2π. At room temperature the lower of these two energy states is slightly more energetically favorable resulting in an unequal distribution between the two states for a system at equilibrium. The ratio of the population of spins in the low energy state to the population in the high energy state is given by the Boltzmann distribution

$$\frac{N_{low}}{N_{high}} = e^{\frac{\gamma\hbar B_0}{kT}} \qquad 1.4$$

where k is Boltzmann's constant and T is the temperature. At high temperatures ($kT \gg \gamma\hbar B_0$) the relative difference in the number of spins in each state (known as the ensemble's polarization) is approximately:

$$\frac{N_{low}-N_{high}}{N_{low}+N_{high}} \approx \frac{\gamma\hbar B_0}{2kT} \qquad 1.5.$$

As an example, consider a sample of water (H_2O) in a 1.5 T magnetic field. ^1H is a spin-1/2 nucleus with a gyromagnetic ratio of 42.58(2π) MHz/T. In a 1.5 T field, the precession frequency is $\omega_0/2\pi$ = 63.86 MHz (radio frequency), and, at room temperature, the relative difference in the number of nuclei in the spin-up and spin-down states is about 5 ppm. That is, for every 200,000 ^1H nuclei, only one nucleus contributes to the ensemble's net magnetic moment. It is clear that it is only by the high density of nuclei in solids and liquids (about Avogadro's number in a 10mL sample of water) that such a net magnetic moment is detectable at all.

1.2.2 Relaxation Times

As stated above, just after an external magnetic field is turned on, the net magnetic moment of a collection of spin-1/2 nuclei is zero. The system starts in a non-equilibrium state and the transition to Boltzmann's equilibrium is characterized by a longitudinal relaxation time constant, T_1. The net magnetic moment for a sample in an external field initially having no longitudinal magnetization is described by:

$$M(t) = M_0[1 - exp(-t/T_1)] \quad 1.6$$

where M_0 is the sample's net magnetic moment at equilibrium and t is the duration of time after the external field is turned on.

Eq. 1.6 describes longitudinal relaxation of a sample starting with no net magnetic moment, but longitudinal relaxation can be described more generally by the equation

$$M(t) = M_0[1 - A\ exp(-t/T_1)] \quad 1.7,$$

where the constant A depends on the initial state of the spins. Through a process known as hyperpolarization (described in section 1.4), it is possible to "pump" spins from their high

energy state to their low energy state creating a difference in the number of spin-up and spin-down nuclei far exceeding Boltzmann's equilibrium. In the case of a sample starting in a hyperpolarized state, A is a negative constant with its magnitude dependent on the level of polarization. Hyperpolarization is commonly employed in NMR of gases in order to overcome the challenges associated with their low spin density.

A sample's longitudinal magnetic moment at equilibrium is, for all practical purposes, undetectable. It is orders of magnitude smaller than typical diamagnetic contributions and many many orders of magnitude smaller than the external field that brought it into being. In order to detect a sample's nuclear magnetic moment that moment must first be rotated into the plane transverse to the external field. This is achieved by applying a magnetic field oscillating at the nuclei's precession frequency (generally radio frequency) in a direction transverse to the external field. A radio frequency (rf) pulse, applied to a sample in equilibrium in a direction transverse to B_0, "flips" the magnetic moment of the sample away from the longitudinal axis of the external field and toward the transverse plane. The flip angle is determined by the rf pulse's magnitude and duration. After a flip angle, α, a sample's moment has a transverse component equal to $M\sin(\alpha)$ and longitudinal component equal to $M\cos(\alpha)$, where M is the sample's net magnetic moment at equilibrium.

Once in the transverse plane, the net moment precesses about the external field creating an oscillating magnetic field of its own, which is detected by an rf receiver. In practice, the rf transmitter and receiver are often integrated into a single LC circuit, known as the rf coil, tuned to the precession frequency, γB_0.

Up to this point it has been assumed that the external magnetic field across the sample is a constant, B_0. In reality, the magnetic field seen from one spin to next is inhomogeneous due to field contributions from neighboring spins. That is, the actual field experienced by some nucleus i is $B_i = B_0 + \epsilon_i$, giving it a precession frequency

$$\omega_i = \gamma B_i = \omega_0 + \gamma\epsilon_i \qquad 1.8.$$

ϵ_i is the field contributions from neighboring spins in the directions of B_0. ϵ_i is a random variable that will be positive or negative with equal probability. Through a process called dephasing, the net moment in the transverse plane decays to zero as spins in a higher field speed up and spins in a lower field slow down relative to ω_0. For a sample at equilibrium in an external field pointing in the z-direction, the magnetic moment in the transverse plane immediately after an rf pulse that flips the moment towards the x-axis is given by

$$M_x(t) = M_{0t}\cos(\omega_0 t)\exp(-t/T_2) \qquad 1.9$$

$$M_y(t) = M_{0t}\sin(\omega_0 t)\exp(-t/T_2) \qquad 1.10$$

where M_{0t} is the transverse magnetization immediately following the rf pulse ($t = 0$). The inverse of the exponential rate constant, T_2, is referred to as the transverse relaxation time. Eqs. 1.6, 1.9, and 1.10 are formally obtained by solving the set of differential equations introduced by Bloch (7), which describe the time evolution of a sample's macroscopic magnetic moment in the presence of one or more external fields. For the sake of convenience, spin dynamics are often represented in a reference frame that rotates at the spins' precession frequency, ω_0, such that a magnetic moment flipped toward the x-axis is given by:

$$M_x(t) = M_{0t}\exp(-t/T_2) \qquad 1.11$$

$$M_y(t) = 0 \qquad 1.12$$

The signal collected by the rf receiver immediately following an rf pulse is called the Free Induction Decay (FID). For an ensemble of isochromatic spins precessing in the rotating reference frame, the FID is simply the decaying exponential of Eq. 1.11. In a non-rotating reference frame, there will be a sinusoidal contribution to the FID as in Eq. 1.9 and Figure 1.1. In general, a Fourier transform of the FID gives the sample's distribution of spin frequencies. The Fourier transform of the FID from a nearly isochromatic sample gives a Lorentzian with height proportional to M_{0t} and FWHM proportional to $1/T_2$ that peaks at the precession frequency ω_0.

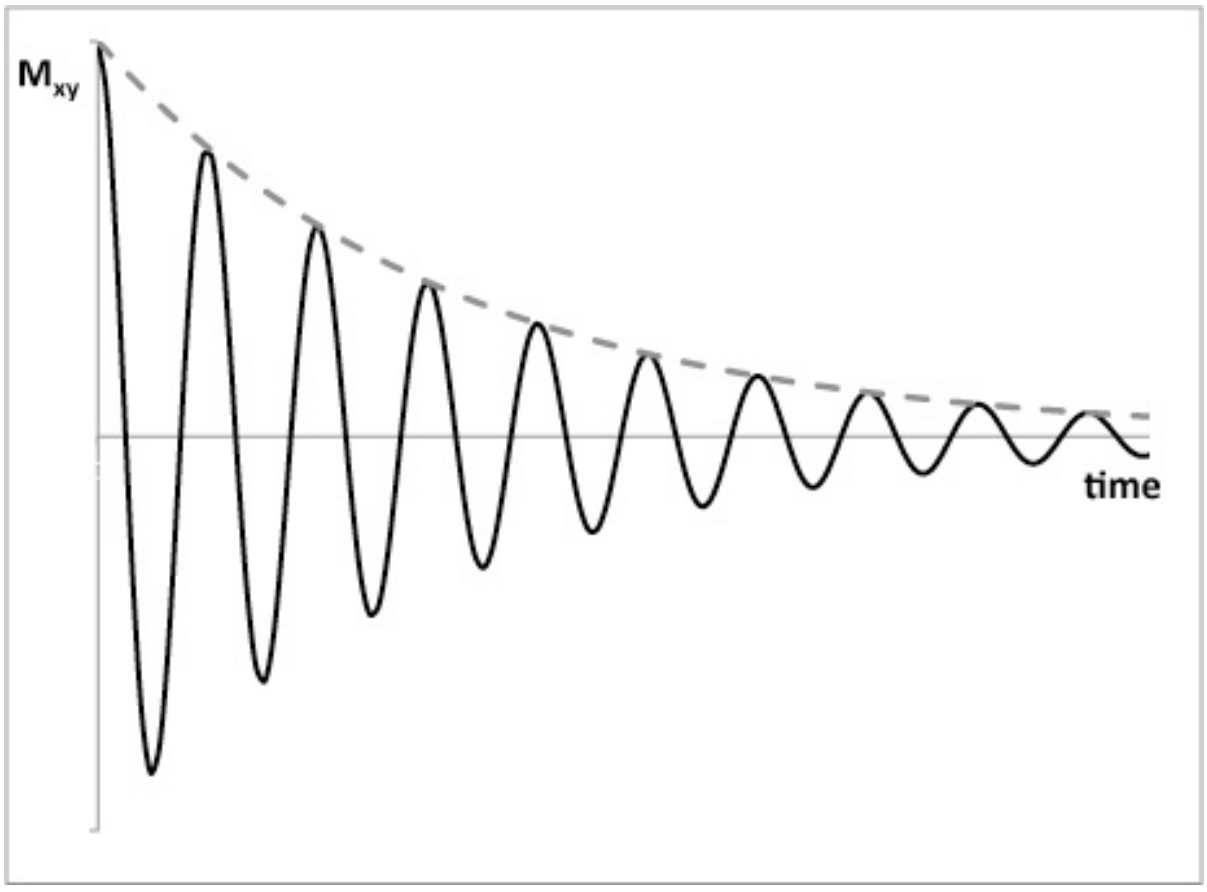

Figure 1.1: Sketch of a Free Induction Decay (FID) acquired from an isochromatic sample. The FID is given by Eq. 1.11 as seen in the rotating reference frame (dashed line) and by Eq. 1.9 for an off-resonance reference frame (solid line).

In practice, the FID decays at a rate faster than $1/T_2$, due to magnetic field inhomogeneities inherent to the source of the external field. The FID in the presence of an inhomogeneous external field is still characterized by Eqs. 1.9 – 1.12, but with a faster decay rate of $1/T_2^*$ rather than $1/T_2$. T_2^* characterizes the dephasing of the spins due to local inhomogeneities caused by neighboring spins *and* global field inhomogeneities due to an imperfect B_0 field.

1.2.3 Magnetic Field Gradients

Just as the $\gamma\epsilon_i$ contribution from neighboring moments in Eq. 1.8 results in a distribution of precession frequencies, any spatially dependent field added to B_0, also leads to a distribution, or "fanning out", of precession frequencies. Magnetic field gradients are often intentionally employed in NMR experiments in order to spatially encode spins within a sample. This spatial encoding is the foundation of Magnetic Resonance Imaging and NMR diffusion experiments.

A linear field gradient results in a magnetic field with a linear dependence on position. For instance, a gradient in the x-direction, G_x, when applied to a uniform field, B_0, results in the spatially dependent magnetic field

$$B(x) = B_0 + xG_x \qquad 1.13,$$

and, from Eq. 1.2, a spatially dependent precession frequency

$$\omega(x) = \omega_0 + x\gamma G_x \qquad 1.14.$$

If a field gradient is turned on immediately following an rf-pulse, the resulting FID decays very rapidly as the spins' precessions quickly dephase due to the gradient term in Eq. 1.14. If

a second gradient of equal magnitude and duration but opposite sign (see Figure 1.2) is turned on after the first is turned off, the spins will come back into phase essentially resulting in a delayed FID. This delayed FID, known as a gradient echo, results from the application of two bipolar magnetic field gradients.

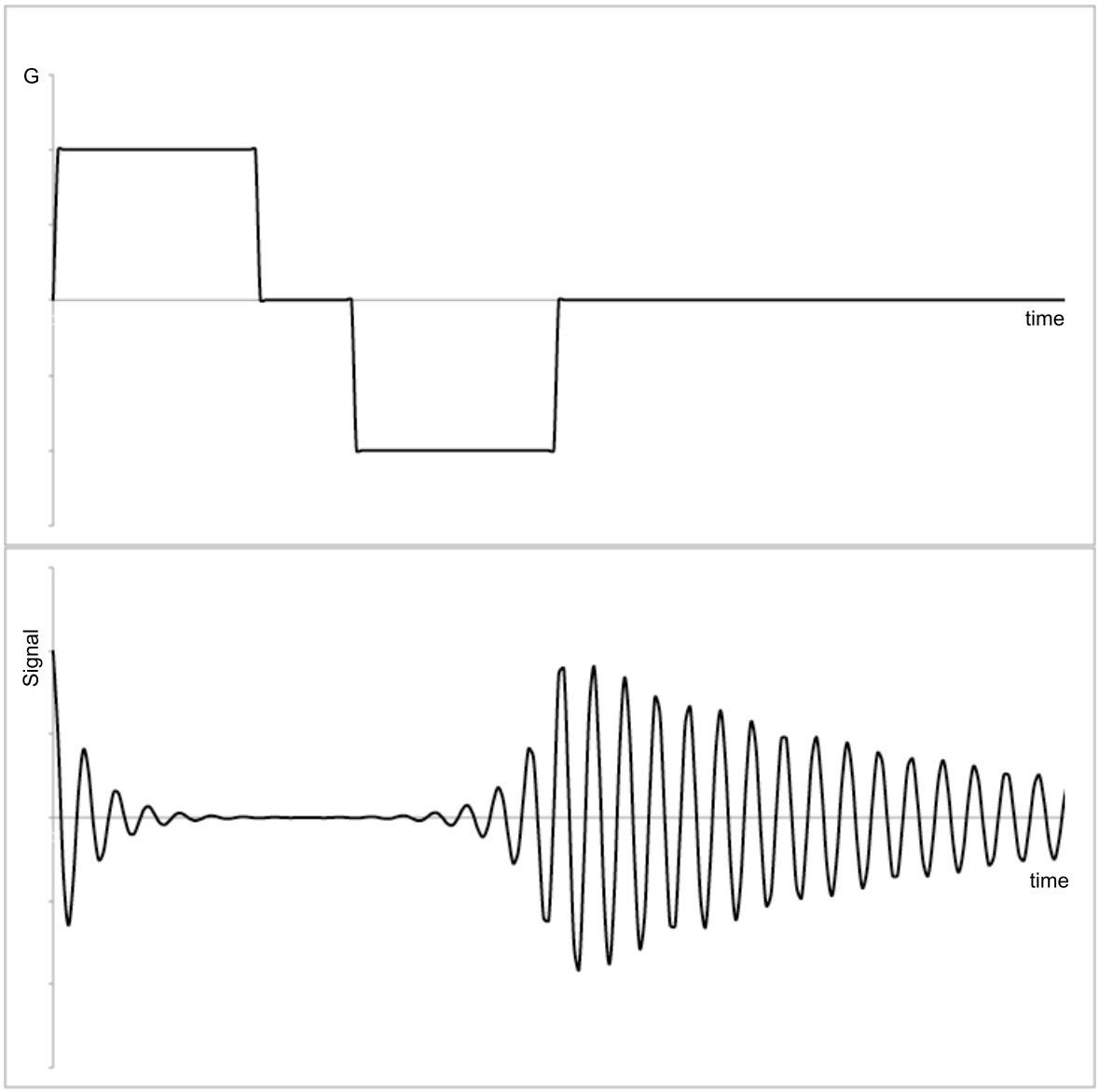

Figure 1.2: Square bipolar gradient pulse (top) and resulting gradient echo (bottom).

1.2.4 Magnetic Resonance Imaging

Unlike the isochromatic FID in Figure 1.1, the FID for an ensemble of spins on resonance with γB_0 and in the presence of a field gradient, G, across the sample is composed of a distribution of frequencies in the range of $\omega_L = x_L \gamma G$ and $\omega_R = x_R \gamma G$ where x_L and x_R are the left and right most boundaries of the sample. In general, in the presence of a field gradient, G, a nucleus's location is related to its precession frequency, ω by

$$x = \omega / \gamma G \qquad 1.15.$$

Thus, a Fourier transform of such an FID provides, not only a distribution of the spins' precession frequencies, but also a distribution of the spins' positions. This technique of spatial encoding is known as frequency encoding and results in a one-dimensional projection of spin density for an isotropic sample. In practice, a gradient of equal magnitude, opposite direction, and half the duration precedes the frequency encoding gradient and the FID is collected from a gradient echo (see Figure 1.4).

As a simple example, consider two test tubes of equal inner diameter each containing an ensemble of moments precessing with angular frequency ω. Suppose that the long axes of the tubes are parallel to the external field, and that the tubes are located at positions x_1 and x_2 along the x-axis. The Fourier transform of the FID acquired during a frequency encoding gradient, G, in the x-direction, results in two peaks, one at $\omega_1 = x_1 \gamma G$ and a second at $\omega_2 = x_2 \gamma G$. The peaks' widths are proportional to the test tubes' inner diameter and the peaks' heights are proportional to the number of resonant nuclei in each of the tubes. For instance, if the test tube located at position x_1 is filled to twice the volume as the test tube located at position x_2, and the two samples are of equal density, the peak at ω_1 will be twice as tall as the peak at ω_2.

A two-dimensional image is created with spatial encoding in a direction orthogonal to the frequency encoding direction. This is accomplished by applying a phase encoding gradient orthogonal to and immediately preceding the frequency encoding gradient. The gradient echo resulting from this sequence of gradient pulses constitutes a single line of k-space. A full two-dimensional k-space image is composed of multiple lines of k-space (typically 40, 64, 128, or 256 depending on the desired resolution of the corresponding real-space image) each collected with a different strength phase-encoding gradient (see Figure 1.4). The frequency encoding direction is typically referred to as the read out direction. A 2D Fourier transform is applied to the k-space image in order to obtain the corresponding real-space image.

The thickness and location of the two-dimensional image along the direction of the third orthogonal direction is determined by a third gradient orthogonal to the imaging plane and a slice-selective rf-pulse [see Ref. (32)]. A diagram of all three gradients, the rf-pulse, and the resultant echo is shown in Figure 1.4.

1.3 MR Diffusion

Consider a spin-1/2 nucleus with magnetic moment parallel to an external field $B_0\hat{z}$ at position x_1 along the x-axis. If after an rf pulse, an x gradient of magnitude G is turned on for a duration δ, the precessing moment acquires a phase of $\phi_1 = x_1\gamma G\delta$. If the nucleus then moves to position x_2 and a second gradient of equal magnitude but opposite direction is turned on for the same duration τ, the spin acquires an additional phase of $\phi_2 = -x_2\gamma G\delta$, giving it a net accumulated phase of

$$\phi = (x_1 - x_2)\gamma G\delta \qquad 1.16.$$

For an ensemble of spins, the mean squared phase is

$$\langle\phi^2\rangle = \langle(x_1 - x_2)^2\rangle\gamma^2G^2\delta^2 \quad 1.17.$$

Notice that stationary spins ($x_1 = x_2$) acquire no net phase after the pair of bipolar gradient pulses. Put another way, the dephasing that occurs during the first gradient pulse is perfectly rephased during the second for stationary spins. This is the cause of the gradient echo discussed in the section 1.2.3.

In samples where nuclei undergo translational motion (by either diffusion or flow), the ensemble's non-zero mean squared displacement results in an imperfect rephasing of spins and an attenuation of the gradient echo amplitude. The self diffusion coefficient over diffusion time Δ is given by the equation (6)

$$D = \langle(x_1 - x_2)^2\rangle/(2\Delta) \quad 1.18,$$

and Eq. 1.17 can be rewritten in terms of this diffusion coefficient as

$$\langle\phi^2\rangle = 2\gamma^2G^2\delta^2\Delta D \quad 1.19.$$

The above example illustrates the effect of diffusion on an ensemble's phase and, consequently, the gradient echo amplitude. Note that the diffusion coefficient in Eq. 1.18 is only for one-dimensional diffusion in the direction of the gradient pulse and also that this derivation is specific to cases where the gradient pulse width is much smaller than the separation of the pulses ($\delta \ll \Delta$).

A general solution for signal attenuation due to a bipolar diffusion gradient of arbitrary shape can be derived by solving the Bloch equations with an additional diffusion term (54, 58). In the rotating reference frame and in the case of isotropic diffusion, the equation of motion for the complex transverse magnetization vector $M_+ = M_x + iM_y$ is

$$\frac{\partial M_+(\boldsymbol{r},t)}{\partial t} = -i\gamma\boldsymbol{r}\cdot\boldsymbol{G}(t)M_+(\boldsymbol{r},t) - \frac{M_+(\boldsymbol{r},t)}{T_2} + D\nabla^2M_+(\boldsymbol{r},t) \quad 1.20,$$

where ***G(t)*** is a time dependent magnetic field gradient. Under the condition of free diffusion during a balanced bipolar gradient, the solution to the above equation is

$$M_+(\boldsymbol{r}, t) = M_0 e^{-t/T_2} e^{-i\boldsymbol{r}\cdot\boldsymbol{k}(t)} e^{-bD} \quad 1.21$$

where M_0 is the unattenuated net magnetization,

$$k = \gamma \int_0^t \boldsymbol{G}(t')\, dt' \quad 1.22,$$

and

$$b(t) = \gamma^2 \int_0^t \left(\int_0^{t'} G(t'')dt'' \right)^2 dt' \quad 1.23.$$

At a fixed echo time (TE), the NMR signal obtained from the gradient echo can be expressed as

$$S = S_0 e^{-bD} \quad 1.24.$$

S_0 is proportional to the $M_0 e^{(-TE/T2)}$ term from Eq. 1.21, while the $e^{-i\mathbf{r}\cdot\mathbf{k}(t)}$ term in Eq. 1.21 is related to the moment's precession in transverse plane and does not affect the echo signal amplitude (8).

A realistic gradient pulse requires some finite amount of time to "ramp" up to its maximum value and "ramp" back down to zero. For a trapezoidal gradient pulse, $G(t)$, with ramp time, τ, pulse duration δ, pulse separation Δ, and maximum gradient strength, G_m, (see Figure 1.3), Eq. 1.23 gives

$$b = \gamma^2 G_m{}^2 \left[\delta \left(\Delta - \frac{\delta}{3} \right) + \tau \left(\delta^2 - 2\Delta\delta + \Delta\tau - \frac{7}{6}\delta\tau + \frac{8}{15}\tau^2 \right) \right] \quad 1.25.$$

Notice that the parameter b depends on the gradient timing parameters and is proportional to the square of the gradient strength, G_m. The pulse separation, Δ, is referred to as the diffusion time. In the case of free diffusion, an experimental value for a molecules self-diffusion coefficient, D, can be obtained by performing a gradient echo experiment with two or more b-values, and then fitting Eq. 1.24 to the resulting signal attenuation.

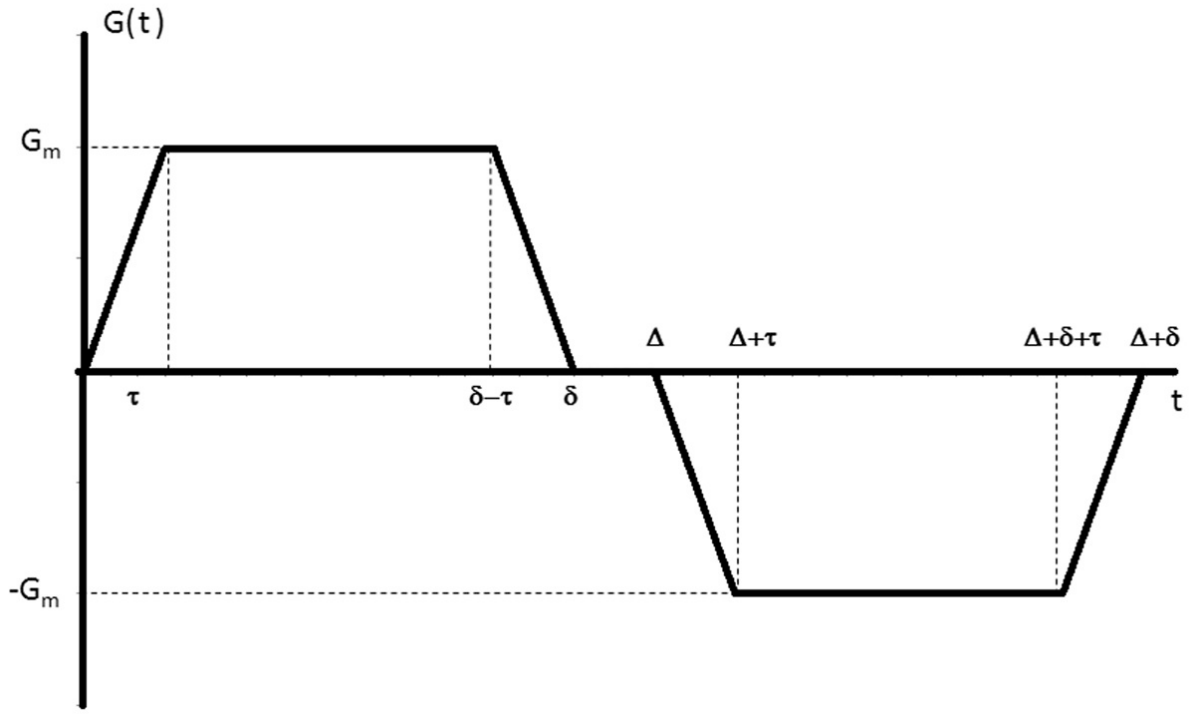

Figure 1.3: Trapezoidal bipolar diffusion gradient.

Eq. 1.20 is specific to a sample under the condition of isotropic, or "free", diffusion. The more general form of Eq. 1.20 for non-isotropic molecular motion does not have a closed form solution. Nevertheless, the gradient echo experiment using Eq. 1.24 is still useful in quantifying non-isotropic diffusion in restricted mediums such as the lung. In cases of restricted diffusion, the diffusion coefficient obtained by fitting Eq. 1.24 to the signal-attenuated data is commonly referred to as the apparent diffusion coefficient (*ADC*). For diffusion of an ensemble of spins with a free diffusion coefficient D_0, within a structure of characteristic length scale, l, a gradient echo pulse sequence with a diffusion time on the order of $\Delta = l^2/2D_0$, provides an *ADC* values which can be used to characterize the "openness" of the medium of interest (41).

Studies of gas diffusion within lungs at various stages of emphysema have shown that simple 2b *ADC* measurements correlate with other, more direct, methods of characterizing tissue destruction such as histology (26, 48, 65, 68). Combined with Magnetic Resonance Imaging, MR measurements of gas diffusion within the lung provide a regionally specific, statistically powerful, and non-invasive method of obtaining structural information at a length scale inaccessible by conventional MRI. The entire gradient echo diffusion imaging pulse sequence is shown in Figure 1.4.

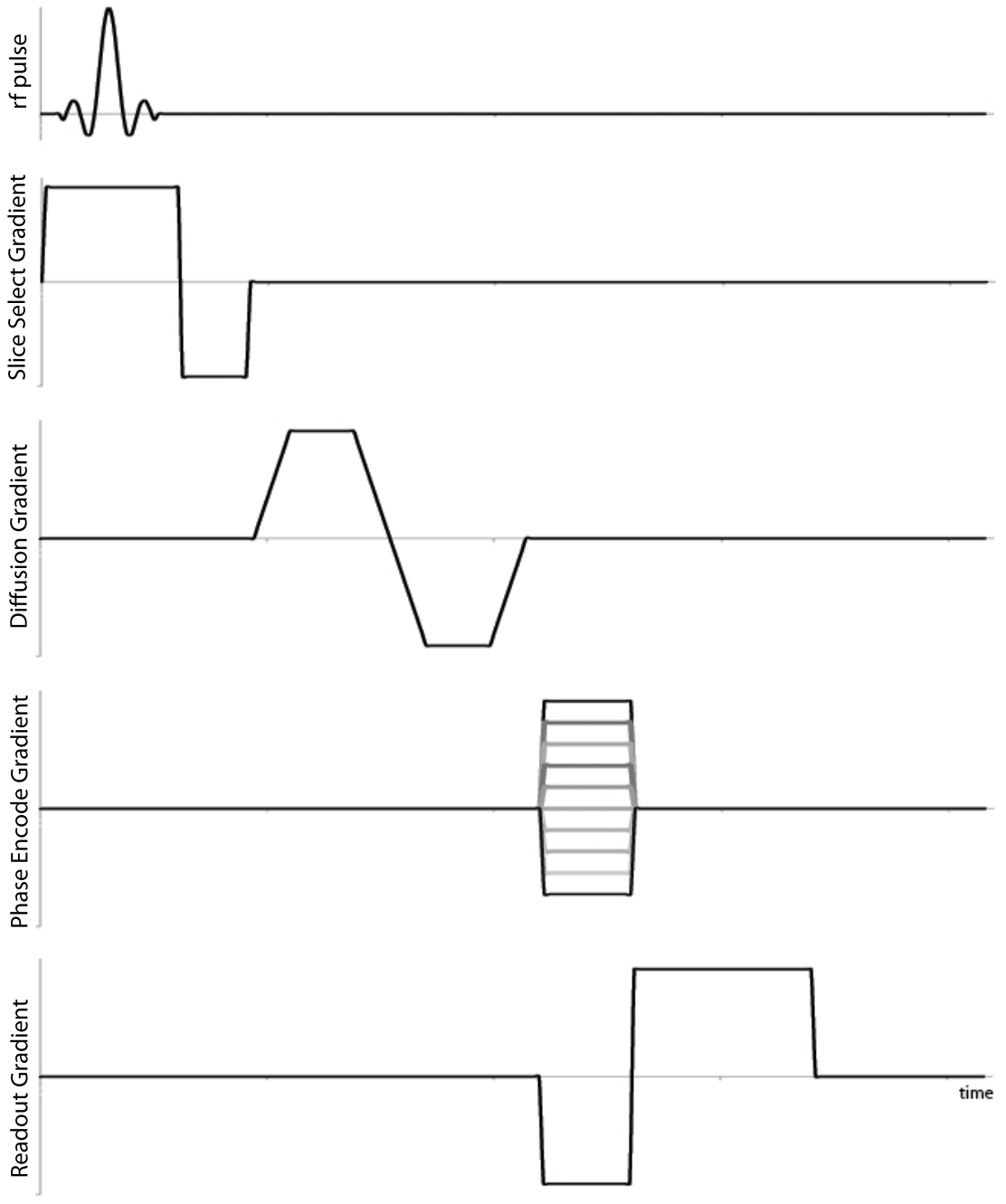

Figure 1.4: Diffusion MR Imaging pulse sequence. A slice selective rf pulse is applied during a the slice select gradient. The bipolar diffusion sensitizing gradient is shown in greater detail in Figure 1.3. Each line of k-space is acquired with a different magnitude phase encode gradient and the gradient echo is acquired during the readout (or frequency encoding) gradient.

1.4 Noble Gas Polarization

NMR, which obtains signal from approximately one in every million nuclei, is, in most cases, an insensitive tool. It is only by virtue of the high water content of human tissue that Magnetic Resonance is of such utility in the field of medicine. However, a tissue sparse organ such as the lung does not provide sufficient MR signal to perform useful studies via traditional MRI. At functional levels of inflation the lung is only about 20% tissue by volume (3). In addition to low ^{1}H density, the numerous air/tissue interfaces lead to high magnetic susceptibility gradients, which decrease T_2^*, thus decreasing the effective NMR signal to noise ratio (SNR).

A revolution in pulmonary MR research followed closely behind the development spin-exchange optical pumping (SEOP), a method of increasing the polarization of spin-1/2 noble gases by up to 5 orders of magnitude (61). This increase in polarization of a gas more than compensates for signal deficiency due to low spin density (compared to tissue and liquids), allowing for NMR and MRI studies of the lung's much more abundant airspace rather than its tissue. Hyperpolarized gas NMR has the additional benefit of allowing for studies of lung microstructure using the diffusion MRI sequence discussed in section 1.3 (and developed further in Chapter 2).

SEOP is a two-step process. Alkali-metal valence electrons receive spin angular momentum from circularly polarized light. That angular momentum is then passed to a spin-1/2 noble gas nucleus by collision. The entire process occurs within a magnetic field in order to induce Zeeman splitting of the spin-up and spin-down states in both the alkali metal electrons and the spin-1/2 nuclei.

While SEOP can occur with any alkali metal, Rb is often chosen because its $5s_{1/2}$-$5p_{1/2}$ transition occurs at 794.7 nm, an electromagnetic wavelength accessible by low cost, high power diode laser arrays (10, 30). Furthermore, Rb, which must be in its gas phase during SEOP, has a high vapor pressure allowing for SEOP to occur at temperatures which are non-destructive to the glass polarizing cell (61).

Using σ+ circularly polarized light, the $\Delta m_s = 1$ quantum selection rule limits the Rb electron excitation to transitions from the m = -1/2 (spin-down) state to the m = +1/2 (spin-up) state. Through collisional mixing, electrons fall back to either the m = -1/2 or m = +1/2 ground state with near equal probability, but because only the m = -1/2 ground state is depopulated by the circularly polarized light, once an electron finds its way to the m = +1/2 ground state, it is impermeable to further excitation by the laser light (see Figure 1.5). Given sufficient time, a large fraction of electrons will eventually be pumped from the m = -1/2 ground state to the m = +1/2 ground state.

The photon emitted during the Rb electron's decay back to its ground state has the same energy as the laser light but is not σ+ circularly polarized. Hence, absorption of these photons emitted during the electrons' relaxation back to the ground state tends to depolarize the Rb. A small amount of N_2 is added to the cell in order to collisionally de-excite the Rb and reduce the number of stray, non-circularly polarized, 794.7 nm photons. A mixture of ^{3}He and 0.5% N_2 at 10 atm reduces the Rb electron relaxation rate by a factor of 10 (4).

The Rb polarization time and the achievable final polarization level depend on the rate at which photons are absorbed by the Rb electrons. Laser power and linewidth are important experimental considerations. One major challenge to SEOP using diode lasers is that the Rb electrons' $5s_{1/2}$-$5p_{1/2}$ absorption line is much narrower than a diode laser

linewidth, resulting in a significant waste of laser light. This problem is remedied by either broadening the Rb absorption line or narrowing the laser line (or both). At 200°C the Rb absorption width is a mere 250 MHz (0.0005 nm), 0.025% the width of the 2 nm linewidth of a typical 794.7 nm diode laser. Pressure broadening, however, increases the Rb absorption line by 18 GHz/atm. Polarizing cells are typically filled with around 10 atm of gas, increasing the Rb absorption line to around 180 GHz (0.38 nm) (60). Further absorption efficiency can be achieved with frequency narrowed laser technology, reducing laser linewidth to as low as 0.2 nm (10, 12).

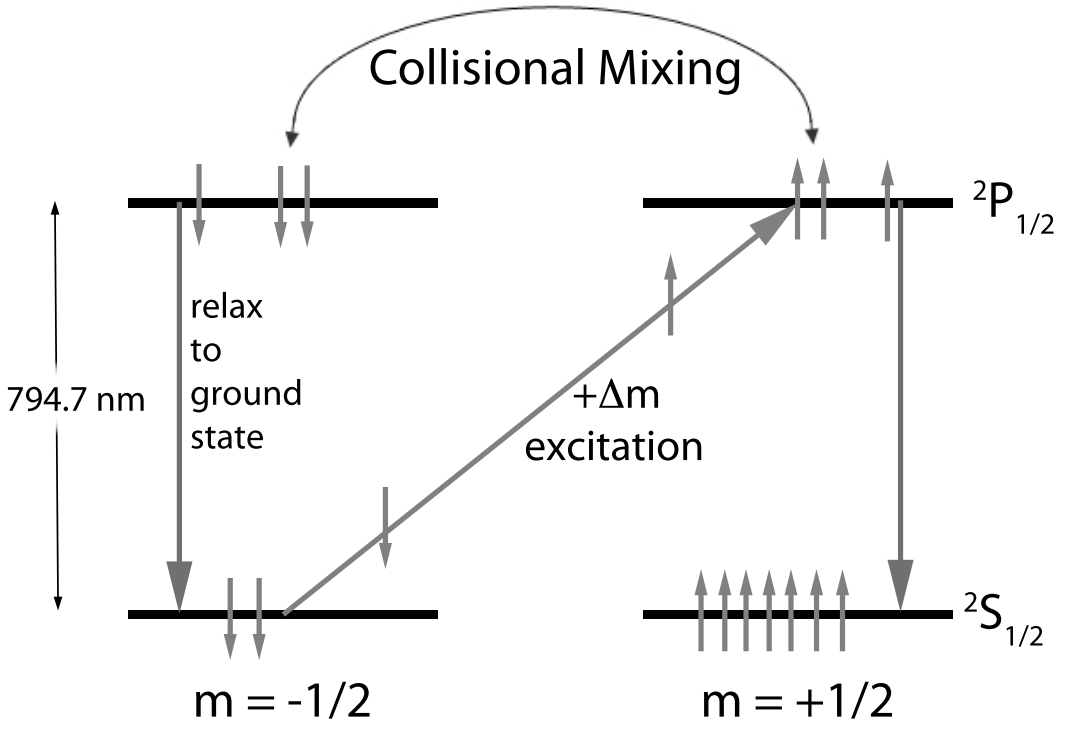

Figure 1.5: Spin optical pumping of Rb electrons from the spin-down state to the spin-up state. σ+ circularly polarized 794.7 nm photons excite electrons in the m = -1/2 ground state to the first m = +1/2 excited state. After collisional mixing, electrons return to either the m = -1/2 or m = +1/2 ground state with equal probability. Over time, depopulation of the m = -1/2 ground state leads to high levels of Rb electron polarization.

Spin angular momentum is transferred from the Rb electron to a spin-1/2 noble gas nucleus by collision through the hyperfine "Fermi-contact" interaction (61). References (4, 30) provide a detailed description and derivation of this spin exchange process. Relaxation of a hyperpolarized gas back to its Boltzmann equilibrium results from collisions with other atoms and the walls of the polarizing cell. This process is characterized by the T_1 relaxation in Eq. 1.7. The T_1 time constant varies widely depending on the choice of nuclei, the purity of the gas, and the cell material and preparation method. Woods (30) shows that, in the long time limit, the noble gas nuclear polarization approaches

$$P = \frac{P_{Rb}\gamma_{se}}{\gamma_{se}+T_1^{-1}} \qquad 1.26$$

where P_{Rb} is the Rb polarization level and γ_{se} is the spin exchange rate between the Rb electrons and the noble gas nuclei. γ_{se} has been measured experimentally to be around $(6h)^{-1}$ for Rb and ^{3}He (30). From this equation it is evident that nuclear polarization increases monotonically with T_1, and for $T_1^{-1} \gg \gamma_{se}$, P and T_1 are proportional.

Of the noble gases, only ^{3}He and ^{129}Xe are both spin-1/2 and stable. Both gases can be successfully hyperpolarized for use in pulmonary MRI, though ^{3}He has several important advantages, which make it ideally suited for diffusion MR lung morphometry. The signal acquired during an NMR experiment is proportional to a nucleus's gyromagnetic ratio (1). The gyromagnetic ratio of ^{3}He is 2.7 times that of ^{129}Xe, resulting in a similar gain in SNR. In addition, ^{3}He has a T_1 of tens of hours in the absence of oxygen making transport across distances of several miles and short-term storage possible. The longer T_1 also results in higher polarization levels, which contributes to higher SNR. Helium also has negligible solubility in tissue, is non-toxic and inert, and has been shown to be safe for human consumption.

^{3}He's biggest disadvantage is its scarcity. With an isotopic natural abundance of only 1.4 ppm, usable quantities of helium exist primarily as a byproduct of the well-funded endeavor of maintaining nuclear weapons. Tritium, a key component of nuclear weapons, decays into ^{3}He, which is then sold at auction in order to recoup some of the cost of tritium purification. After September 2001, a large fraction of the United States' ^{3}He stockpile was consumed in the production of neutron detectors, deployed to detect nuclear material at US borders and around the world. The United States' ^{3}He stockpile is now around 20% of its 2001 size (51). ^{3}He cost has subsequently increased by over 500% (now around $700/L) in just a few years, and, at times, ^{3}He has not been available at all. In order to insure the continued advancement of pulmonary imaging research, nearly all ^{3}He used in current NMR experiments is recaptured and stored for eventual purification, compression, and reuse (66).

1.5 Lung Architecture

The lung is a network of branching airways in which the size of each daughter airway is either smaller than or equal in size to its parent airway. Lung structure is generally described with a simple bifurcating branching model. The trachea branches into left and right main bronchi which in turn branch into a total of four lobar bronchi, which branch into 16 smaller airways, and so on. The bifurcating nature of branching results in 2^k branches at the k^{th} branching generation. As a consequence, the total number of airways at each branching generation is equal to the sum of all airways from all previous generations of branching combined.

The lung consists of around 24 total generations of airways which can be divided into two general regions based on the airway's generational proximity to the trachea. The first

17 generations define the conducting region of the lung, and the last 7 generations comprise the respiratory region. Two functional differences distinguish conducting airways from respiratory airways (64). First, the transport of gas through the conducting region of the lung occurs, as the name implies, by conduction due to pressure differences caused by the lung's changing volume. By contrast, gas transport in the respiratory region occurs almost completely by diffusion, that is, by Brownian motion. For this reason, the respiratory region of the lung is sometimes also referred to as the diffusion region. The second distinction between the two regions is that conducting airways are void of alveoli, and, thus, do not take part in gas exchange. West refers to the 17 generations of conducting airways as an "anatomic dead space" which serve only as a conduit to the respiratory region of the lung (64).

Classification of the respiratory region is further divided into (1) respiratory bronchioles, which are sparsely line with alveoli, and (2) alveolar ducts, which are completely lined with alveoli. Alveoli are the terminus of oxygen's migration down the airway tree and are where oxygen and carbon dioxide exchange between airspace and blood occurs. By virtue of the nature of bifurcation, there are around 15 million alveolar ducts and between 300 and 600 million alveoli covering a total area of between 50 to 100 square meters. Together the respiratory bronchioles and alveolar ducts comprise the lung acinus and account for around 95% of the lung volume at functional residual capacity (64).

The diameter of the airways in the conducting region decrease like $2^{-k/3}$, where k is the generation number (63). However, in the respiratory region, airway diameter changes very little from one generation to the next, and the alveolar ducts found in the last 3 or 4 branching generations have near uniform size and geometry independent of their generational

location. For the purposes of this study, the geometry of alveolar ducts is treated within the framework proposed by Weibel and colleagues (25, 67, 68). The duct is modeled as a long hollow cylinder of radius R lined with annuli of inner radius r and outer radius R, periodically spaced along the inside of the cylinder and separated by a distance L. The space between the annuli is further segmented by 8 alveolar walls extending between annuli and from the outer wall of the cylinder radially inward to a depth $h = R - r$ (see Figure 1.6).

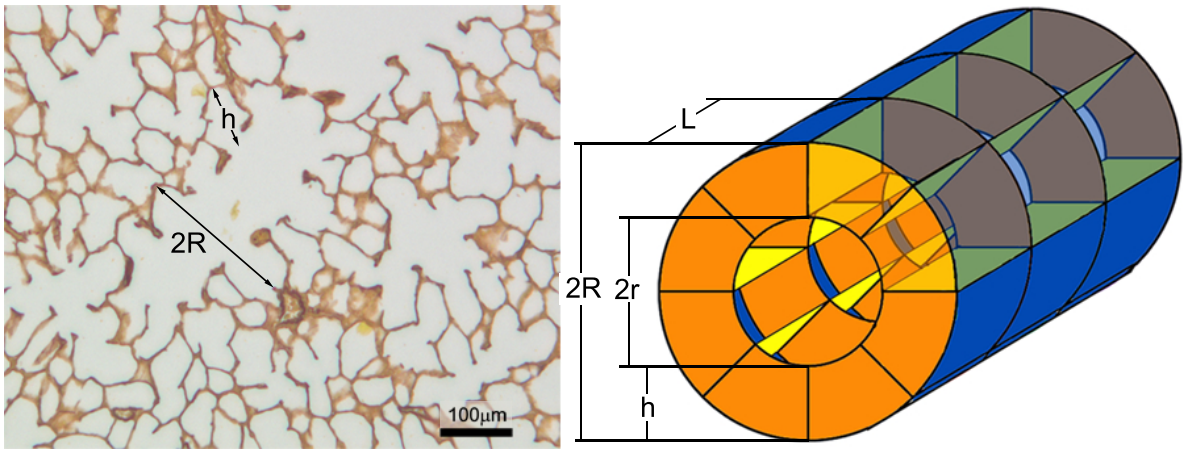

Figure 1.6: Left: Microscope image showing morphometric parameters h and R for an alveolar duct oriented parallel to the slide. Right: Model of an oblique alveolar duct assumed in MR morphometric analysis. Three segments of the periodic structure are shown. The outer walls of two alveoli from each segment have been made transparent for clarity.

A single alveolar duct unit is defined as the space between two adjacent annuli and contains 8 alveoli (see ref. (68) for discussion regarding the number of alveoli per duct unit); the surface area of a single alveolus is

$$S_a = \frac{1}{4}\pi RL + \frac{1}{4}\pi(R^2 - r^2) + 2hL \qquad 1.27,$$

the volume of a single alveolus is

$$V_a = \frac{1}{8}\pi R^2 L \qquad 1.28,$$

and the alveolar number density is

$$n_a = 1/V_a \quad (1.29)$$

Note that the alveolar volume, as defined in Eq. 1.28, is one eighth of the volume of the alveolar duct unit. That is, the alveolar volume includes both the alveolar proper volume (defined in Eq. 1.30) and an eighth of the lumen volume (Eq. 1.31).

$$V_{a,proper} = \frac{1}{8}\pi(R^2 - r^2)L \quad (1.30)$$

$$V_{a,lumen} = \frac{1}{8}\pi r^2 L \quad (1.31)$$

In order to minimize the number of geometric parameters needed to describe the size and shape of an alveolar duct, the alveolar length, L, is related to the alveolar duct radius, R, by:

$$L = 2R\ sin(\pi/8) \quad (1.32)$$

This relationship ensures that the alveolar dimensions are the same in the direction along the airways axis and along the outer circumference. This assumption agrees well with experimental observations (40, 42, 50, 63).

In the next chapter, the geometric model for alveolar ducts described here is used to develop a set of mathematical relationships between the MR diffusion measurements described in section 1.3 and the morphometric parameters R and h. This technique of measuring precise lung geometric parameters via ^{3}He diffusion MR measurements is referred to as ^{3}He lung morphometry. With the parameters R and h, the volume and surface area of individual alveoli are calculated using Eqs. 1.28, 1.27, and 1.32. Additionally, measurements of the total lung volume (from either MR images or spirometry) allow for the calculation of the total number of alveoli

$$N_{tot} = \overline{n}_a V_{tot} \quad (1.33)$$

and the total lung surface area

$$S_{tot} = N_{tot} S_a \qquad 1.34.$$

In this study, these morphometric parameters are measured at different levels of lung inflation and deflation in order to better understand the mechanisms of lung volume change at the alveolar level.

Chapter 2: ^{3}He Lung Morphometry

2.1 Anisotropic Diffusion in the Lung Acinus

While *ADC* measurements using Eq. 1.24 provide a powerful technique for performing lung microscopy, Figure 2.1 shows that real lung diffusion data diverge from the best-fit monoexponential curve of Eq. 1.24. The non-monoexponential nature of signal attenuation results from the anisotropic diffusion of the gas within the restricted medium of the lung. A more sophisticated model of gas diffusion within the lung, which takes into account the anisotropy of diffusion in a network of acinar airways, was proposed by Yablonskiy *et. al.* (67). Using the well established cylindrical model of acinar airways proposed by Weibel (25), Yablonskiy proposed that diffusion within an acinar airway can be characterized with a linear combination of diffusion coefficients in an airway's transverse and longitudinal directions. Recall that in an MR diffusion experiment diffusion is *only* measured in the direction of the diffusion gradient. Consequently, the measured diffusion coefficient (by Eq. 1.24) for a cylindrical airway oriented parallel to the diffusion gradient can be characterized by a longitudinal diffusion coefficient, D_L, and the diffusion coefficient for a cylindrical airway perpendicular to the diffusion gradient can be characterized by a transverse diffusion coefficient, D_T. In terms of its anisotropic components, the diffusion coefficient for an alveolar duct at an angle α to the diffusion gradient (see Figure 2.2) is, in general,

$$D(\alpha) = D_L \cos^2\alpha + D_T \sin^2\alpha \qquad 2.1.$$

Combining Eq. 1.24 and 2.1, the signal attenuated gradient echo amplitude within a single alveolar duct at an angle α to the diffusion gradient is

$$S_{airway} = S_0 \exp[-b(D_L \cos^2\alpha + D_T \sin^2\alpha)] \qquad 2.2.$$

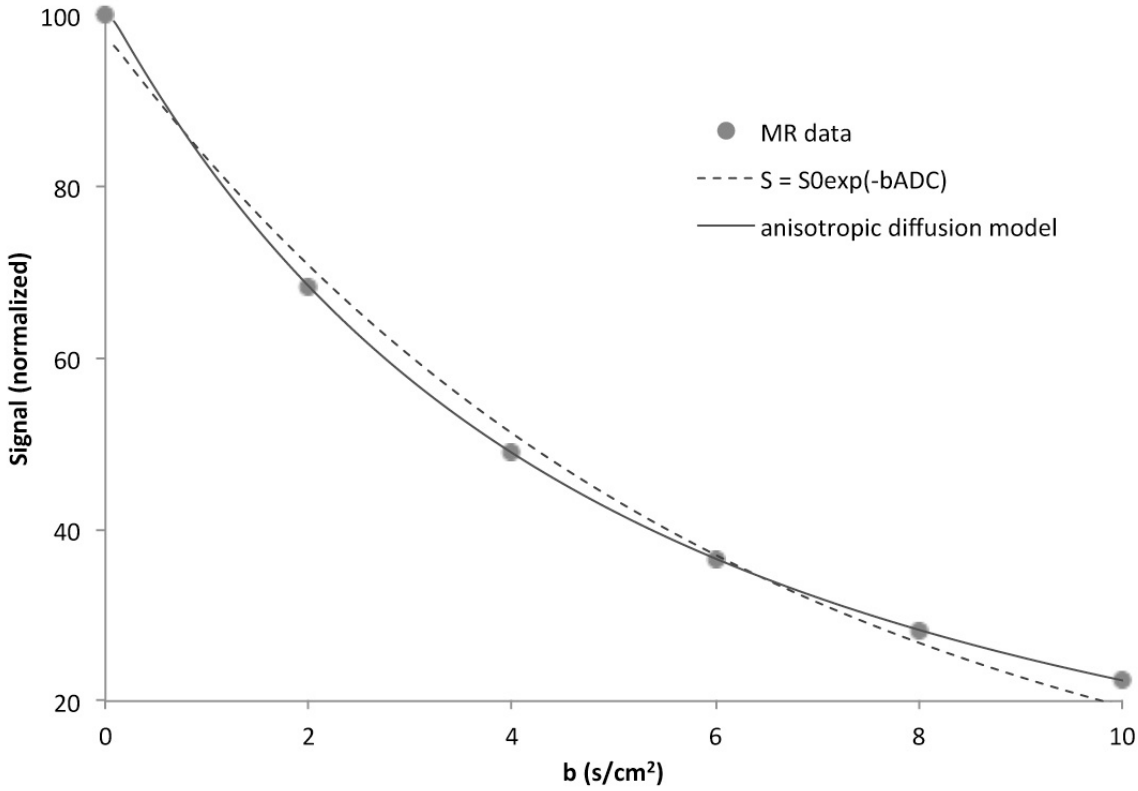

Figure 2.1: Plot of signal from an MR diffusion experiment as a function of the diffusion gradient parameter, *b*, and corresponding fits of Eq. 1.24 (dashed line) and Eq. 2.3 (solid line).

A typical imaging voxel contains hundreds of randomly oriented acinar airways. The angle, α, between the diffusion gradient and an airway's longitudinal direction is a random variable with a uniform distribution between 0 and π. The net signal from the collection of randomly oriented airways within a single voxel is thus

$$S_{voxel} = \int_0^{\pi} S_{airway} \frac{\sin\alpha}{2} d\alpha = S_0 e^{-bD_T} \left(\frac{\pi}{4b(D_L - D_T)}\right)^{1/2} \Phi[(b(D_L - D_T))^{1/2}] \qquad 2.3,$$

where Φ[x] is the error function and S_0 is the echo amplitude in the absence of a diffusion gradient (b = 0).

Because MR signal attenuation is non-monoexponential, the value of *ADC* measured using Eq. 1.24 will depend on the diffusion gradient b-values used to acquire the MR signal (18). Uniformly integrating Eq. 2.1 over all orientation angles allows *ADC* to be written in terms of the anisotropic diffusion coefficients:

$$ADC = \frac{1}{3} D_L + \frac{2}{3} D_T \qquad 2.4.$$

The expression for *ADC* given in Eq. 2.4 has a much weaker dependence on b-value, and thus provides a more objective measurement of the restricted diffusivity than Eq. 1.24.

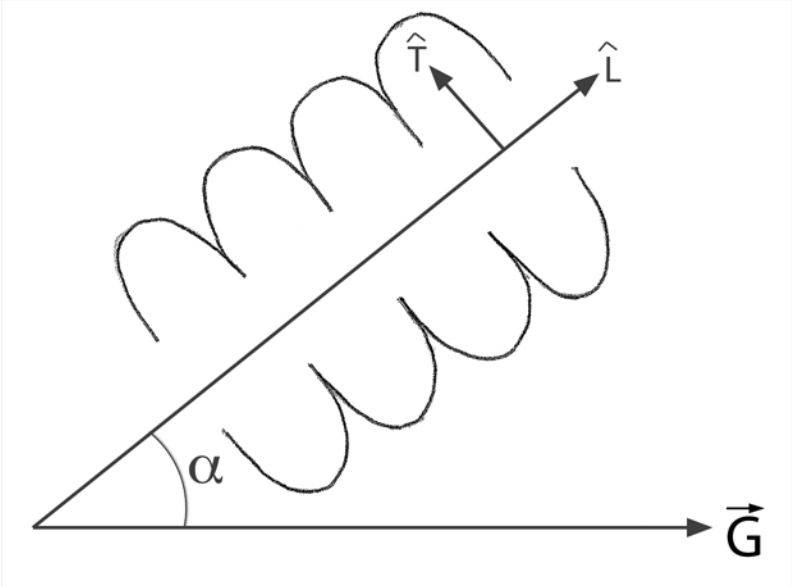

Figure 2.2: Diagram showing an alveolar duct an angle α relative to the diffusion gradient vector **G**. The duct's longitudinal ($\hat{L}$) and transverse ($\hat{T}$) directions are also shown.

2.2 Human Morphometric Model

The mathematical relationship given in Eq. 2.3 between diffusion NMR signal attenuation and the anisotropic cylindrical diffusion coefficients is the first step in relating NMR diffusion measurements to alveolar geometry. The next step, formulation of a precise

mathematical relationship between the anisotropic diffusion coefficients, D_L and D_T, and alveolar geometric parameters was accomplished by Sukstanskii and Yablonskiy by means of Monte Carlo simulations (57, 68) of diffusion within the geometric structure of Figure 1.6.

In these simulations, virtual particles with diffusion properties of ^{3}He dilute in air (D_0 = 0.88 cm^2/s) underwent a random walk within the three-dimensional geometric structure of Figure 1.6. The particle's position was updated after discrete simulated time steps of 1 μs. After each time step the particle advanced a distance equal to the rms displacement of a freely diffusing ^{3}He atom in one of eight randomly chosen directions, (±1, ±1, ±1). If the particle's new position after a time step crossed a boundary of the alveolar duct, the move was discarded and the particle remained stationary.

In order to simulate the effect of diffusion on NMR signal attenuation, a virtual time-dependent magnetic field gradient was applied at an angle α across the duct, and the phase of each particle, initially set to zero, was updated at each time step to reflect the gradient's effect as dictated by Eq. 1.16. The gradient magnitude at each time point corresponded to that of the trapezoidal bipolar gradient pulse described in Section 1.3 and shown in Figure 1.3. The timing parameters of the gradient pulse corresponded to those used in a typical diffusion MRI experiment (τ = 0.3 ms, δ = 1.6 ms, and Δ = 1.6 ms). Each particle advanced over the 3200 time steps corresponding to a total time equal to the gradient pulse duration (3.2 ms). After simulations of N particles, the normalized MR signal, attenuated by the spread in phases, was calculated as

$$S = \frac{1}{N}\sum_{j=0}^{N} \cos \Delta\phi_j \qquad 2.5$$

where $\Delta\phi_j$ is the net phase change of the jth particle after application of the bipolar diffusion gradient. The simulations were repeated up to 20 times for additional sets of N particles with

b-values between 0 and 10 s/cm^2. The b-value dependent anisotropic diffusion coefficients, D_L and D_T, were determined by

$$D(\alpha, b) = -\frac{1}{b}\ln S(\alpha, b) \quad 2.6$$

where the angle, α, between the airway's axis and the gradient direction was set to either 0 to measure longitudinal diffusivity or to π/2 to measure transverse diffusivity.

The procedure outlined above was repeated for a range of values for the alveolar duct radius, R, and the alveolar depth, h. The alveolar length, L, was kept proportional to R as specified in Eq. 1.32. D_L and D_T were calculated for each unique combination of b, R, and h using N equal to 10^6 to 10^7 particles. Based on simulations with R ranging from 280 μm to 400 μm and h ranging from 0 to R, Yablonskiy and Sukstanskii found the following set of empirical equations relating the anisotropic diffusion coefficients, D_L and D_T, to the geometric parameters R and h:

$$D_L = D_{L0}(1 - \beta_L \cdot bD_{L0}) \quad 2.7$$

$$D_T = D_{T0}(1 + \beta_T \cdot bD_{T0}) \quad 2.8$$

$$\beta_L = 35.6 \cdot \left(\frac{R}{l_1}\right)^{1.5} \cdot \exp\left[\frac{-4}{\sqrt{h/R}}\right] \quad 2.9$$

$$\frac{D_{L0}}{D_0} = \exp\left[-2.89 \cdot \left(\frac{h}{R}\right)^{1.78}\right] \quad 2.10$$

$$\frac{D_{T0}}{D_0} = \exp\left[-0.73 \cdot \left(\frac{R}{l_2}\right)^{-1.4} \cdot \left(1 + \exp\left(-A \cdot \left(\frac{h}{R}\right)^2\right) \cdot \left\{\exp\left[-5\left(\frac{h}{R}\right)^2\right] + 5 \cdot \left(\frac{h}{R}\right)^2 - 1\right\}\right)\right. \quad 2.11$$

$$A = 1.3 + 0.25 \cdot \exp\left[14 \cdot \left(\frac{R}{l_2}\right)^2\right] \quad 2.12$$

where $\beta_T = 0.06$. $l_1 = (2D_0\Delta)^{1/2}$ and $l_2 = (4D_0\Delta)^{1/2}$ are free-diffusion lengths in one- and two-dimensions, respectively. Due to the non-Gaussian effects of anisotropic diffusion, D_L and D_T have a linear dependence on the diffusion gradient parameter b. D_{L0} and D_{T0} are the

anisotropic diffusion coefficients for b = 0. To emphasize the scalability of these results, Eqs. 2.7 – 2.12 are written in terms of dimensionless parameters R/l_1, h/R, and R/l_2. In order to show a few general features of these relationships, D_{L0}/D_0 (Eq. 2.10) and D_{T0}/D_0 (Eq. 2.11) are plotted in Figure 2.3 as a function of the variables h/R and R/l_2, respectively. In Figure 2.3b h/R is set to 0.5. We note that, within the physically relevant range of h/R = 0.1 to 0.9, D_{T0}/D_0 has a very weak dependence on h/R and any insight gleamed from the plot in Figure 2.3b is applicable to all other values of h/R.

Figure 2.3 shows that the relationships between the anisotropic diffusion coefficients, D_{L0} and D_{T0}, and the parameters R and h agree with reasonable intuition for large and small values of R and h. As h/R approaches zero, the impediments to diffusion in the longitudinal direction are removed and D_{L0} approaches the free diffusivity, D_0. As h/R approaches 1, diffusion in the longitudinal direction becomes highly restricted and D_{L0}/D_0 approaches a small, non-zero value. Likewise, as R becomes much bigger than l_2, D_{T0} approaches D_0, and as R approaches zero, D_{T0} approaches zero as well.

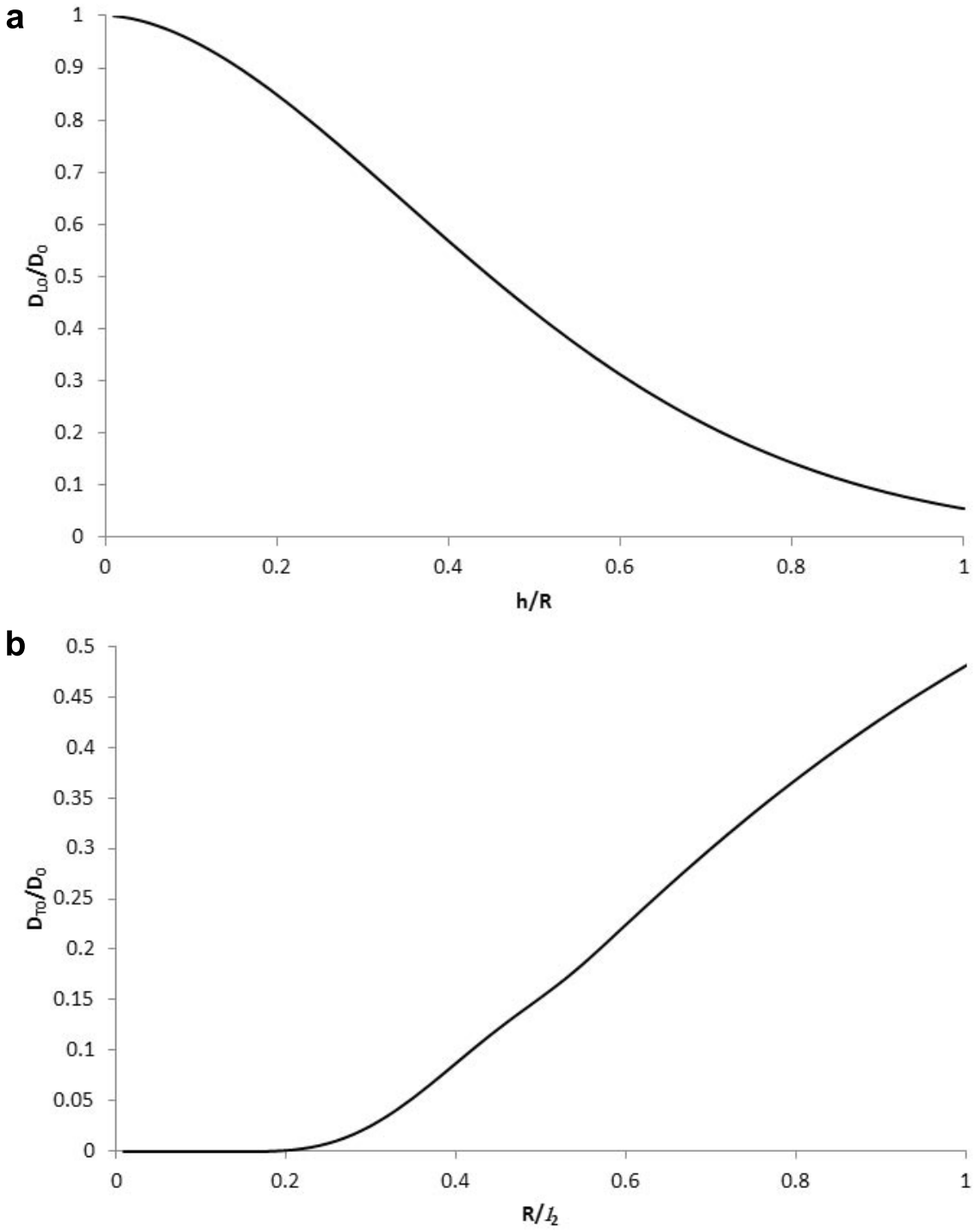

Figure 2.3: (a) Plot of D_{L0}/D_0 as function of h/R as given in Eq. 2.10. (b) Plot of D_{T0}/D_0 as a function of R/l_2 as given in Eq. 2.11.

Figure 2.3b also illustrates the importance of choosing an appropriate diffusion length, l_2, providing insight for an optimal choice of the bipolar diffusion gradient parameter, Δ (recall that l_2 is proportional to the square root of Δ). Ideally, values of R measured by ^{3}He lung morphometry should fall within the range for which Eq. 2.11 is most sensitive to differences in R. Put another way, Eqs. 2.10 and 2.11 are most effective over a range for which the magnitudes of their slopes are relatively large. The corresponding slopes from Figure 2.3 are plotted in Figure 2.4. Haefeli-Bleuer and Weibel report average values of alveolar duct radii of around 350 μm (25) in healthy humans. This, together with Figure 2.4b, suggests that an optimal value of l_2 is between 600 μm and 900 μm. For ^{3}He dilute in air, D_0 is 0.88 cm^2/s which requires a diffusion time of between 1.0 ms and 2.3 ms. Hardware restrictions for the MRI scanner used in this study place a lower limit of 1.8 ms on Δ, making it a suitable choice for the pulse sequence diffusion time.

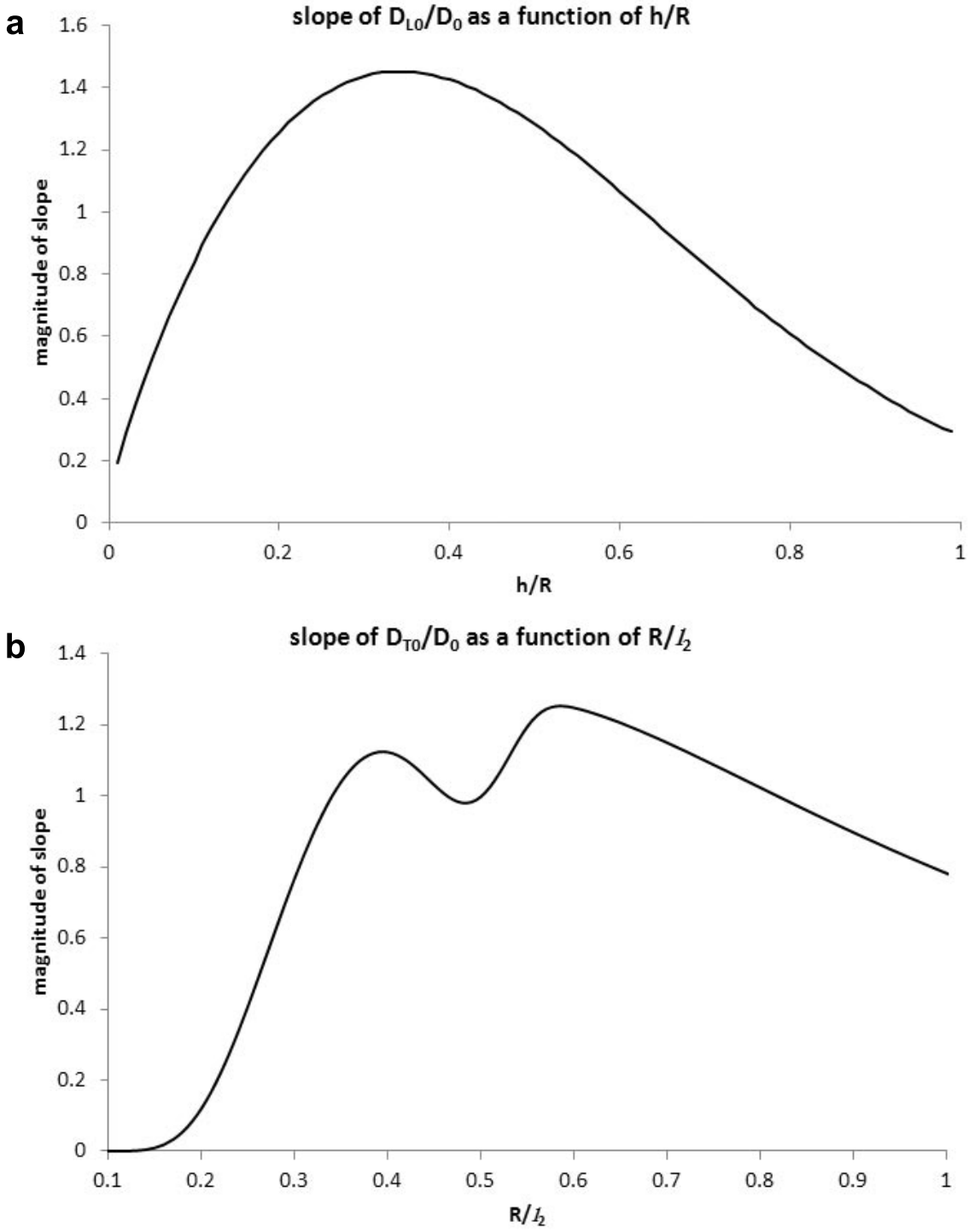

Figure 2.4: (a) Plot of the first derivative of Eq. 2.10 with respect to *h/R*. (b) Plot of the first derivative of Eq. 2.11 with respect to R/l_2.

2.3 Canine Model

For a diffusion time of 1.8 ms, l_2 = 796 μm. Based on a rough estimate from Figure 2.4b, Eqs. 2.7 – 2.12 will be most effective for R/l_2 greater than about 0.3, or for R greater than about 240 μm. Figure 2.4b also indicates that these equations will be less accurate when used to measure values of R between about 160 μm and 240 μm (or R/l_2 between 0.2 and 0.3), and nearly useless for R less than 160 μm (or R/l_2 less than 0.2). These predictions have been verified by fits to simulated data using Bayesian Inference and by inspection of the corresponding posterior probability distribution. Recall also that Eqs. 2.7 – 2.12 were obtained via simulations with values of R between 280 μm and 400 μm. As with any modeling based on a fixed range of inputs, these equations are not necessarily valid outside of this range.

Eqs. 2.7 – 2.12, with the above choice of Δ, were intended for performing ^{3}He lung morphometry experiments in human subjects, and, for that purpose, they are well suited. Over 98% of voxels in ^{3}He MR diffusion images of human lungs contain airways with average R-values between 240 μm and 400 μm, and virtually no airways are smaller than 160 μm. However, one aim of this study is to use ^{3}He lung morphometry to study canine lungs, which are composed of airways typically smaller than those found in human lungs. The average canine acinar airway radius is around 225 μm (26). Around 65% of canine airways have radii smaller than 240 μm and around 7% of airways have radii smaller than 160 μm. The ideal solution to this problem would be to employ a bipolar diffusion gradient with a shorter diffusion time, Δ, in order to reduce l_2 and, thus, the range over which Eqs. 2.7 – 2.12 are valid. However, due to the aforementioned hardware restrictions, such a solution is not

feasible. Instead, a new set of equations similar to Eqs. 2.7 - 2.12 but specific to canine airway sizes have been developed.

Monte Carlo simulations identical to those described in section 2.2 were performed for diffusion gradients oriented parallel and perpendicular to the longitudinal axis of an alveolar duct for 20 *b* values ranging from 0 to 10 cm^2/s, 5 values of *R* from 140 μm to 260 μm, and values of *h* from 0 to *R* (1000 total combinations of *b, R,* and *h*). As before, the alveolar length, *L,* was specified by Eq. 1.32. These simulations resulted in the following set of empirical relationships between the anisotropic diffusion coefficients, D_L and D_T, and the alveolar duct geometric parameters *R* and *h*:

$$D_L = D_{L0}(1 - \beta_L b D_{L0}) \quad 2.13$$

$$\beta_L = 96.4\left(\frac{R}{l_1}\right)^{1.5} \exp\left[\frac{-4.86}{\sqrt{h/R}}\right] \quad 2.14$$

$$\frac{D_{L0}}{D_0} = \exp\left[-2.87\left(\frac{h}{R}\right)^{1.75}\right] \quad 2.15$$

$$\frac{D_{T0}}{D_0} = \frac{7}{16}\left(\frac{R}{l_2}\right)^{(4-3.61(R/l_2)^{0.63}} \left(1 + \exp\left(-A\left(\frac{h}{R}\right)^2\right)\left\{\exp\left[-5\left(\frac{h}{R}\right)^2\right] + 5\left(\frac{h}{R}\right)^2 - 1\right\}\right) \quad 2.16$$

$$A = -6.55 + 6.44\exp\left[2.68\left(\frac{R}{l_2}\right)^2\right] \quad 2.17.$$

Throughout the remainder of this dissertation, Eqs. 2.7 - 2.12 will collectively be referred to as the "human model" and Eqs. 2.13 - 2.17 will collectively be referred to as the "canine model". D_{L0}/D_0 is plotted in Figure 2.5a as a function of *h/R* for both the human and canine models. D_{T0}/D_0 is plotted in Figure 2.5b as a function of *R* for both models with *h/R* = 0.5 and l_2 = 796 μm. While the dependence of D_{L0} on *h/R* is nearly identical for the human and canine models, the plots of D_{T0} for the two models (Eq. 2.11 and Eq. 2.16) diverge for *R* less than around 300 μm. Because the canine model is based on simulations for *R* < 300 μm

(between 130 μm and 260 μm), it is the optimal model for performing ^{3}He lung morphometry in lungs composed of alveolar ducts with radii in that range. While both models become less effective at resolving differences in R as R becomes small, Figure 2.5b illustrates that the canine model is markedly better at resolving these differences for values of R less than 160 μm.

To test the accuracy of each of these mathematical models, the values of D_{L0}, β_L, and D_{T0} calculated from Eqs. 2.9, 2.10, and 2.11 (the human model) and Eqs. 2.14, 2.15, and 2.16 (the canine model) for various combinations of R and h were compared to the values of those parameters generated by Monte Carlo simulations. The percent differences in the values obtained by simulations and those predicted by the respective models for $h/R = 0.5$ are plotted in Figure 2.6 for different values of R. This plot shows that the human model accurately predicts anisotropic diffusion coefficients for values of R between 280 μm and 400 μm, but the model becomes unreliable for values of R less than 280 μm. The canine model, on the other hand, produces accurate values for D_{L0} and D_{T0} for airway radii between 140 μm and 400 μm and produces accurate values for β_L for airway radii up to about 300 μm.

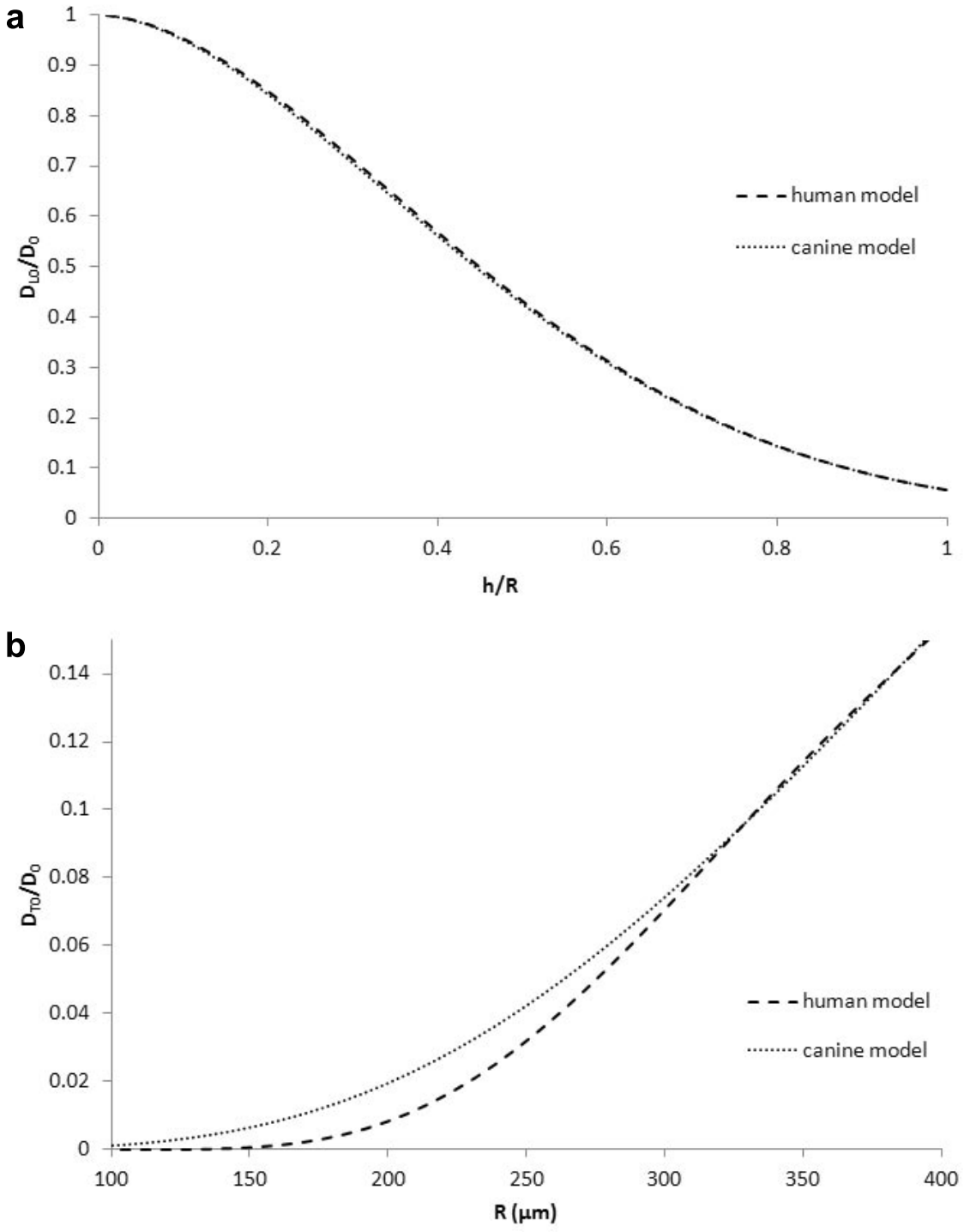

Figure 2.5: (a) Plot of D_{L0}/D_0 from the human (Eq. 2.10) and canine (Eq. 2.15) models as a function of h/R. (b) Plot of D_{T0}/D_0 from the human (Eq. 2.11) and canine (Eq. 2.16) models as a function of R.

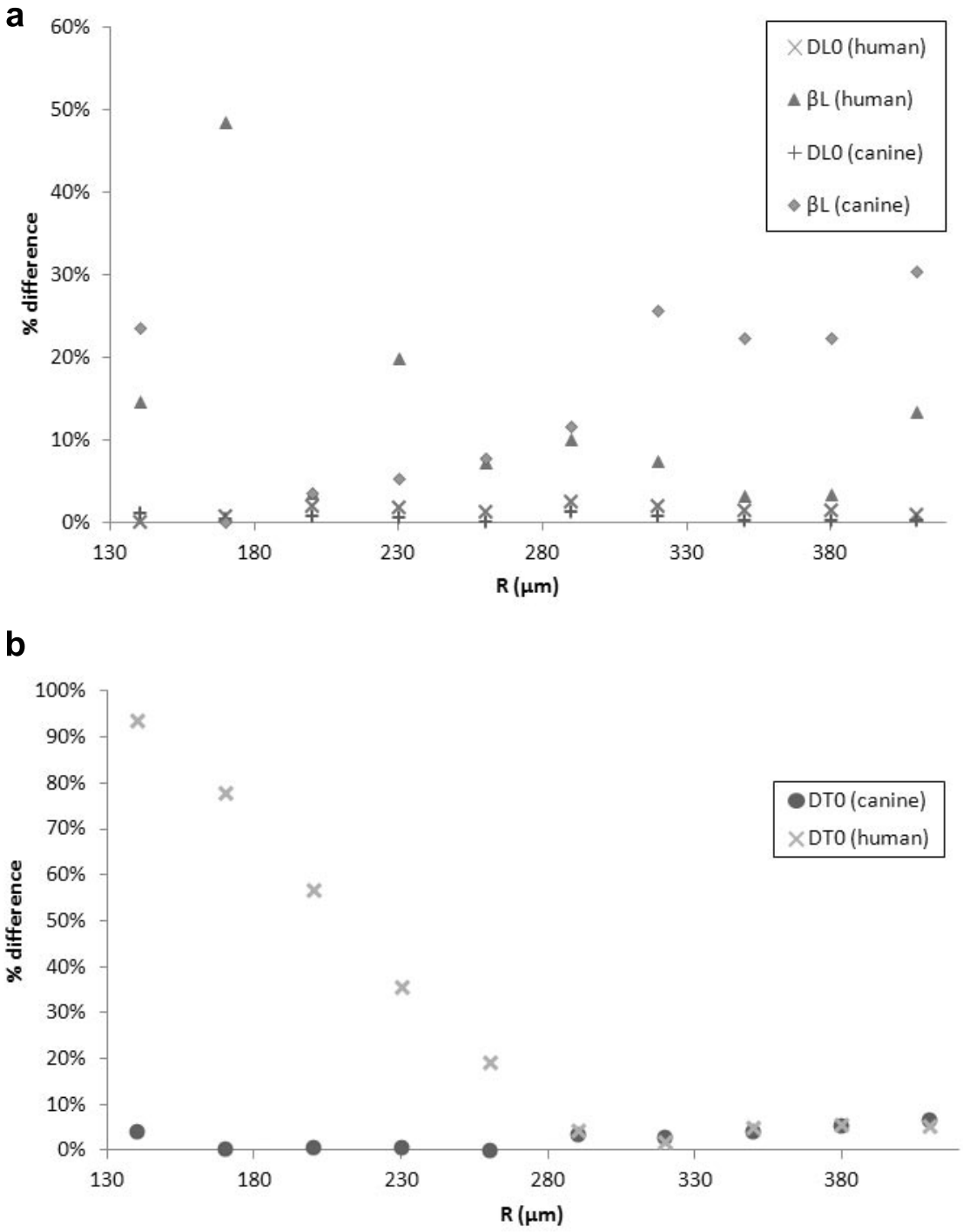

Figure 2.6: (a) Plot of the percent difference between values of D_{L0} and β_L generated by Monte Carlo simulations and values obtained from Eqs. 2.9 and 2.10 (human model) and Eqs. 2.14 and 2.15 (canine model) for values of R ranging from 130 μm to 410 μm with h/R = 0.5. (b) Plot of the percent difference between computer generated values of D_{T0} and values obtained from Eq. 2.11 (human model) and Eq. 2.16 (canine model) for values of R ranging from 130 μm to 410 μm with h/R = 0.5.

2.4 MR Images, Data Filtering, and Model Fitting

Typical diffusion MR images are composed of thousands of voxels. Each image covers a slice of the lung, and the entire lung is covered by 3 to 10 slices. Multiple images are obtained for each slice, each with a different diffusion gradient magnitude (different b-values). The diffusion attenuated MR signal from each voxel is fit by Eq. 2.3 and the appropriate morphometric model (Eqs. 2.7 - 2.12 for human lungs and Eqs. 2.13 – 2.17 for canine lungs) in order to obtain an average value for R and h for the alveolar ducts in that voxel.

It has been demonstrated that SNR on the order of around 100 is adequate to accurately evaluate R and h (56). Thus, any voxels with SNR below 100 were excluded from the morphometric analysis. Since only ^{3}He produces MR signal, and all ^{3}He is contained within the lung, this requirement filters out all voxels outside of the lung.

The ^{3}He morphometric models were obtained using simulation of diffusion within alveolar ducts and may not be applicable to non-acinar airways. Furthermore, the choice of diffusion time (Δ = 1.8 ms) restricts use of the model to airway radii smaller than around 400 μm. Fortunately, around 95% of gas resides in acinar airways, which meet this size criterion. Typical ADC values are around 0.22 cm^2/s within the lung acinus and 0.88 cm^2/s in the trachea. For each voxel, ADC is measured using Eq. 1.24. Voxels with ADC larger than 0.5 cm^2/s are assumed to contain large airways and are excluded from the morphometric analysis.

The ^{3}He morphometric models are fit to the MR diffusion data using the Levenberg-Marquardt algorithm for least squares curve fitting (31, 37). A fit with an excessively large

95% confidence interval is considered poor and all morphometric parameters from voxels with poor fits are excluded from all parameter maps and any reported averages.

Chapter 3: Lung Micromechanics

The mechanism for lung volume change has been a subject of contention among researchers for over six decades. Over the full inflationary range, the human lung expands to over twice its residual volume. Since acinar airways make up over 95% of the lung, it follows that this macroscopic volume change is the result of a collective change in these airways. However, the open question remains, what is the nature of this microstructural change?

In 1950, Charles Macklin, a pioneer in pulmonary research, described the alveolar duct as a cylindrical hallway with "contiguous alveoli opening into it all the way around" (36). This understanding of alveolar geometry is still widely held and a simple but precise geometric representation is described in section 1.5 and shown in Figure 1.6.

In their chapter on micromechanics of the lung in the *Handbook of Physiology*, Greaves, Hildebrandt, and Hoppin discuss five possible mechanisms of lung expansion (24). They propose that during inflation the cylindrical alveolar ducts described my Macklin might undergo: (1) isotropic changes in alveolar dimensions (that is, uniform scaling of all dimensions), (2) an increase in alveolar depth (a "saucer-to-cup" like change in the shape of alveoli), (3) a decrease in alveolar depth (a "cup-to-saucer" like change in the shape of alveoli), (4) no change in alveolar surface area (a special case of (3) which the authors refer to as "accordion-like extension"), or (5) instantaneous opening of new alveoli from a completely collapsed state via a process known as alveolar recruitment. Illustrative sketches of each of these mechanisms are shown in Figure 3.1.

A simple mathematical model for analyzing alveolar mechanics relates the total alveolar surface area, S_{tot}, to total lung volume, V_{tot}, by the power function

$$S_{tot} = kV_{tot}{}^{n} \qquad 3.1$$

where k and n are constants (24). Greaves *et al.* outline the relationship between possible values of n and each of the five previously mentioned mechanisms for lung inflation. Isotropic changes in alveolar dimensions would result in $n = 2/3$, "saucer-to-cup" like change in alveolar shape would result in $n > 2/3$, "cup-to-saucer" like change in the shape would result in $n < 2/3$, "accordion-like extension" would result in $n = 0$, and alveolar recruitment would result in $n = 1$. The authors point out that Eq. 3.1 is commonly used to interpret the results of studies in lung micromechanics.

The two most common methods for investigating lung micromechanics are histological assessment of frozen or fixed lung tissue (5, 15, 20, 29, 36, 55, 59) and *in vivo* subpleural microscopy (9, 16, 19, 39). With both methods, lung volume and surface area are commonly estimated based on morphometric measurements at different levels of lung inflation and the mechanism of alveolar mechanics is inferred from Eq. 3.1.

The result that $n = 2/3$ in the case of isotropic expansion is not specific to any particular choice of alveolar geometry. Isotropic expansion simply implies that the structure's geometric parameters change in proportion to each other. As a consequence, the structure's volume and surface area can be expressed as $V = c_1x^3$ and $S = c_2x^2$, where x is an arbitrary length parameter. Solving for V in terms of S, results in Eq. 3.1 with $k = c_1/c_2$ and $n = 2/3$. One of the early studies to utilize Eq. 3.1 was conducted by Dunnill in 1967 (15) who fixed dog lungs at various levels of inflation and measured surface area and volume from histological sections using linear intercept measurements. Dunnil measured n to be 0.77,

from which he concluded that isotropic changes in alveolar shape are responsible for changes in lung volume. Using subpleural microscopy, D'Angelo (16) calculated $n = 0.66$ and, similarly, concluded that alveolar ducts expand isotropically. Additionally, Flicker and Lee (19) and Storey and Staub (55) made similar measurements and also calculated values of n around 2/3.

Reports of increased alveolar depth with lung inflation (case 2) have not, to the author's knowledge, been published. If observed indirectly by means of Eq. 3.1, the mechanism would likely be attributed to either alveolar recruitment or isotropic expansion (as was the case with Dunnil's study). Decreased alveolar depth with lung inflation (case 3) have been observed by Macklin (36) and can be inferred by application of Eq. 3.1 to the histological measurement made by Klingele and Staub (29) resulting in $n = 0.44$ (16).

Alveolar recruitment is a lung expansion mechanism, in ways, unlike the others. All other mechanisms describe how alveoli change their shape by means of some continuous process. Recruitment, on the other hand, is a discrete process in which alveoli open nearly instantaneously. In such a case, if the lung doubles in volume, it is because the number of alveoli has doubled. In this case, the surface area, which is just the sum of the surface areas of the individual alveoli, also doubles. Thus the ratio of lung volume to surface area is a constant and the two quantities can be related by Eq. 3.1 with $n = 1$. Smaldone (53), Lum (33), and Carney (9) all observed that alveolar size changes very little during macroscopic changes in lung volume and conclude that the number of alveoli change in proportion with the total lung volume. Carney did so with subpleural microscopy, Lum with histological assessment, and Smaldone with a unique technique involving monodispersed aerosol.

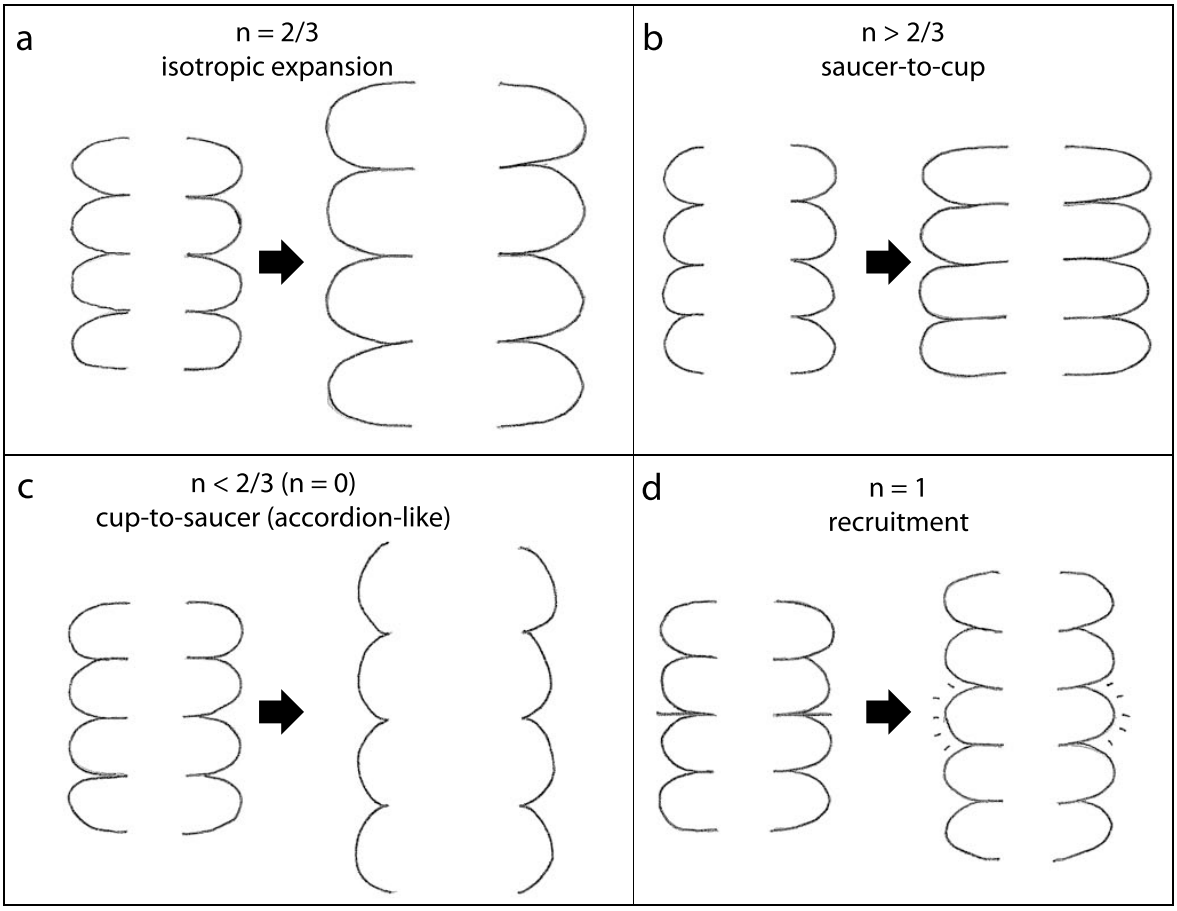

Figure 3.1: Four possible mechanisms for lung inflation at the level of the alveolar duct. (a) isotropic expansion of alveolar ducts. (b) Lengthening of alveolar depth as alveoli change from a saucer shape to a cup shape. (c) Shortening of alveolar depth as alveoli change from a cup to saucer shape. In the case where the alveolar duct surface area remains constant (n = 0), this mechanism is referred to as accordion-like extension. (d) Alveolar size and shape remain constant but increase in number through a process referred to as alveolar recruitment.

While each of the five possible mechanisms for alveolar duct expansion results in a particular value of *n*, the converse is not true. A measured value of *n* could result from any of the five mechanisms alone, or from a combination of recruitment and any of the other four mechanisms. For instance, suppose that individual alveolar ducts increased in volume by an accordion-like extension. This by itself would result in a value of *n* close to zero. But suppose also that there is, at the same time, recruitment of new alveoli. Recruitment, by itself, results in $n = 1$, but the combination of recruitment *and* accordion-like extension

would result in some intermediate value of n. If recruitment contributes more to the macroscopic increases in lung volume, n would be closer to 1, and if accordion-like expansion contributes more, n would be closer to zero. Thus inferences about changes in alveolar ducts from Eq. 3.1 are only valid in a scenario where lung micromechanics can be attributed to a single mechanism. In chapter 6 it is shown that such a scenario is likely not the case in human lung inflation and deflation.

Furthermore, Macklem (35) points out that the model requires measurement precision not attainable by most morphometric techniques, noting that data from studies by both Forrest (20) and Dunnill (15) could be fit by Eq. 3.1 equally well with either $n = 2/3$ or $n = 1$.

Chapter 4: Experimental Equipment

4.1 Polarizers

All ^{3}He used in this study was polarized in one of two polarizer systems. A system located in the Washington University Physic Department's Compton Laboratory, approximately 3 miles from the MR scanners located on Washington University's Medical School campus, was designed and constructed by former students of Mark Conradi's research group (30). The system consists of four main components: (1) a glass cell which holds both Rb and ^{3}He, (2) a ^{3}He filling station, (3) an oven, and (4) a water-cooled diode laser array. The glass cell, which at room temperature contains solid rubidium, is filled with 10 atm of a 99% ^{3}He 1% N_2 mixture at the filling station. The cell is then moved to an oven located between a pair of Helmholtz coils and heated to 165 °C in order to produce the required Rb vapor pressure. While in the oven, 50 to 100 W of 794.7 nm light illuminates the cell, polarizing the Rb electrons via optical pumping, which then polarize the ^{3}He nuclei by spin exchange collisions. A diagram of the cell, oven, laser, and monitoring equipment is shown in Figure 4.1.

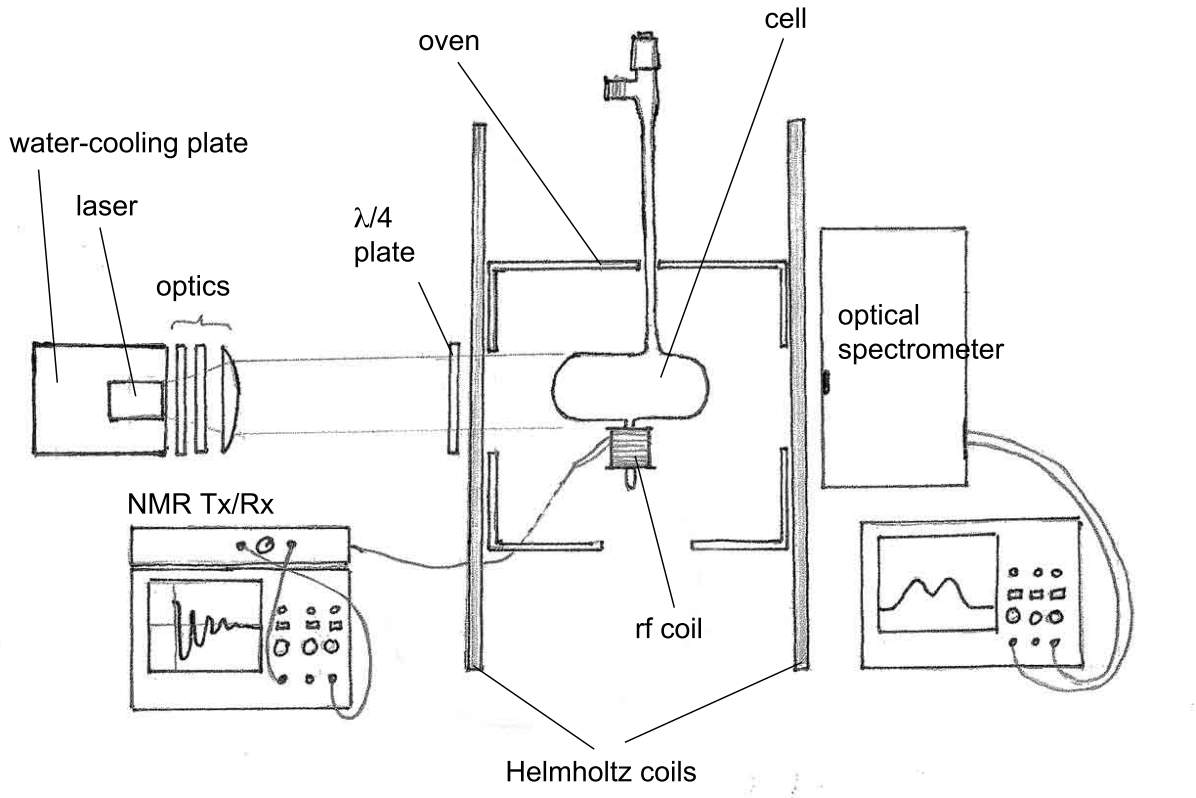

Figure 4.1: ^{3}He Polarizer components. Light from the water-cooled diode laser is collimated by a set of cylindrical lenses, passes through a circularly polarizing quarter-wave plate, and illuminates the glass cell containing ^{3}He and Rb. The cell sits in an oven heated to 165 °C and is located between a pair of Helmholtz coils. Polarization is measured by an rf coil on the cell's finger and absorption of laser light by the Rb electrons is measured by an optical spectrometer.

4.1.1 Polarizing Cells and ^{3}He Filling Station

Recall from Eq. 1.26 that ^{3}He polarization increases monotonically with T_1. The T_1 for pure ^{3}He in the absence of collisions with walls is approximately 80 hours. In a 45 mL cylindrical glass cell (Figure 4.2), collisions with the container's walls become the dominant relaxation mechanism, and T_1 is typically reduced to 10 to 30 hours for a well made cell. In the presence of even minute amounts of oxygen, T_1 is drastically reduced to tens of seconds. Keeping the cells free of oxygen is, therefore, a very important consideration in both the initial manufacturing of the cell and in its periodic refilling.

Over time a cell's intrinsic T_1 decreases, often gradually, but sometimes suddenly. Once T_1 drops below around 6 hours, the cell becomes incapable of producing polarization levels sufficient to produce quality ^{3}He diffusion images. New cells must, therefore, be manufactured periodically in order to replace these old "dead" cells.

The cells are initially hand blown from Borosilicate glass (Pyrex) and attached to a glass manifold (see Figure 4.3). The manifold serves as the path by which Rb is deposited into the cells. A vacuum system is attached to one end of the manifold and 1 g of solid Rb is dropped in through a vertical opening at the opposite end. The cells are attached to the manifold by a thin 1.5" long glass tube 16" and 22" from the vertical opening. In addition to a retort directly below the vertical opening, there are two additional retorts separated by 4". Rb is "chased" from one retort to the next by application of flame heat. At the temperatures produced by the flame heat, the Rb vaporizes and recondenses on the nearest cool piece of glass. Approximately 1/6 of the Rb is left behind in each retort in order to distill the Rb of impurities and around 250 g of Rb is distilled into each cell. Prior to this distillation process, but after the Rb is dropped into the manifold and the vertical opening is sealed, the manifold is evacuated to below 10^{-6} Torr, and the entire manifold, with the exception of the cell valves and the large Rb retort, is baked at 400 °C for 2-3 days in order to remove impurities trapped in the glass.

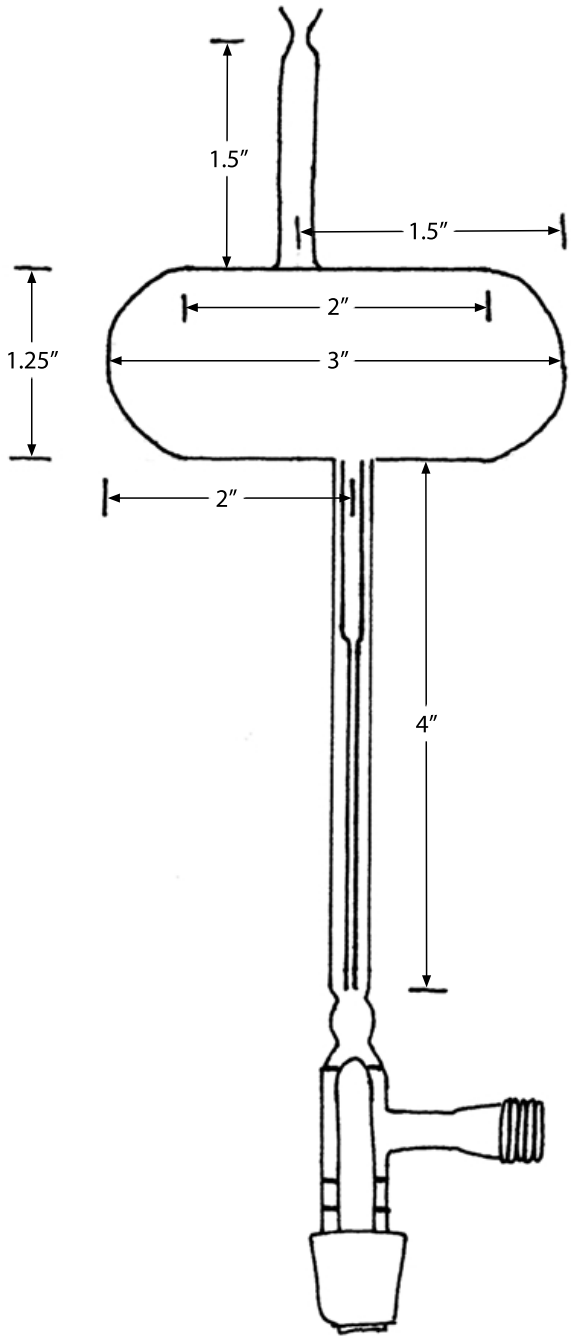

Figure 4.2: Typical glass cell used for ^{3}He polarization. The cell is filled and evacuated through the valve at the bottom. The 4" long small ID stem between the bulb and the valve allows for the solid Rb in the bulb to be heated without exposing the o-rings in the valve to high temperatures. The 1.5" finger located at the top of the diagram allows for polarization measurements with a small rf coil (see Figure 4.1).

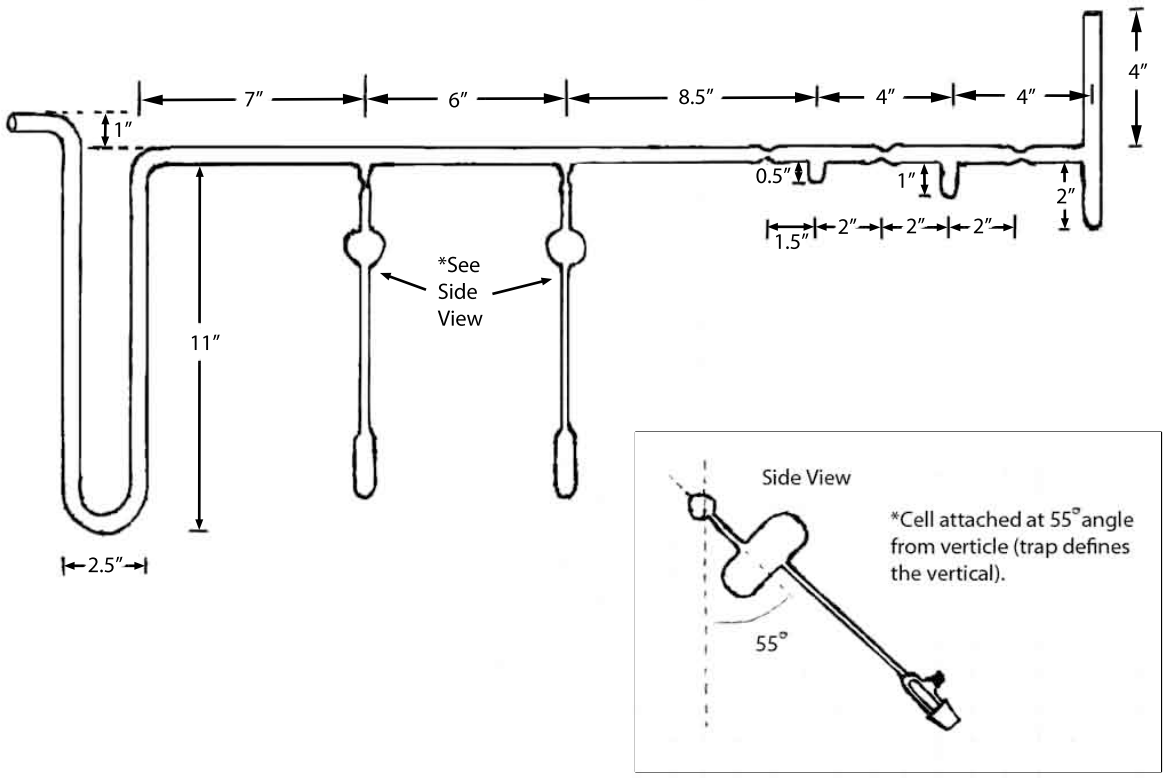

Figure 4.3: Glass manifold for cell production. A turbo vacuum pump is attached to the opening at the far left and the U-shaped trap is submerged in liquid nitrogen to increase the vacuum pump's effectiveness. A 1 g solid Rb ampule is dropped in the vertical opening at the far right and the opening is then flamed sealed. The entire manifold is heated to 400 °C while under vacuum for 2 days. After 2 days the Rb is chased into the cells and the cells are removed from the manifold and sealed by flame heat.

The cell's dimensions and short sausage shape (see Figure 4.2) were chosen to maximize the volume of Rb vapor illuminated by the diode laser array. The cell is evacuated and filled through a glass valve attached to the sausage bulb by a capillary tube, which is sufficiently long for the valve (and its o-rings) to remain outside the oven during the polarization process. The capillary tube's inner diameter is very small in order to reduce the volume of gas not participating in spin exchange during polarization. Additionally, the small tube by which the cells are initially attached to the manifold serves as a finger over which a

small rf coil is placed in order to periodically measure the FID during polarization. The initial amplitude of this FID serves as an indirect measurement of the ^{3}He's polarization.

The glass cell is refilled with 10 atm of ^{3}He after each use. A series of valves and charging volumes allows for the high-pressure gas in a 1/2-L lecture bottle to be incrementally transferred to the 45 mL glass cell. Prior to filling, the system is evacuated to between 10 to 30 mTorr and purged with N_2 three times in order to remove O_2 and other impurities from the system.

4.1.2 Diode Laser Arrays and Oven

After filling with 10 atm of ^{3}He, the cell is placed in an oven and heated to 165 °C in order to produce Rb vapor pressure. Each oven has several glass windows: one through which 794.7 nm light enters from the laser, one through which the light leaving the cell is monitored, and one or two additional windows for monitoring cell illumination. The cell bulb sits in an aluminum cradle with its long axis collinear with the laser and the valve resting several centimeters outside of the oven. The oven is mounted on a cart and sits between a pair of 60 cm-diameter Helmholtz coils, which provide an approximately 30 Gauss field at the location of the cells.

A diode laser array (Coherent, Santa Clara, CA and nLight, Vancouver, WA) emits 50 to 100 W of 794.7 nm light in the direction of the cell bulb. The horizontal array of diodes has high angular divergence in the vertical direction as well as smaller angular divergence in the horizontal direction. A series of cylindrical lenses, carefully placed between the laser and the cell, collimate the laser light so that most of the emitted photons pass through the cell. A quarter-wave plate, located between the laser and the oven, converts

the linearly polarized light emitted by the laser to σ+ circularly polarized light. The natural spectral width of all lasers is < 3 nm. At the time of this study, one of the three diode lasers was line narrowed via a Volume Bragg Grating system (PD-LD, Pennington, NJ) reducing its spectral width to < 0.4 nm. Three lasers, mounted on two carts, were capable of polarizing three 45 mL cells simultaneously.

4.1.3 Commercial Polarizer

A second, commercial IGI.9600.He polarizer (GE Healthcare, Durham, NC) is located within 50 meters of the MR scanner on the Washington University Medical School Campus. Functionally, the system is very similar to system described above. The two main differences are: (1) the GE system is designed to polarizer 1-L of ^{3}He in a single 120 mL spherical cell and (2) the system is designed such that the cell remains in the oven at all times during normal operation. Consequently, the ^{3}He filling system is integrated into the polarizer cart allowing the cell to be filled without removing it from the oven. As a result, the GE cart must be located close enough to the scanner such that polarized gas can be transported from the polarizer to the scanner by foot in under 30 seconds.

4.2 MR Scanner Hardware

All MR images were acquired in a 1.5 T Siemens Magnetom Sonata whole-body multi-nuclear scanner at 48.47 MHz (^{3}He) and 63.63 MHz (^{1}H). All dynamic ^{3}He lung morphometry scans were acquired on a 1.5T Siemens Avanto scanner. Explanted lung images were acquired using an in-house-built, solenoid-like rf coil constructed out of copper tape attached to poster board. The LC circuit includes a variable capacitor allowing for small

manual adjustments of its resonance frequency. These adjustments were typically required prior to each imaging session. All *in vivo* studies were performed with a custom-built ^{3}He volume-transmit/8-channel receiver pair (Stark Contrast MRI Coils Research, Erlangen, Germany).

4.3 Hyperpolarized Gas Transport, Lung Ventilation, and ^{3}He Recycling

While the Earth's 0.5 G magnetic field is sufficient to remove the spin degeneracy and sustain a polarized state, a larger magnetic field produces a larger difference in spin-up and spin-down energy levels and a corresponding increase in T_1. In order to minimize polarization loss due to T_1 relaxation, the cells containing the ^{3}He gas polarized in Compton Laboratory were transported the 3 miles to the MR scanner in a portable 35 G magnetic field. This field was created by a 50 cm long, 10 cm diameter, 3000 turn solenoid and powered by a 12 V battery (30). The portable 35 G field also served as temporary storage vessel during experimental preparations prior to ^{3}He imaging.

As previously noted, the presence of paramagnetic O_2 greatly reduces the T_1 relaxation time for ^{3}He. It is, therefore, important to eliminate the introduction of O_2 whenever possible. For *in vivo* human imaging, O_2 must inevitably be present during lung ventilation. One advantage of imaging explanted lungs, however, is that O_2 can be purged from the organ prior to ventilation. After explantation, a gortex sleeve was surgically attached to the explanted lung's main bronchus. The opposite end of the gortex sleeve was secured to a double-sided 1/2" nylon barbed fitting with a pair of cable ties. Prior to imaging the lung was connected to the ventilation system shown in Figure 4.4 ventilated with N_2 and

allowed to passively collapse 5 – 10 times in order to purge the lung and ventilator system of O_2.

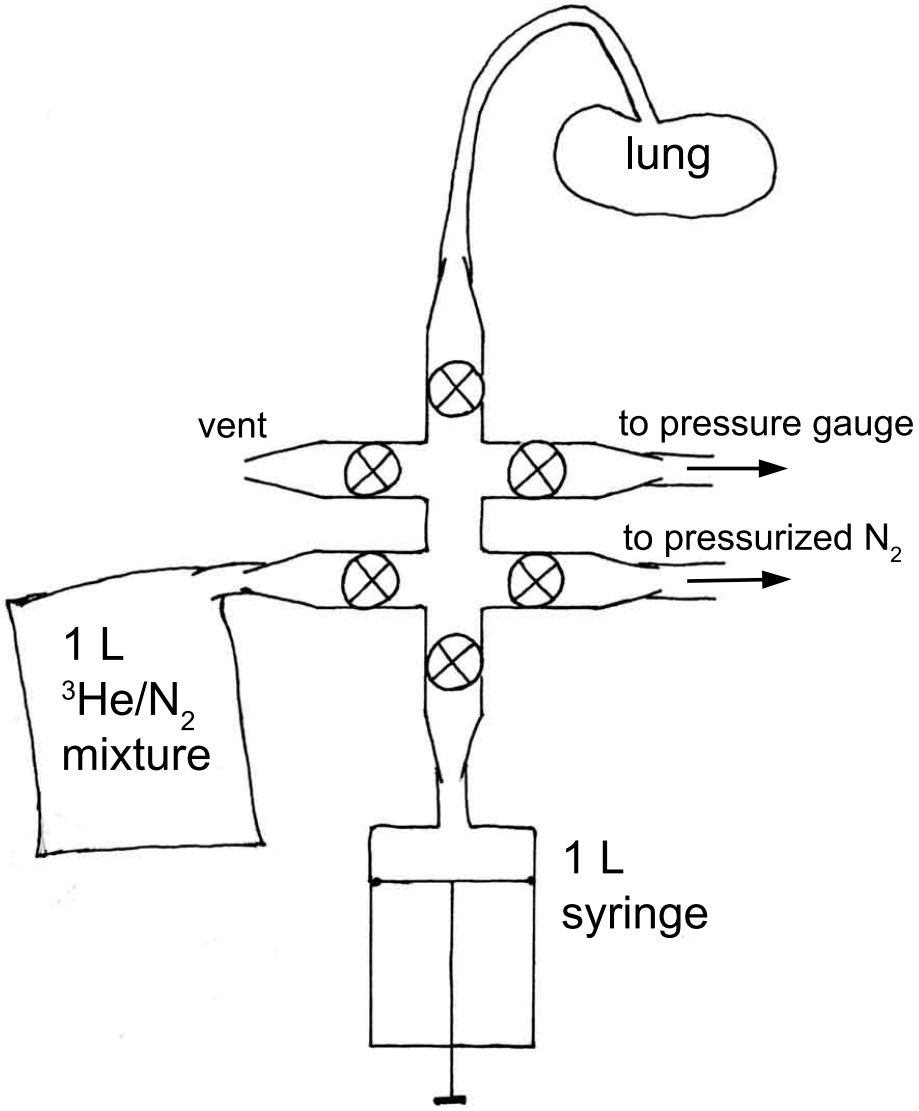

Figure 4.4: Ventilation system for purging and ventilating explanted lungs. During O_2 purging, the 1 L syringe is filled with pressurized N_2. The valve to the pressurized N_2 is then closed, the valves to the lung and pressure gauge are opened, and the N_2 is pushed into the lung with the 1 L syringe at a rate so as not to exceed a pressure of 23 cm. H_2O. The lung is then allowed to passively deflate by opening the vent valve. The process is repeated 5 to 10 times prior to ventilation with ^3He. Just before imaging, the 1 L bag containing the $^3He/N_2$ mixture is attached to the ventilation system and the gas is pulled into the syringe. The valve to the 1 L bag is then closed, the $^3He/N_2$ mixture is pushed into the lung, and the imaging sequence is initiated.

After thorough purging with N_2, 400 mL (STP) of ^3He was transferred from a cell to a 1-L polyethylene bag containing approximately 600 mL of N_2. Once filled, the polyethylene bag was connected to the ventilation system, its contents were transferred to a 1-L syringe, and the lung was inflated with the $^3He/N_2$ mixture using the syringe.

Prior to static *in vivo* MRI scans, human subjects were given a nose clip and a snorkel-like mouthpiece connected to a 50 cm long flexible tube. The polyethylene bag containing the $^3He/N_2$ mixture was attached to the tube immediately prior to ventilation. Polyethylene bags were filled with N_2 and ^3He directly from the commercial polarizer's ^3He filling system. The gas was quickly transported to the MR scanner by foot.

The dynamic breathing procedures were aided with the ventilation system shown in Figure 4.5. As with the static *in vivo* MRI scans, subjects breathed through a snorkel-like mouthpiece and the $^3He/N_2$ gas mixture was initially delivered in a 1-L polyethylene bag. Prior to the scan, the lungs' contents were evacuated into the 1-L and 4-L polyethylene bags. Inspired and expired gas volume was determined at 20 ms intervals using a pneumotachometer (Hans Rudolph).

After each *in vivo* ^3He MR image acquisition, the subject exhaled into a large ^3He recovery bag. After all images had been acquired, the contents of the ^3He recovery bag were evacuated into a long term ^3He storage tank. Once this tank reaches its capacity, the contents will be separate by cryogenic distillation and the ^3He will be recompressed for future use.

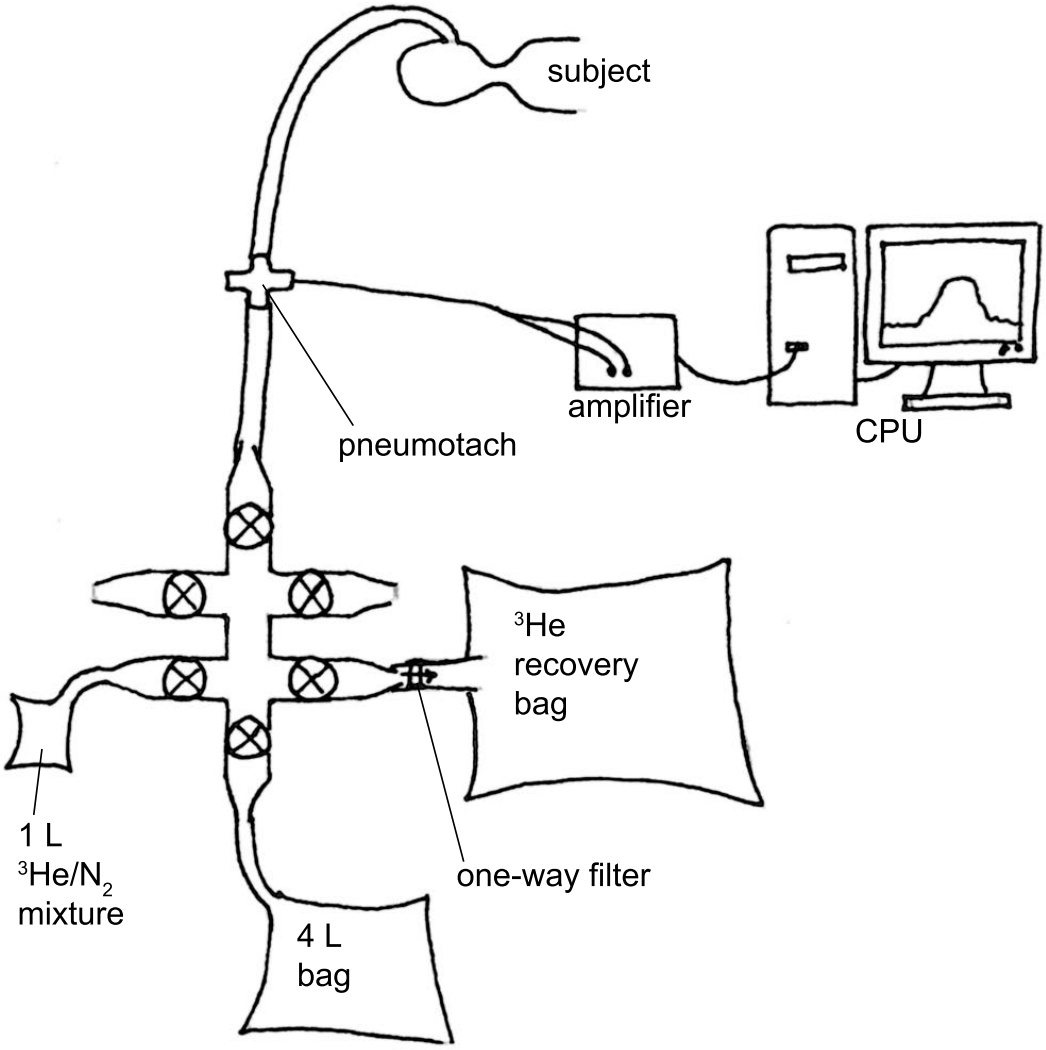

Figure 4.5: Ventilation system for delivering and recovering gas during dynamic ^{3}He lung morphometry scans. Just after a resting breath out, the subject inhales the contents of the 1 L ^{3}He/N_2 mixture bag. The subject is then instructed to exhale to residual volume (RV) into the 1 L and 4 L bags. The MR scan sequence is initiated and the subject begins inspiration (from the 1 L and 4 L bags) to total lung capacity (TLC). If the 1 L and 4 L bags are emptied before the subject reaches TLC, an additional vent valve is opened. During expiration back to RV, all valves are closed except for the valve to the ^{3}He recovery bag. Gas flow and volume to and from the subject is measured with the pneumotachometer and recorded with a CPU.

Chapter 5: Methods

5.1 Imaging Strategies

Because hyperpolarized ^{3}He exists in a non-equilibrium state, each rf pulse depletes a fraction of the gas's unrecoverable polarization. The fraction of polarization remaining after a single rf pulse is given by cos(α), where α is the rf flip angle. On the other hand, for each line of k-space, the NMR signal generated by a flip angle of α is proportional to sin(α). Larger flip angles give higher signal, but deplete the polarization more quickly. Smaller flip angles conserve polarization, but result in lower NMR signal. An appropriate value for the flip angle is chosen so as to maximize the NMR signal of each line of k-space while leaving enough polarization for subsequent acquisitions. This strategy is very different from non-hyperpolarized NMR where multiple 90° flip angles can be employed because a sample's polarization recovers to its Boltzmann equilibrium with a time constant T_1.

In a typical ^{3}He diffusion scan, each image slice is acquired with 40 lines of k-space. In this study, diffusion attenuation was measured with 9 b-values for the explanted lungs and 6 b-values for the *in vivo* scans resulting in acquisitions of between 240 and 360 lines of k-space for each image slice. If a minimum fraction of initial polarization P_f/P_0 is required for the final line of k-space, the required flip angle, α, is given by the solution to Eq. 5.1:

$$\frac{P_f}{P_0} = \cos(\alpha)^n \qquad 5.1.$$

For instance, in order to acquire the last line of k-space with final polarization level equal to 30% of the initial polarization level after previously acquiring 359 lines of k-space, a 5° flip angle must be used. In this study, multiple-b value diffusion images are acquired with rf flip angles between 5° and 8°.

A second consideration unique to pulmonary MR imaging with hyperpolarized gas is that the total image acquisition time must be short, particularly for *in vivo* scans. The reduced ^3He T_1 in the presence of O_2, requires that a scan be completed in under a minute for explanted lungs and shorter for *in vivo* scans. *In vivo* scans are typically acquired while a subject holds his or her breath, requiring that the total scan time be less than around 10 seconds. This constraint is satisfied by using short repetition times between rf pulses and acquiring low-resolution images and a small number of slices. In this study explanted lung images were acquired with between 24 and 40 lines of k-space and between 5 and 11 slices. All *in vivo* images were acquired with 40 lines of k-space and 3 slices. All MR scans were acquired with a 13 ms repetition time.

5.2 Explanted Lungs

Normal lungs were explanted from six dogs after sacrifice following unrelated cardiac experiments; approval was obtained from the Washington University Animal Studies Committee. All dogs were purpose-bred adult (usually over 8 months of age) mongrel hounds (male and female) weighing between 20 and 25 kg with no pulmonary abnormalities. A single lung was removed from Dogs 1-4, while both left and right lung were removed from Dog 5 and Dog 6. Three normal human donor lungs rejected for lung transplantation due to recipient complications were also acquired and studies performed with these lungs were done so with the approval of the Institutional Review Board (IRB). The main bronchus of each explanted lung was cannulated and all leaks were repaired prior to imaging.

5.2.1 Diffusion MR Imaging

Before imaging, each lung was filled with N_2 and passively deflated 5 to 10 times in order to purge the lung of O_2 and increase the ^3He T_1 relaxation time. While purging, each lung was gently massaged during inflation to ensure that all visible atelectatic regions were well ventilated prior to imaging. The lung was then placed in the MR scanner and ventilated with a syringe containing approximately 400 mL of ^3He and 600 mL of N_2 to a maximum transpulmonary pressure of 23 cm H_2O. Nuclear spin polarization was approximately 35% for all experiments. The gas mixture was then partially evacuated by free collapse to obtain one of three desired pressures (approximately 18, 7.5, or 2.5 cm H_20) and imaged at near-static pressure for between 15 and 50 seconds. This process was repeated a total of three times in order to obtain images at high, medium, and low levels of lung inflation.

Diffusion weighted images were acquired with the two-dimensional gradient echo pulse sequence described in section 1.3. For all experiments the timing parameters were kept constant (τ = 0.3 ms, $\delta = \Delta$ = 1.8 ms) while G_m was varied in order to produce a complete set of multiple-b-value, diffusion-weighted images at each inflation pressure. Nine diffusion-weighted images were obtained for all slices at each inflation pressure using values of b ranging from 0 to 14 s/cm^2. Slices were each 30 mm thick with an in-plane resolution of 5 mm x 5 mm. For each set of images, the field of view and number of slices were sufficiently large to contain the entire lung so that the volume of the lung could be measured from the MR images. Each lung's reported high volume (HV) corresponds to a pressure for which there was no visual change in lung volume for incremental increases in pressure. This volume is nearly equal to the lung's volume at total lung capacity (TLC).

For each voxel, Eq. 2.3 was fit to the diffusion attenuated MR signal with the relationships between the anisotropic diffusion coefficients, D_T and D_L, and the geometric parameters R and h specified by either the canine morphometric model (described in section 2.3) for canine lungs or the human morphometric model (described in section 2.2) for human lungs. Voxels containing large airways or with insufficient SNR were not analyzed, and voxels with poor fitting confidence were excluded from all images and reported averages. For each voxel, ADC was calculated from Eq. 2.4. Using the geometric parameters R and h determined by ^{3}He lung morphometry, the alveolar surface area, S_a, and volume, V_a, were calculated from Eqs. 1.27 and 1.28 and the total number of alveoli at each lung volume was determined from Eq. 1.33.

For each lung at each volume, values of R, h, S_a, V_a, and ADC from all voxels included in the analysis were averaged. For the canine morphometric results, the significance of the effects of lung volume on the parameters R, h, S_a, V_a, ADC, and N_{tot} were determined for all 6 lungs by performing repeated measures analysis of variance (ANOVA). Comparisons between each pair of lung volumes were performed using paired t-tests. P-values < 0.05 were considered statistically significant.

5.2.2 Histology

After imaging, the right and left lungs from Dog 5 and Dog 6 were frozen at different levels of deflation for quantitative histological studies. Each lung from the pair was first inflated to 23 cm H_20 and then passively deflated to the desired pressure and suspended at constant pressure in cold N_2 vapor (over a bed of LN_2) in an insulated container for 30 minutes (65). The left lungs from Dog 5 and Dog 6 were frozen at the pressure

corresponding to each lung's high volume from the MRI experiments, and the right lungs were frozen at pressures corresponding to low volumes from the MRI experiments. Each lung was then cut and sampled while frozen over dry ice, and each sample was sectioned at 6 microns for immunohistochemistry (in this case a Hart's stain) to distinguish elastic fibers (13).

Low resolution (5X) microscope images were acquired across the entire slide. These images were seamlessly stitched together using Adobe Photoshop and saved as a composite image of the whole slide. By serial sectioning, in most cases it was possible to distinguish acinar airways that were parallel, perpendicular, and at oblique angles relative to the slide. All airways deemed to be perpendicular (which are subject to the least error in transverse measurements) within the 2 cm x 2 cm sample were then measured for morphometric parameters *R* and *h* using ImagePro Plus software. Shrinkage was accounted for by measuring several dimensions of the cut samples before and after histological processing. A total of 550 measurements were made in 62 different airways in the two lungs frozen at high inflation and 689 measurements were made in 74 different airways in the two lungs frozen at low inflation.

5.3 *In vivo* Human Lung Diffusion MR Imaging

Five healthy subjects (2 male, 3 female) between the ages of 22 and 32 (mean age 27 ± 4) received proton and multiple b-value ^{3}He diffusion MRI scans at three distinct and reproducible lung volumes. Scans at each lung volume were acquired during a breath-hold following a breathing routine specific to each volume. Low lung volume scans were acquired by instructing the subject to exhale fully to residual volume (RV) and then inhale

the contents of a 1-L bag filled with either air (for proton scans) or a $^3He/N_2$ mixture (for ^3He scans). After breathing in the bag's contents, the MR scan was immediately initiated and the subject held his/her breath for the duration of the scan (approximately 10 seconds). Medium lung volume scans were obtained in a similar manner, but the 1-L gas mixture was administered immediately after expiration during a resting breathing cycle (adding 1 L to functional residual capacity, FRC). High lung volume scans were acquired by having the subject breath in the 1-L gas mixture immediately after expiration during a resting breathing cycle and then continue to inhale room air until total lung capacity (TLC) was achieved. In this way proton and ^3He diffusion MR images were obtained at volumes corresponding to residual volume + 1 L (RV+1), functional residual capacity + 1 L (FRC+1), and total lung capacity (TLC).

All measurements of total lung volume were made from higher resolution 2D multi-slice axial proton images (128 x 128; resolution= 3.52 x 3.52 x 15 mm; 21 slices completely covering both lungs from each subject) by semi-automated segmentation with the image processing program ImageJ (National Institute of Health). Armstrong *et al.* report that at FRC tissue accounts for 19% of total lung volume (3). For each subject, 1 L was subtracted from the measured lung volume at FRC+1, and 19% of this value was taken as the lung tissue volume for that subject. This tissue volume was subtracted from each lung volume (RV+1, FRC+1, TLC) and an additional 150 mL was subtracted to account for conductive airspace volume (64), so that all reported volume measurements represent gas volume of the diffusion region of the lungs. In order to determine the reproducibility of the breathing routines, each routine was repeated 5 additional times at each of the three volumes (TLC, FRC+1, and RV+1) in subjects 1 and 2. Proton images were acquired following each of

these additional breathing routines, and the volume was measured in the manner described above. The standard deviations of the five additional measurements at each lung volume are reported in Table 6.4 and demonstrate excellent reproducibility of both the breathing routines and the lung volume measurements.

Axial two-dimensional ^{3}He diffusion images (64 x 40; resolution = 7 x 7 x 30 mm; 3 slices) were acquired with a multiple b-value gradient echo pulse sequence (b = 0, 2, 4, 6, 8, and 10 cm^2/s, τ = 0.3 ms, $\delta = \Delta$ = 1.8 ms). For each voxel, Eq. 2.3 was fit to the diffusion attenuated MR signal with the relationships between the anisotropic diffusion coefficients, D_T and D_L, and the geometric parameters R and h specified by the human ^{3}He lung morphometric model described in section 2.2. Voxels containing large airways or with insufficient SNR were not analyzed, and voxels with low fitting confidence were excluded from all images and reported averages. Using the geometric parameters R and h determined by ^{3}He lung morphometry, the alveolar surface area, S_a, alveolar volume, V_a, total number of alveoli, N_{tot}, and the total lung tissue surface area, S_{tot} was calculated as described in section 1.5.

All ^{3}He/N_2 gas mixtures contained approximately 400 mL of ^{3}He and 600 mL of N_2. Nuclear spin polarization was approximately 35% for all experiments. Exhaled gas was captured in a helium-impermeable bag for ^{3}He recycling. All procedures were performed with IRB approval and ^{3}He IND exemption. Written informed consent was obtained from all subjects before participation in the study.

For each pair of lungs at each volume, the values of R, h, S_a, V_a, and ADC from all analyzed voxels with sufficient fitting confidence were each averaged. The statistical significance of the effects of lung volume on all parameters was determined for all 5 subjects

by performing repeated measures ANOVA. Comparisons between each pair of lung volumes were performed using paired t-tests. P-values < 0.05 were considered statistically significant.

5.4 Dynamic ^{3}He Diffusion MR

The insight into lung micromechanics gained from the experiments described above is ascertained from 3 static snapshots of lung microstructure during either the inflation or deflation leg of the breathing cycle. An ideal study of lung microstructure would, however, acquire measurements throughout both the inflation and deflation legs of the breathing cycle. Due to the high cost and scarcity of ^{3}He and the time required to prepare hyperpolarized gas, such an experiment, if performed with static diffusion MR images as described above, would be very costly and time consuming. If, on the other hand, MR diffusion scans are acquired *during* a single breathing cycle (rather than at static volumes), microstructure could be measured at several points during both inflation and deflation using a single dose of ^{3}He over the duration of a single breathing cycle.

The diffusion pulse sequence requires a minimum acquisition time of 13 ms for each line of k-space, so that acquiring a full set of 6 b-value scans for a single line of k-space requires a minimum scan time of 72 ms. Thus, using a sufficiently large field of view and slice thickness, the acquisition of a single line at the center of k-space is capable of collecting anisotropic ^{3}He diffusion data over the entirety of a pair of lungs in under 100 ms. In healthy humans, both inspiration from RV to TLC and expiration from TLC to RV each typically occur over a duration of around 15 seconds. Using a single line of k-space, over 150 snapshots of lung microstructure could, theoretically, be acquired during each leg of the breathing cycle. In practice, the maximum number of snapshots is limited by the polarization

level of the ^{3}He and the high SNR required for performing the ^{3}He lung morphometry analysis.

In the final part of this study, dynamic ^{3}He lung morphometry was performed with 13 MR diffusion snapshots during each leg of the breathing cycle (inflation and deflation). Each snapshot consists of five 30 mm slices, each acquired with a single line of k-space, covering both right and left lungs entirely.

Dynamic ^{3}He diffusion scans were acquired over one full breathing cycle in 3 subjects (2 male and 1 female) between the ages of 23 and 30. Immediately prior to the scan, subject 1 and subject 3 were each instructed to breathe in the contents of a 1-L bag filled with 600 mL of ^{3}He and 400 mL of N_2 and then exhale to RV. The gas expelled during expiration was captured in the original 1-L bag and additional 3-L bag. Once the subject reached RV, the MR scan sequence was initiated and the subject immediately began inspiration to TLC. The ventilation system shown in Figure 4.5 allowed for simultaneous inspiration of the gas from the 1-L and 3-L bags (containing the previously expired ^{3}He) and room air. Once the subject reached TLC, he or she held his or her breath for the remainder of the first scan. A second dynamic ^{3}He MR diffusion scan sequence began immediately following the first at which time the subject immediately began expiration to RV.

Subject 2 was instructed to inhale the contents of the 1-L ^{3}He/N_2 bag and then continue inspiring until he reached TLC. Once the subject reached TLC, the first MR scan sequence was initiated and the subject immediately began expiration to RV. The expired gas was captured in the 1-L and 3-L bags. Once the subject reached RV, he held his breath until the first scan ended. A second scan sequence began immediately following the first at which time the subject immediately began inspiration to TLC. All procedures were performed with

IRB approval and ^{3}He IND exemption. Written informed consent was obtained from all subjects before participation in the study.

5 axial one-dimensional ^{3}He diffusion projections (64 x 1; resolution = 7.81 x 156.25 x 30 mm) were acquired with a multiple b-value gradient echo pulse sequence (b = 0, 2, 4, 6, 8, and 10 cm^2/s, τ = 0.3 ms, $\delta = \Delta$ = 1.8 ms). At RV each subject's pair of lungs contained less than 150 mL of ^{3}He, which, in most cases, resulted in insufficient SNR for fitting the morphometric model to individual voxels. In order to achieve the SNR required to fit the morphometric model to the data at low lung volumes, all voxels containing MR signal were summed over all 5 slices for each b-value at each of the 26 sets of scans and the human morphometric model was fit to the net signal from the entire lung. MR scans with low fitting confidence were excluded from the reported results. Using the geometric parameters R and h, the derived parameters S_a, V_a, and N_{tot}, were calculated as described in section 1.5 and ADC was calculated from Eq. 2.4.

Additionally, three static proton scan were acquired at RV, TLC, and FRC. The volume of gas at each of these inflation levels was determined in the manner described in section 5.3. The lung tissue volume was taken as 19% of the FRC volume measurement. A polynomial function was fit to each of the time dependent volume curves obtained by the pneumotachometer measurements. This volume was added to the gas volume at RV (as measured from the proton images) in order to determine the total lung volume at each of the 26 MR snapshots. Lung tissue volume and conducting airway volume (150 mL) were subtracted from the lung volumes at each time point so that the reported measurements indicate the volume of gas in the respiratory region of the lung.

Chapter 6: Results

6.1 Explanted Canine Results

6.1.1 ^{3}He Lung Morphometry

All canine lung images demonstrated high SNR resulting in high fitting confidence of the canine morphometric model for the large majority of voxels. Three series of diffusion attenuated lung images are shown in Figure 6.1 for each of the 9 b-values at three different levels of deflation. Corresponding parameter maps of *ADC* values based on voxel-by-voxel fits of Eqs. 2.3 and 2.4 are shown to the right in Figure 6.1 for each of the three lung volumes. An example of diffusion attenuated MR signal as a function of b-value is plotted in Figure 6.2 for three different levels of deflation along with the corresponding anisotropic fitting curves from Eq. 2.3. Histograms of *ADC* over all voxels at each of the three volumes illustrate a clear difference in airway sizes as expected (Figure 6.3).

All images were analyzed on a voxel-by-voxel basis and all voxels included in the analysis demonstrated more than sufficient signal-to-noise (>100 for b = 0 images) to confidently fit the canine morphometric model (Eqs. 2.13 – 2.17) to the data and obtain the geometric parameters R and h. Alveolar volume, V_a, and alveolar surface area, S_a, were calculated for each voxel from Eqs. 1.28 and 1.27. Additionally, the total number of alveoli, N_{tot}, was calculated from Eq. 1.33 using the total volume measurements obtained from the ^{3}He MR images. *ADC* values were calculated using Eq. 2.4. The average parameter values for each lung at each of the three lung volumes are shown in Table 6.1.

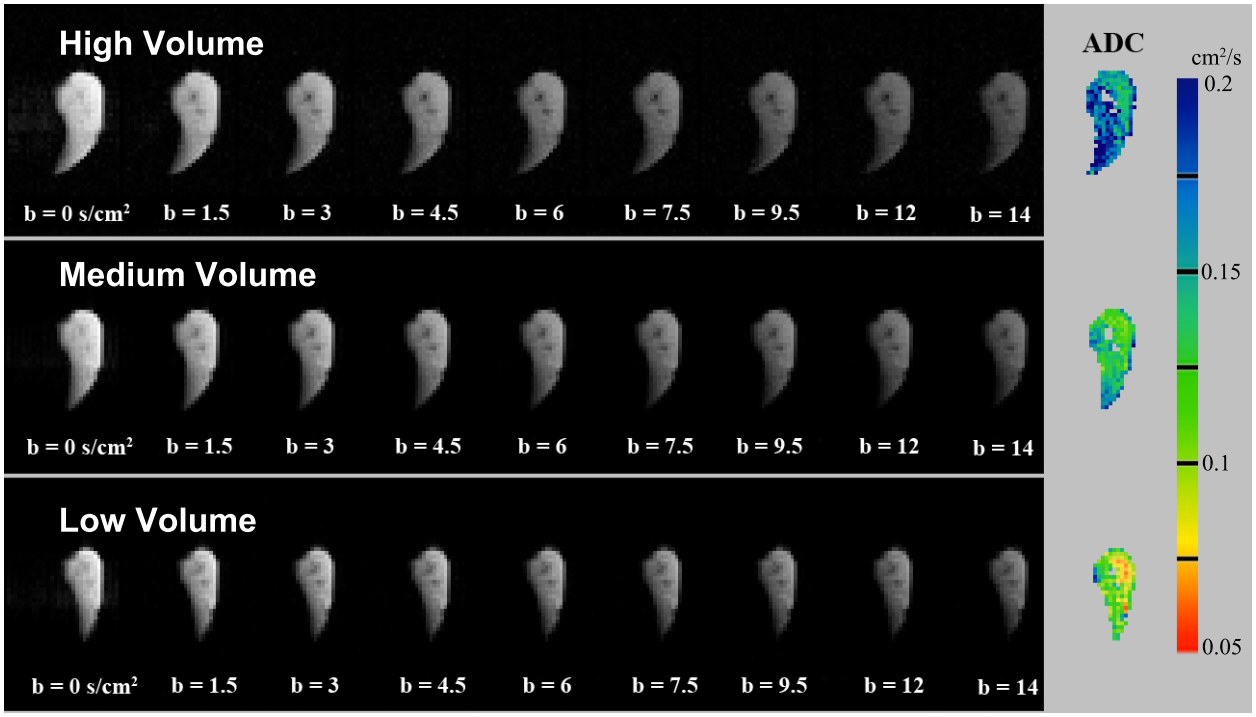

Figure 6.1: Diffusion attenuated images for b = 0, 1.5, 3, 4.5, 6, 7.5, 9.5, 12, and 14 cm^2/s (from left to right) at High Volume, Medium Volume, and Low Volume (top to bottom). *ADC* parameter maps are shown to the right based on voxel-by-voxel fits to Eqs. 2.3 and 2.4.

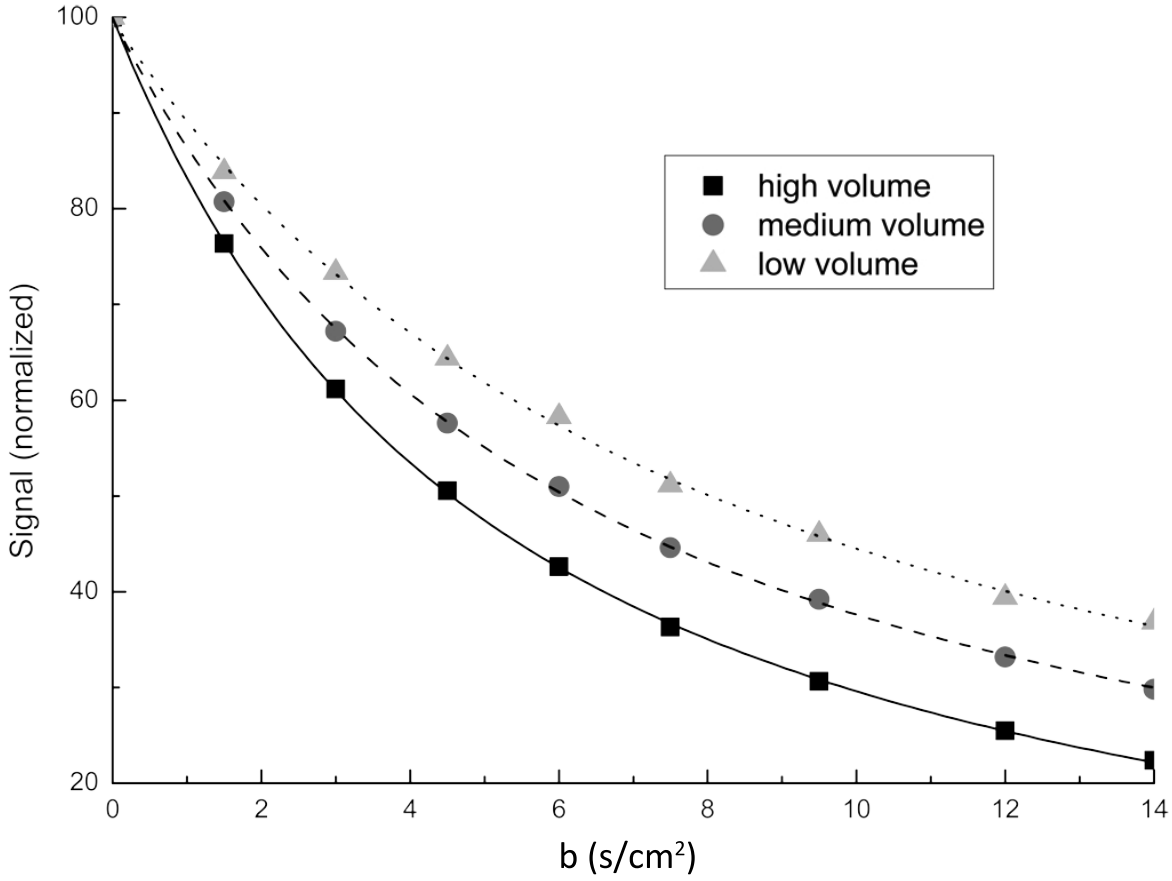

Figure 6.2: Normalized MR signal as a function of the bipolar diffusion gradient parameter, *b*, averaged over 4 voxels from Dog Lung 4 at high volume, medium volume, and low volume. The increased signal attenuation at high lung volumes is due to increased airspace volume relative to the diffusion length during the diffusion time Δ.

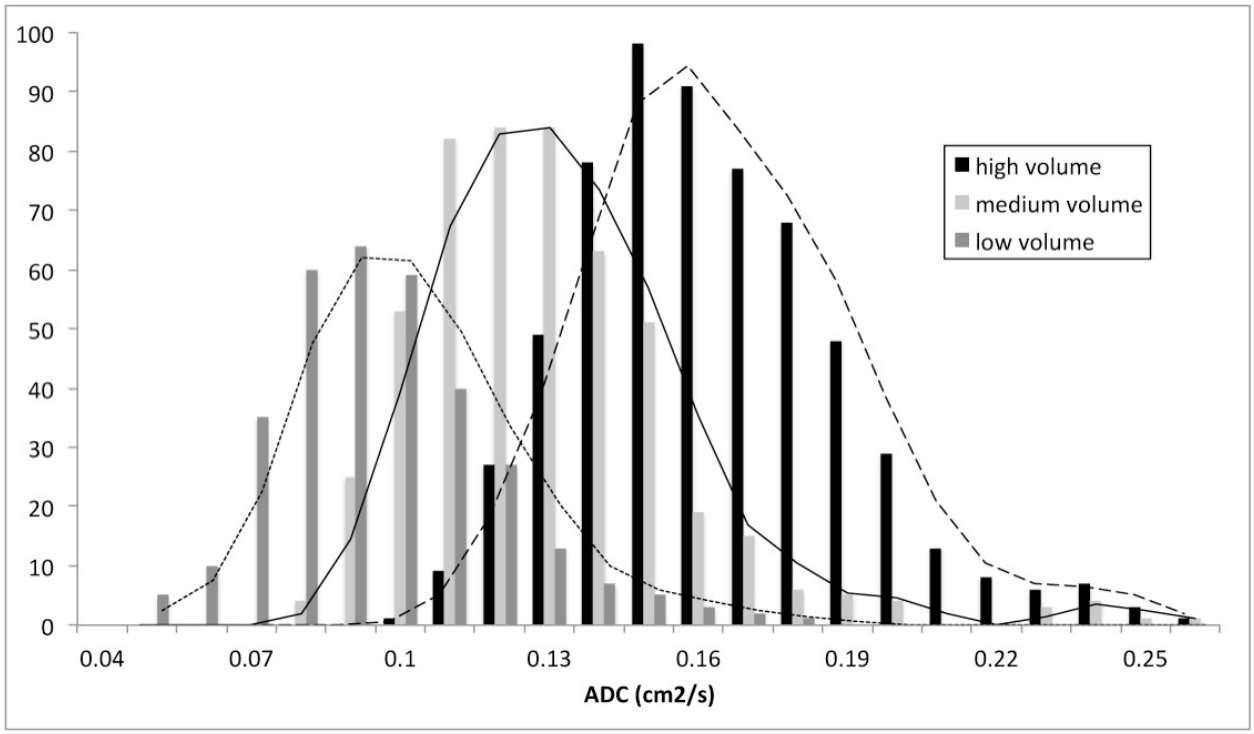

Figure 6.3: Histograms of ADC values from the parameter maps of Dog Lung 6 at high volume, medium volume, and low volume.

Each lung showed significant microgeometrical changes in R ($P < 10^{-6}$), h ($P < 0.01$), V_a ($P<10^{-5}$), S_a ($P<10^{-4}$), and ADC ($P<10^{-4}$) across all volumes via repeated measures ANOVA. On average a 46% decrease in total lung volume (high to low volume) led to a 18% decrease in R, an 11% increase in the alveolar depth h, a 40% decrease in alveolar volume, V_a, a 17% decrease in alveolar surface area, S_a, and a 38% decrease in ADC. ($P < 0.005$, $P < 0.05$, $P<0.005$, $P<0.05$, and $P<0.005$ respectively via paired t-tests). There was no significant change in the total number of alveoli across lung volumes ($P<0.05$). Differences between values of h at high and medium volumes were also not significant ($P > 0.05$); all other pairwise comparisons of R, h, V_a, S_a, and ADC at different volumes were significant (see Table 6.2).

Table 6.1: ^{3}He Lung Morphometry Canine Results

	Volume (L)	R (μm)	h (μm)	V_a (mm^3x10^{-3})	S_a (mm^2x10^{-2})	N_{tot} (10^6)	ADC (cm^2/s)
Dog 1							
HV	1.00	249±27	108±26	4.8±1.5	11.2±3.0	237	0.17±0.03
MV	0.72	238±37	97±31	4.3±2.0	10.1±3.9	223	0.18±0.03
LV	0.49	199±39	111±30	2.6±1.5	8.6±3.6	277	0.12±0.02
Dog 2							
HV	1.39	253±24	117±29	5.0±1.4	12.1±3.1	301	0.16±0.03
MV	0.83	230±39	122±38	4.0±1.9	11.1±4.5	283	0.14±0.03
LV	0.71	218±39	129±42	3.4±1.8	10.7±4.6	286	0.11±0.02
Dog 3							
HV	1.20	253±20	111±21	5.0±1.1	11.6±2.1	257	0.17±0.03
MV	0.97	224±34	114±29	3.6±1.5	10.1±3.3	348	0.14±0.03
LV	0.79	212±35	126±37	3.1±1.5	10.1±3.9	338	0.11±0.03
Dog 4							
HV	0.54	238±30	99±19	4.2±1.5	10.1±2.5	150	0.17±0.02
MV	0.34	227±35	99±21	3.7±1.6	9.5±2.9	116	0.16±0.02
LV	0.29	192±34	123±34	2.3±1.3	8.6±3.5	170	0.09±0.03
Dog 5							
HV	1.96	228±27	119±28	3.7±1.2	10.6±3.1	614	0.14±0.02
MV	1.32	207±32	114±28	2.9±1.3	9.2±3.2	597	0.12±0.02
LV	1.05	185±36	125±34	2.1±1.3	8.4±3.6	699	0.08±0.02
Dog 6							
HV	0.48	250±31	120±34	4.9±1.8	12.2±4.0	114	0.16±0.03
MV	0.36	233±32	131±34	4.0±1.7	11.6±3.9	108	0.12±0.03
LV	0.23	206±37	133±40	2.9±1.6	10.0±4.3	109	0.09±0.02
Average							
HV	1.09	245±10	112±8	4.6±0.5	11.3±0.8	279	0.16±0.01
MV	0.76	227±11	113±13	3.8±0.5	10.3±0.9	279	0.14±0.02
LV	0.59	202±12	125±8	2.8±0.5	9.4±1.0	313	0.10±0.02

Values for alveolar duct radius, R, alveolar depth, h, alveolar volume, V_a, alveolar surface area, S_a, total number of alveoli, N_{tot}, and apparent diffusion coefficient, ADC, for lungs from dogs 1 - 6 at High Volume (HV), Medium Volume (MV), and Low Volume (LV) averaged over all voxels. Values are reported as average ± SD. The last three rows are averages of mean results from all lungs ± SD in the means.

Table 6.2: Canine Statistical Tests

		Paired t-test		
	ANOVA	HV to LV	HV to MV	MV to LV
R	10^{-6}	0.003	0.001	10^{-6}
h	0.003	0.01	0.8	0.008
V_a	10^{-6}	0.004	0.002	10^{-6}
S_a	10^{-5}	0.01	0.002	0.0003
N_{tot}	0.14	0.11	0.99	0.11
ADC	10^{-5}	0.004	0.04	10^{-5}

P values for repeated measures ANOVA and paired t-test pairwise comparisons between High Volume (HV) and Low Volume (LV), HV and Medium Volume (MV), and MV and LV for *R, h,* V_a, S_a, N_{tot}, and *ADC*.

Within a particular lung, regional variations of each parameter were consistent across all volumes. For instance, if *ADC* values were larger in the apex than in the base at the high lung volume, they typically tended to also be relatively large at medium and low lung volumes, implying that these spatial variations were physiological. Figure 6.4 shows parameter maps of *R* and *h* for a representative slice from Dog Lung 6 at the high lung volume (HV), 78% HV, and 54% HV.

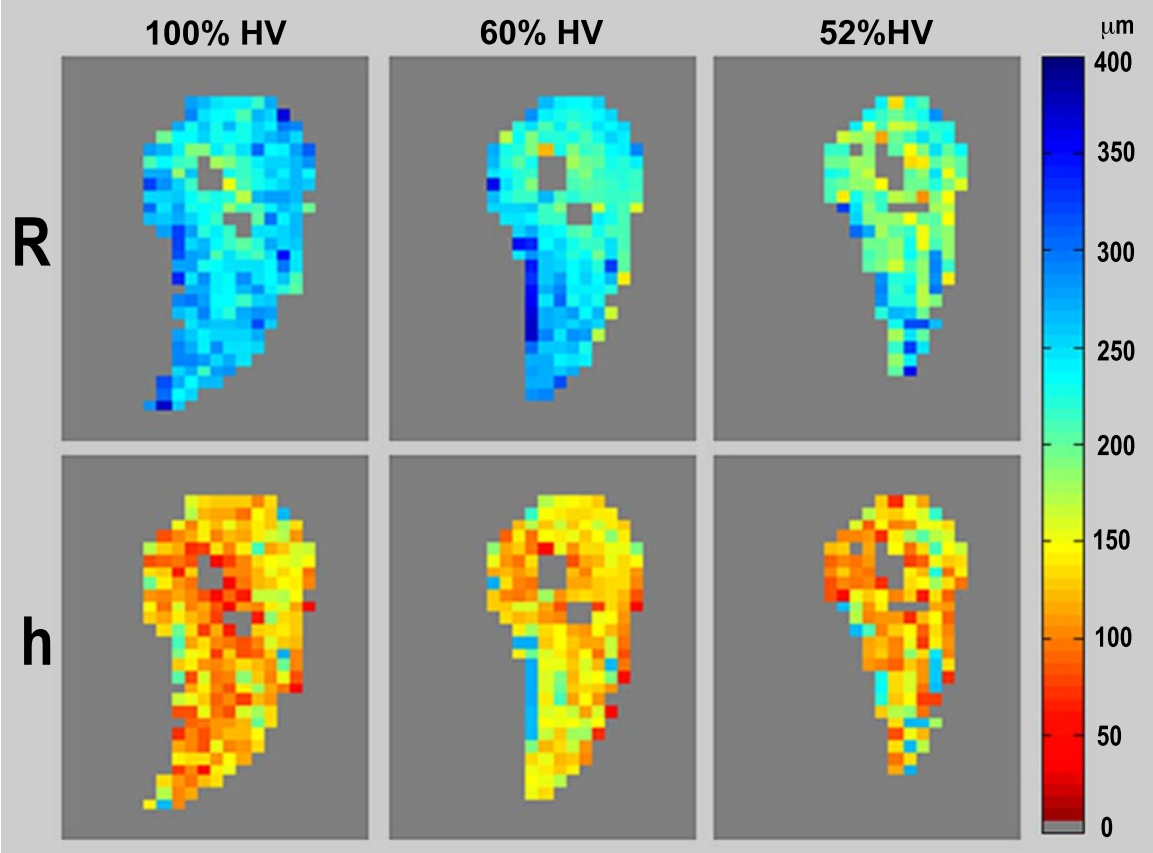

Figure 6.4: Transverse parameter maps for *R* and *h* in dog lung 6 at multiple volumes. Top row: R-map in microns at 100%, 60%, and 52% high-volume (HV) (L to R). Bottom Row: h-map at identical volumes. The value of each voxel in the above parameter maps represents the average value of *R* (top row) and *h* (bottom row) of all acinar airways within that voxel as determined by the multiple-b-value diffusion MR images. Major airways (gray in the center of the images) and voxels with low SNR and poor fitting confidence have been removed from the parameter maps.

6.1.2 Histology

From the composite histological images, all acinar airways judged by serial section to be perpendicular to the slide within each 2x2 cm sample were identified and measured for morphometric parameters *R* and *h*, after correcting for shrinkage (Figure 6.5). The shrinkage factor (post-processed sample size/pre-processed sample size) was 0.47 ± 0.03 (avg. ± SD). While serial sections reduce the probability of error, we note that our method for histological measurements of *R* and *h* are still subject to some error due to subjective judgments made in

determining which alveolar ducts are perpendicular enough to measure. A summary of the histology and MR measurements from the same lungs is shown in Table 6.3. The comparison is quite favorable, and in each case the difference between histology and MRI was well within one standard deviation of either average measurement.

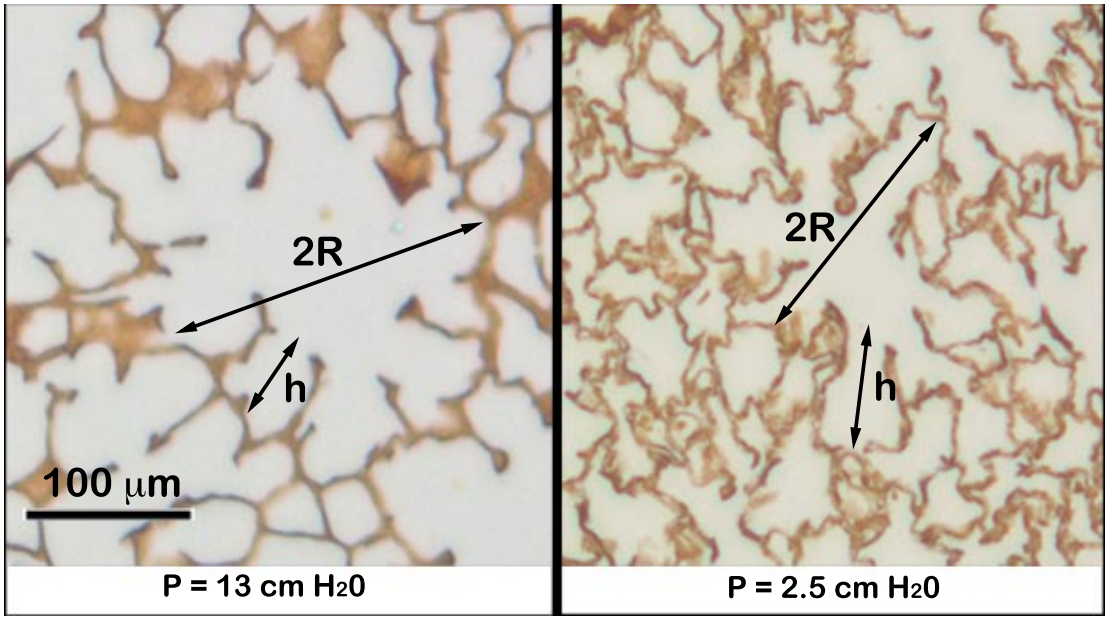

Figure 6.5: Acinar airways oriented perpendicular to the slide at two levels of inflation, viewed with a Hart's stain to distinguish elastic fibers.

Table 6.3: Comparison of histology and MR

	Histology		*^{3}He Morphometry*	
Volume	*R (μm)*	*h (μm)*	*R (μm)*	*h (μm)*
Dog 5				
High	224 ± 27	138 ± 21	228 ± 29	119 ± 29
Low	173 ± 24	116 ± 31	184 ± 38	124 ± 34
Dog 6				
High	243 ± 35	121 ± 44	249 ± 33	120 ± 34
Low	202 ± 25	107 ± 31	205 ± 40	133 ± 42

Histology values are averaged over all measurements ± SD.
^{3}He Morphometry values are averaged over all voxels ± SD.

6.2 Static Human *In vivo* ^{3}He Lung Morphometry Results

All *in vivo* human images demonstrated SNR more than sufficient to confidently fit the human morphometric model to the data in order to obtain the geometric parameters R and h. N_{tot} and average values of R, h, S_a, V_a, and ADC for each pair of lungs at total lung capacity (TLC), functional residual capacity + 1-L (FRC+1), and residual volume + 1-L (RV+1) are given in Table 6.4. Image voxels with SNR less than 100 or containing large conducting airways were not analyzed, and voxels with poor fitting confidence were excluded from all images and reported averages. After excluding voxels containing large airways and with low SNR, fewer than 2% of voxels were excluded due to poor fitting confidence. Typical parameter maps of h and R are shown in Figure 6.6. Each lung showed statistically significant microgeometrical changes with inflation across all volumes in R ($P < 0.001$), h ($P < 10^{-5}$), V_a ($P < 0.001$), N_{tot} ($P < 10^{-5}$), and ADC ($P < 10^{-6}$) via repeated measures ANOVA. On average a 143% increase in lung gas volume (from RV+1 to TLC) led to a 7% increase in alveolar duct radius, R, a 21% decrease in alveolar depth, h, a 19% increase in alveolar volume, V_a, a 96% increase in the number of alveoli, N_{tot}, and a 41% increase in ADC ($P < 0.001$, $P < 10^{-5}$, $P < 0.001$, $P < 10^{-5}$, and $P < 10^{-5}$ respectively via paired t-tests). All other pairwise comparisons of R, h, V_a, and N_{tot} were also significant ($P < 0.05$). There were no significant changes in the average alveolar surface area, S_a, between any of the three volumes ($P > 0.05$). P values for all statistical tests are reported in Table 6.5.

Table 6.4: Static ^{3}He Lung Morphometry *In vivo* Human Image Results

	Volume (L)	*R (μm)*	*h (μm)*	S_a (mm^2x10^{-2})	V_a (mm^3x10^{-3})	N_{tot} (10^6)	*ADC* (cm^2/s)
subject 1							
TLC	6.06±0.17	325±18	120±24	17.3±2.5	10.4±1.5	594	0.24±0.03
FRC+1	3.46±0.09	322±29	157±37	20.1±4.9	10.2±2.8	358	0.20±0.03
RV+1	2.59±0.04	317±32	169±40	20.6±5.3	9.9±3.1	284	0.18±0.04
subject 2							
TLC	5.23±0.02	318±22	130±20	17.7±2.5	9.8±1.2	536	0.22±0.02
FRC+1	3.55±0.03	307±20	153±24	18.4±2.8	8.8±1.4	412	0.18±0.02
RV+1	2.26±0.04	302±24	167±29	19.0±3.8	8.4±2.0	281	0.16±0.02
subject 3							
TLC	5.29	324±22	158±28	20.3±3.6	10.4±2.0	526	0.20±0.02
FRC+1	3.38	307±27	179±33	20.4±4.4	8.9±2.2	397	0.16±0.02
RV+1	2.02	300±30	193±37	20.6±5.0	8.3±2.4	262	0.13±0.02
subject 4							
TLC	5.91	324±20	141±23	19.0±2.9	10.3±1.8	585	0.22±0.02
FRC+1	3.45	314±20	152±25	19.0±3.2	9.4±1.7	377	0.19±0.02
RV+1	2.58	303±24	173±31	19.6±3.8	8.5±1.9	315	0.16±0.02
subject 5							
TLC	5.90	318±21	139±15	19.1±3.3	9.8±2.0	621	0.20±0.03
FRC+1	4.26	308±22	161±11	19.3±3.4	8.9±1.8	495	0.17±0.02
RV+1	2.21	289±28	177±11	19.1±4.1	7.4±1.9	321	0.13±0.02
average							
TLC	5.68	322±3	135±14	18.7±3.0	10.1±0.3	572±40	0.22±0.02
FRC+1	3.62	311±6	153±11	19.4±3.8	9.2±0.6	408±53	0.18±0.02
RV+1	2.33	302±10	167±11	19.8±4.4	8.5±0.9	293±25	0.15±0.02

Values for alveolar duct radius, R, alveolar depth, h, alveolar surface area, S_a, alveolar volume, V_a, total number of alveoli, N_{tot}, and apparent diffusion coefficient, ADC, for subjects 1-5 at total lung capacity (TLC), functional residual volume + 1 L (FRC+1), and residual volume + 1 L (RV+1) averaged over all voxels. Values are reported as average ± SD. The last three rows are averages of mean results from all lungs ± SD in the means. The SD obtained from volume measurements from 5 additional proton scans at each volume are reported for subjects 1 and 2.

Table 6.5: *In vivo* Human Statistical Tests

		Paired t-tests		
	ANOVA	**RV+1 -> TLC**	**FRC+1 -> TLC**	**RV+1 -> FRC+1**
R	0.0004	0.005	0.008	0.02
h	10^{-5}	0.0002	0.008	0.001
V_a	0.0006	0.007	0.01	0.03
S_a	0.10	0.13	0.21	0.09
N_{tot}	10^{-6}	10^{-5}	0.002	0.005
ADC	10^{-6}	10^{-5}	0.001	0.01

P values for repeated measures ANOVA and paired t-test pairwise comparisons between RV+1 and TLC, FRC+1 and TLC, and RV+1 and FRC+1 for *R, h,* V_a, S_a, N_{tot}, and ADC.

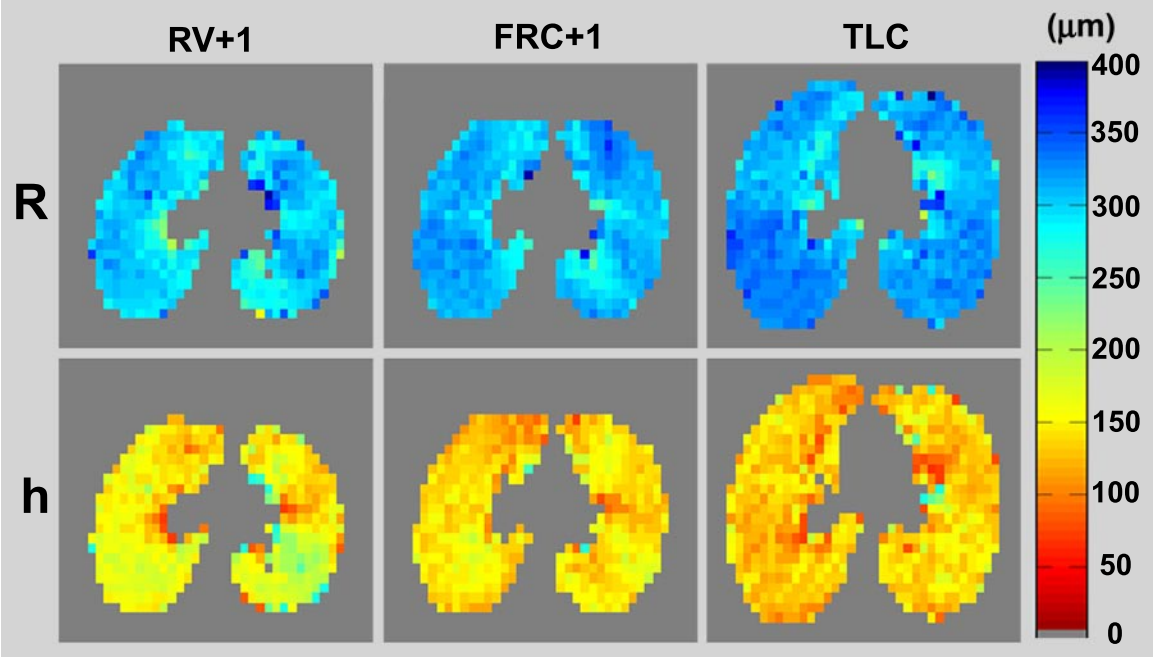

Figure 6.6: Axial parameter maps of alveolar duct radius, *R*, (top row) and alveolar depth, *h*, (bottom row) from slice 2 of subject 5 at RV+1, FRC+1, and TLC (L to R). The value of each voxel in the above parameter maps represents the average value of *R* (top row) and *h* (bottom row) of all acinar airways within that voxel as determined from the multiple-b-value diffusion MR images.

The standard deviations of the five additional proton image volume measurements at each lung volume for subjects 1 and 2 are reported in Table 6.4. The average standard deviation for each of these 6 sets of measurements was 50 mL (1.1%) and the maximum standard deviation was 169 mL (2.4%), demonstrating excellent reproducibility of the lung volume measurements and breathing routines.

In Figure 6.7, N_{tot} and average values of R, h, V_a, $V_{a,prop}$, $V_{a,lumen}$, S_a for all 5 subjects at each of the three volumes TLC, FRC+1, and RV+1 are each plotted against total lung gas volume, V_{tot}. Each data point represents the average parameter value over the entire pair of lungs for a single subject at the lung volume indicated by the horizontal axis. In Figure 6.8, total lung surface area, S_{tot}, is plotted against V_{tot} and the power function given in Eq. 3.1 is fit to the data.

For each parameter, averages from the anterior third, middle third, and posterior third of each of the five pairs of lungs at each of the three inflation levels were compared via repeated measures ANOVA to determine whether any parameters exhibited consistent significant gravitational dependence. No significant regional variation in the gravitational direction was measured in R, h, or ADC at TLC, however significant differences were measured in all three parameters at FRC+1 and RV+1. At FRC+1, in the anterior third of the lung the average ADC value was 19% larger, the average R value was 3% larger, and the average h value was 12% smaller than their respective values in the posterior third of the lung. At RV+1, ADC was 29% larger, R was 6% larger, and h was 8% smaller in the anterior third of the lung than in the posterior third of the lung. Plots for average values of R, h, V_a, S_a, and ADC as a function of position in the gravitational direction are shown in Figure 6.9.

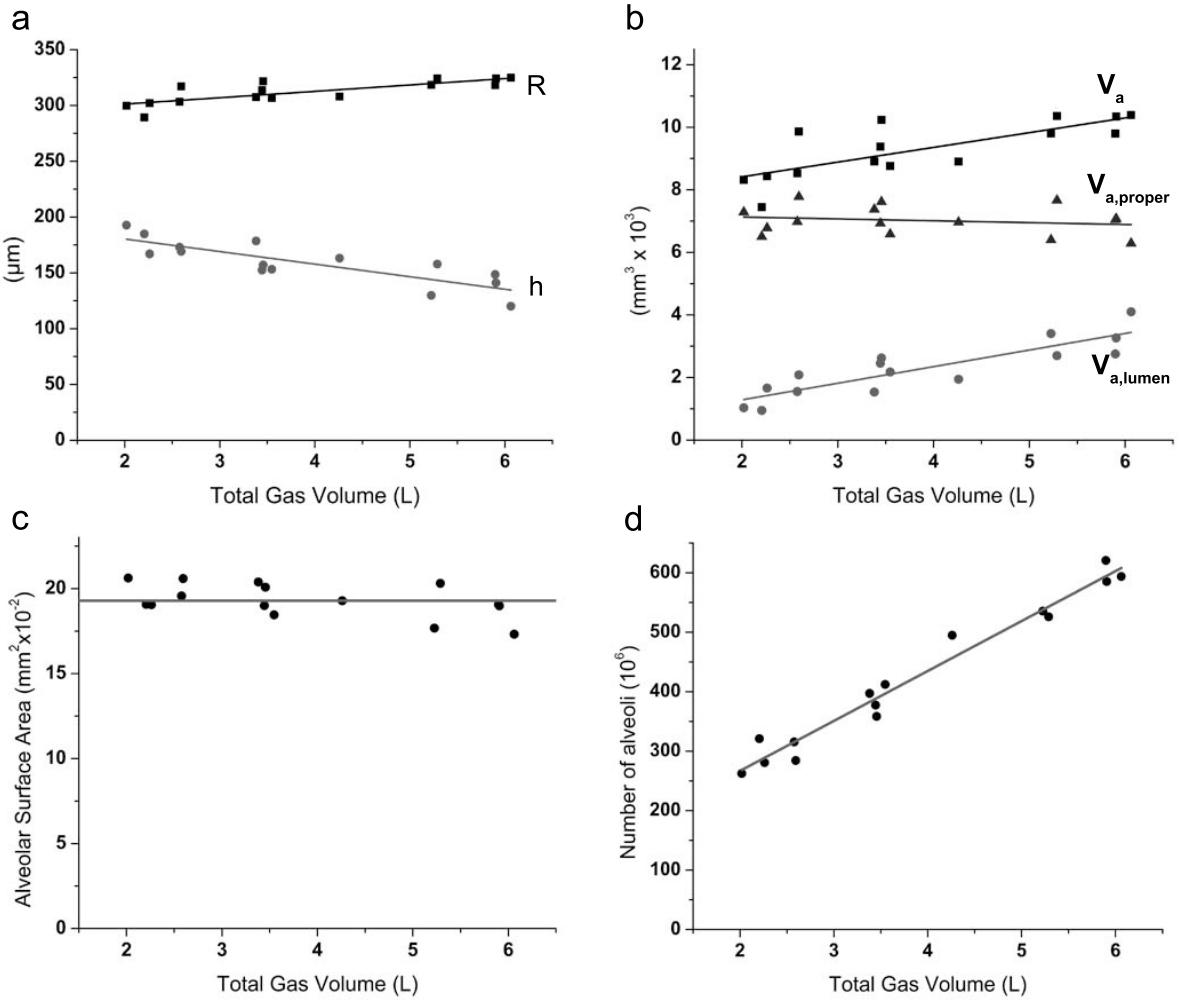

Figure 6.7: Microgeometrical parameters obtained by ^{3}He lung morphometry plotted against total lung gas volume for five subjects. Each data point represents a parameters value averaged over the entire lung for one subject at a particular lung volume. (a) Plot of average alveolar duct radius, R, and alveolar depth, h, versus total lung gas volume. Linear fits to the data give $R = 5.71V_{tot} + 290$ and $h = -11.3V_{tot} + 203$. (b) Plot of average alveolar volume, V_a, alveolar proper volume, $V_{a,prop}$, and one eighth alveolar lumen volume, $V_{a,lumen}$, versus total lung gas volume, V_{tot}. Linear fits to the data give $V_a = 0.47V_{tot} + 7.47$, $V_{a,proper} = -0.06V_{tot} + 7.25$, and $V_{a,lumen} = 0.53V_{tot} + 0.22$. (c) Plot of average alveolar surface area, S_a, versus total lung gas volume, V_{tot}. A constant line fit to the data gives $S_a = 0.193$ mm^2. (d) Plot of total number of alveoli, N_{tot}, versus total lung gas volume, V_{tot}. A linear fit to the data gives $N_{tot} = 98.8V_{tot}+84.0$.

Similar statistical tests were performed to compare morphometric differences in directions orthogonal to the sagittal planes (the read out direction) and in directions orthogonal to the transverse plane (the slice direction). In the read out direction there were

no significant differences in either *ADC* or *h* at any volumes. *R* was, on average, about 3% larger in the medial third of the lung than in the lateral third of the lung at all volumes ($P < 0.05$ via repeated measures ANOVA). Plots for average values of *R, h*, V_a, S_a, and *ADC* as a function of position relative to the mid sagittal plane are shown in Figure 6.10. No consistent statistically significant differences in any parameters were observed in the slice direction.

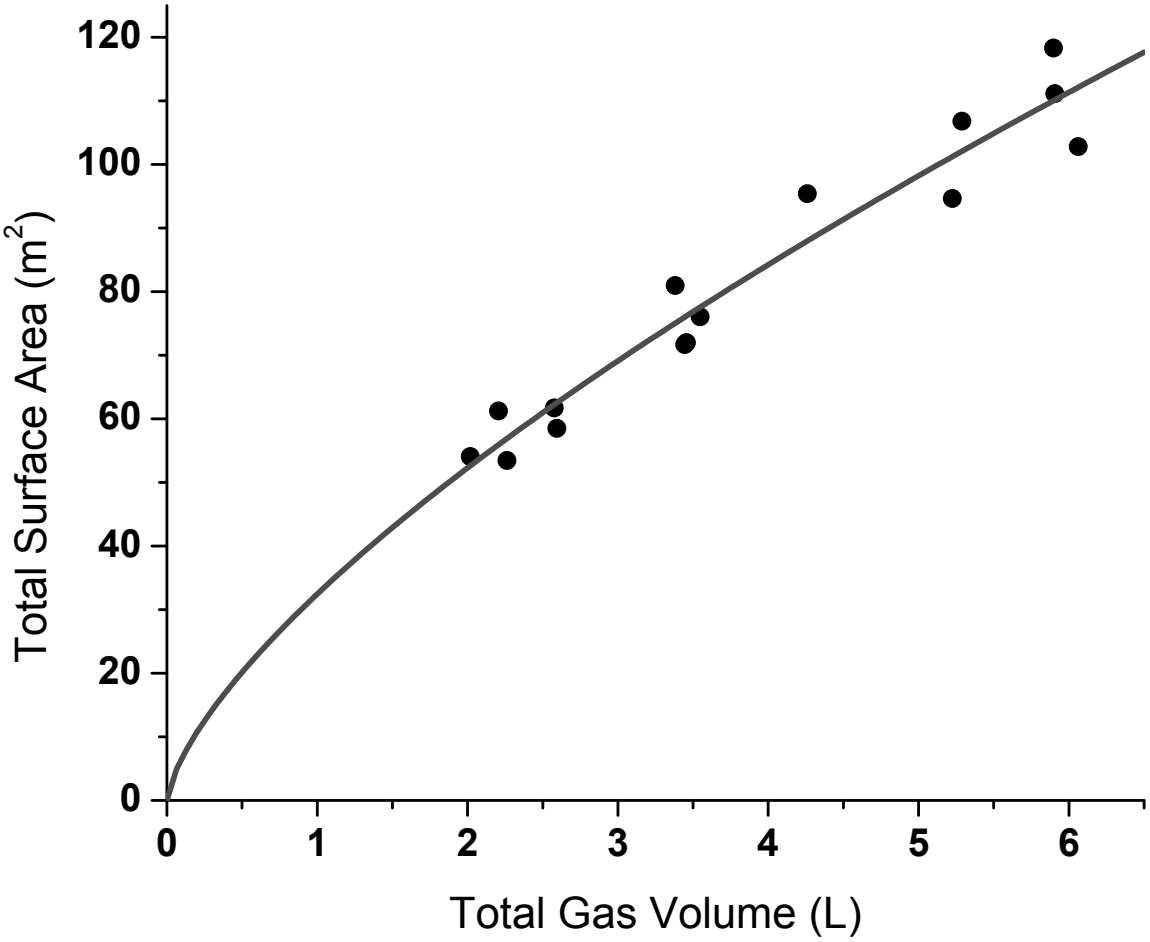

Figure 6.8: Plot of total surface area, S_{tot}, versus total lung volume, V_{tot}, for all 5 subjects at each of the three volumes TLC, FRC+1, and RV+1 with best fit curve for $S_{tot} = k\ V_{tot}^{\ n}$, ($n = 0.69 \pm 0.05$).

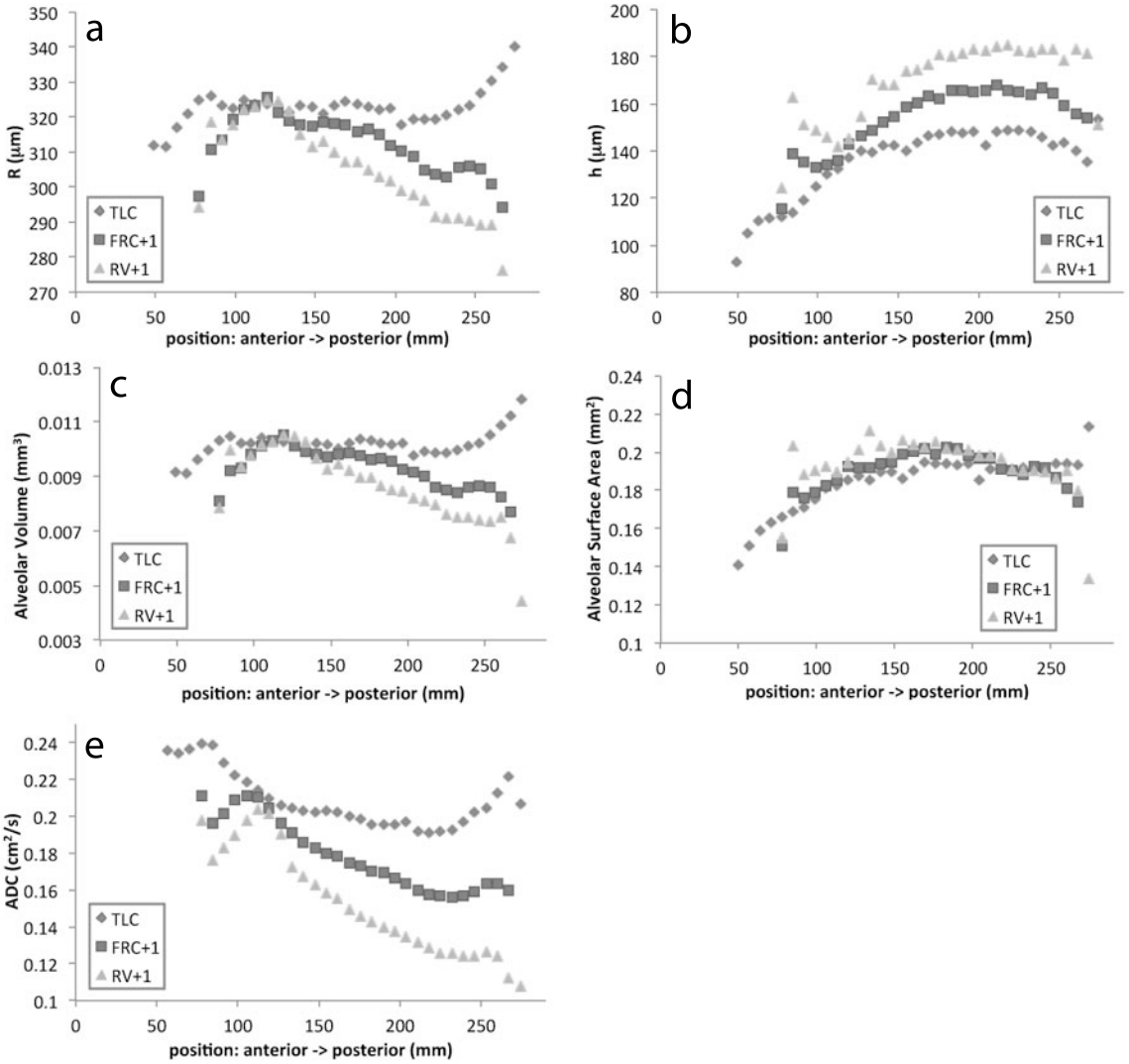

Figure 6.9: Microgeometrical parameters obtained by ^{3}He lung morphometry plotted against position in the gravitational direction. The anterior edge of each lung was around 100 mm and the posterior edge of each lung was around 400 mm. Each data point represents a parameters value averaged over all slice of all 5 pairs of lungs. The positional dependence of each parameter is plotted for each of the 3 lung volumes, TLC, FRC+1, and RV+1. (a) Plots of average alveolar duct radius, R, versus position in the gravitational direction. (b) Plots of average alveolar depth, h, versus position. (c) Plots of average alveolar volume, V_a, versus position. (d) Plots of average alveolar surface area, S_a, versus position. (e) Plots of ADC versus position.

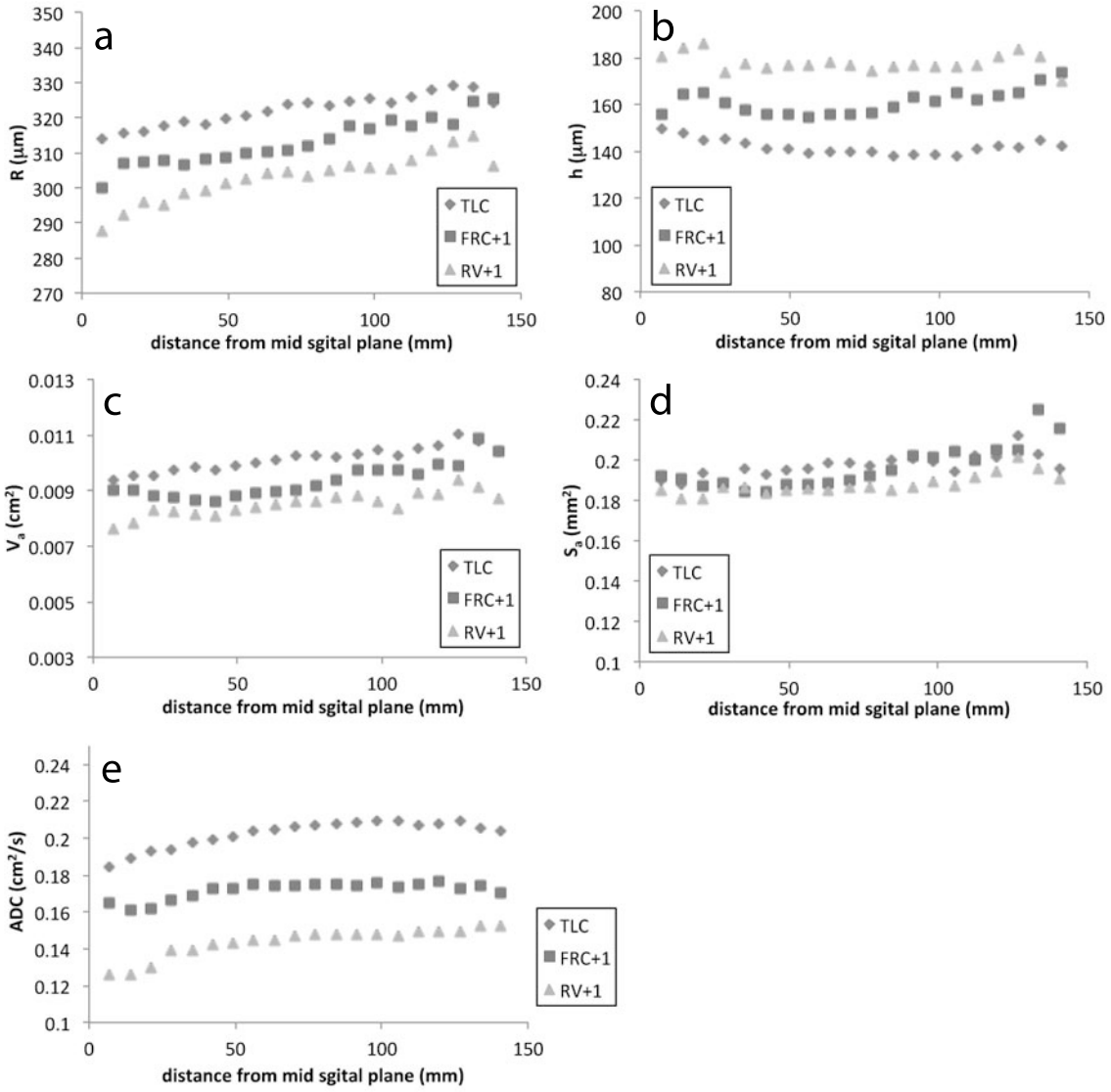

Figure 6.10: Microgeometrical parameters obtained by ^{3}He lung morphometry plotted against distance from the mid sagittal plane (medial to lateral). Each data point represents a parameters value averaged over all slices of all 5 pairs of lungs. The positional dependence of each parameter is plotted for each of the 3 lung volumes, TLC, FRC+1, and RV+1. (a) Plots of average alveolar duct radius, R, versus distance from the mid sagittal plane (medial to lateral). (b) Plots of average alveolar depth, h, versus distance from the mid sagittal plane. (c) Plots of average alveolar volume, V_a, versus distance from the mid sagittal plane. (d) Plots of average alveolar surface area, S_a, versus distance from the mid sagittal plane. (e) Plots of ADC versus distance from the mid sagittal plane.

6.3 Explanted Human ^{3}He Lung Morphometry Results

After excluding imaging voxels containing large airways or with insufficient SNR, the human morphometric model was fit to the signal attenuated explanted lung images on a voxel-by-voxel basis. The total number of alveoli, N_{tot}, and the average values of R, h, V_a, S_a, and ADC for each lung at each of the three levels of deflation are given in Table 6.6. On average a 52% decrease in total lung gas volume led to a 6% decrease in R, and 12% increase in h, a 19% decrease in V_a, a 69% decrease in N_{tot}, and an 18% decrease in ADC. There was not significant change in S_a across the three volumes.

Table 6.6: ^{3}He Lung Morphometry Explanted Human Lung Results

	Volume (L)	R (μm)	h (μm)	V_a (mm^3x10^{-3})	S_a (mm^2x10^{-2})	N_{tot} (10^6)	ADC (cm^2/s)
Lung 1							
HV	3.04	319±15	115±26	9.8±1.3	16.4±2.4	310	0.23±0.03
MV	2.23	314±19	109±26	9.4±1.8	15.6±3.0	238	0.23±0.03
LV	1.43	304±23	116±36	8.6±2.1	15.5±4.2	167	0.22±0.04
Lung 2							
HV	1.86	289±14	151±17	7.3±0.9	16.8±1.6	253	0.16±0.02
MV	1.16	271±17	172±20	5.8±0.9	16.6±2.0	192	0.11±0.02
LV	0.81	268±17	177±21	5.8±0.9	16.6±2.1	138	0.10±0.02
Lung 3							
HV	1.81	316±23	108±29	9.6±2.0	15.6±0.3	188	0.23±0.05
MV	1.47	309±36	101±33	9.0±2.8	14.6±3.0	164	0.23±0.05
LV	1.01	297±43	126±48	7.2±1.9	15.2±2.3	140	0.21±0.05
Average							
HV	2.24±0.70	308±16	125±23	8.9±1.4	16.3±0.6	250±61	0.21±0.05
MV	1.62±0.55	297±23	127±39	8.2±1.8	15.7±0.8	198±37	0.19±0.07
LV	1.08±0.32	285±19	140±33	7.2±1.4	15.5±1.1	148±16	0.18±0.06

Values for total lung gas volume, alveolar duct radius, R, alveolar depth, h, alveolar volume, V_a, alveolar surface area, S_a, total number of alveoli, N_{tot}, and apparent diffusion coefficient, ADC, for explanted human lungs 1 - 3 at High Volume (HV), Medium Volume (MV), and Low Volume (LV) averaged over all voxels. Values are reported as average ± SD. The last three rows are averages of mean results from all lungs ± SD in the means.

6.4 Dynamic Human *In vivo* ^{3}He Lung Morphometry Results

Figure 6.11 shows a typical plot of inspired gas volume over the duration of the two dynamic 6-b diffusion scans (approximately 32 s) as measured by the pneumotachometer. The plot plateaus as the subject reaches TLC and awaits the termination of the first scan sequence and the commencement of the second. For subjects 2 and 3 the total inhaled gas volume measured by the pneumotachometer was within 1% of the difference in lung volumes at TLC and RV as measured from the proton images. Subject 1 started inspiration from 0.5 L above RV and stopped inspiration 0.5 L below TLC.

Figure 6.12a shows a typical set of one-dimensional projections of both right and left lungs for each of the 6 b-values. Figure 6.12b shows the net diffusion attenuated signal from those same one-dimensional projections and the corresponding fit of the morphometric model to the data.

The morphometric parameters R and h are plotted as a function of total lung gas volume during both inflation and deflation in Figure 6.13 for subjects 1-3. The error bars represent the 67% confidence interval for the model's fit to the data. Results for which the fitting confidence was poor were excluded from the plots. There is also potential error in the total lung gas volume measurements not shown in these plots. While the pneumotachometer records very precise values for inspired gas volume, synchronization of the volume curve with the MR scan acquisition times was done manually under the assumption that the first MR scan was acquired simultaneously with the beginning of inspiration. A delay in the commencement of inspiration would lead to an error propagated to all inspired volume measurements. This delay is likely no more than 0.5 s corresponding to a potential offset in the volume measurements of up to 175 mL ± 50 mL.

The average alveolar surface area, S_a, and total number of alveoli, N_{tot}, are plotted as a function of total lung gas volume for all three subjects in Figure 6.14.

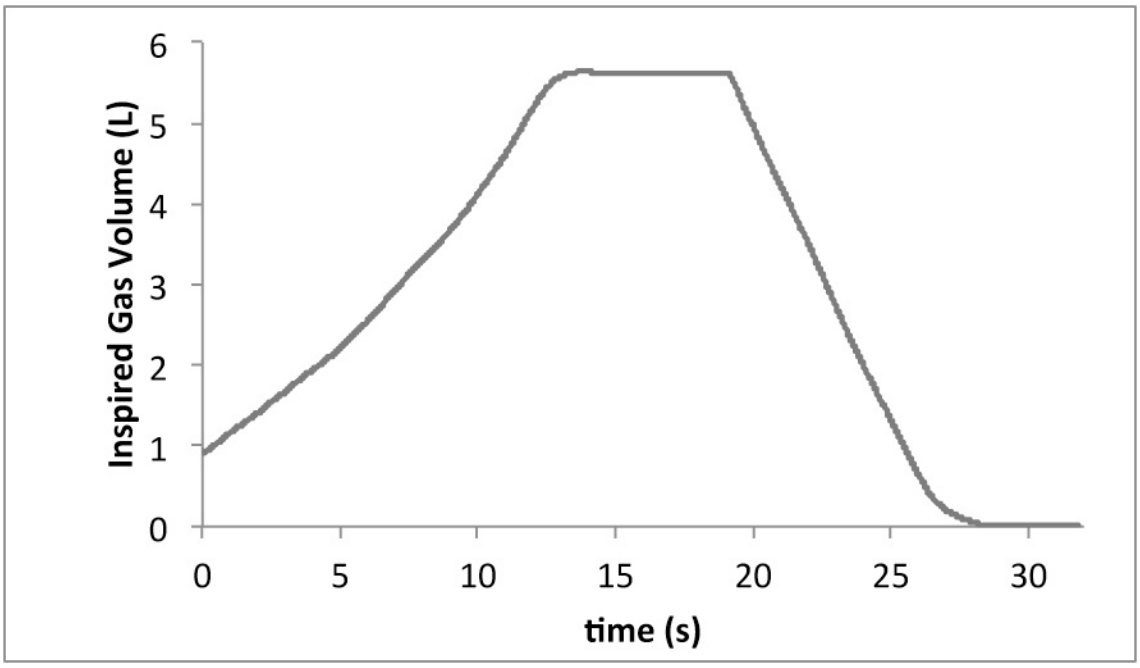

Figure 6.11: Inspired gas volume over the duration of the two dynamic 6-b diffusion scans.

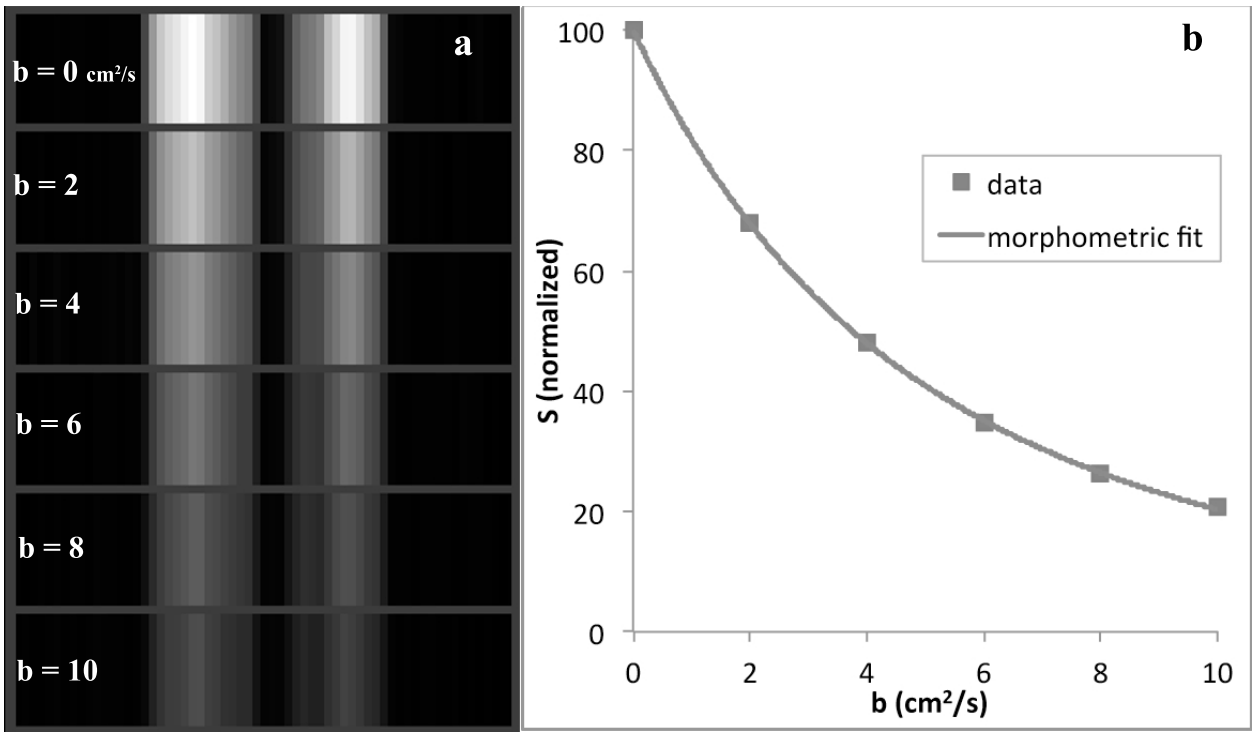

Figure 6.12: (a) signal attenuated one-dimensional projections of left and right lungs for b = 0, 2, 4, 6, 8, 10 cm^2/s (top to bottom). (b) Plot of net signal from the projections in (a) as a function of the diffusion gradient parameter *b* along with the corresponding fit from Eq. 2.3.

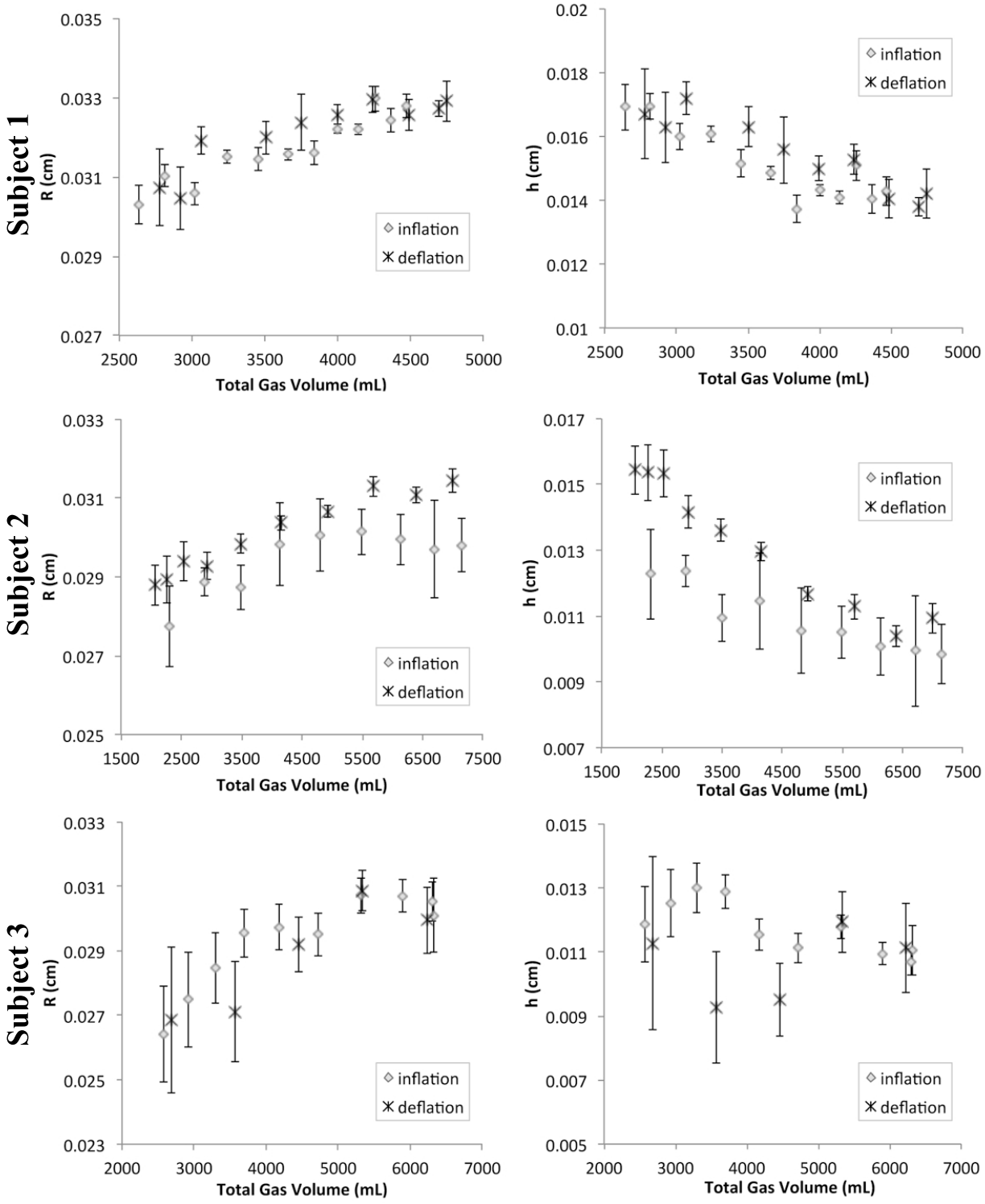

Figure 6.13: Plots of *R* (left) and *h* (right) as a function of total lung gas volume for subjects 1-3 (top to bottom). The error bars represent the 67% confidence interval for the human morphometric model's fit to the data.

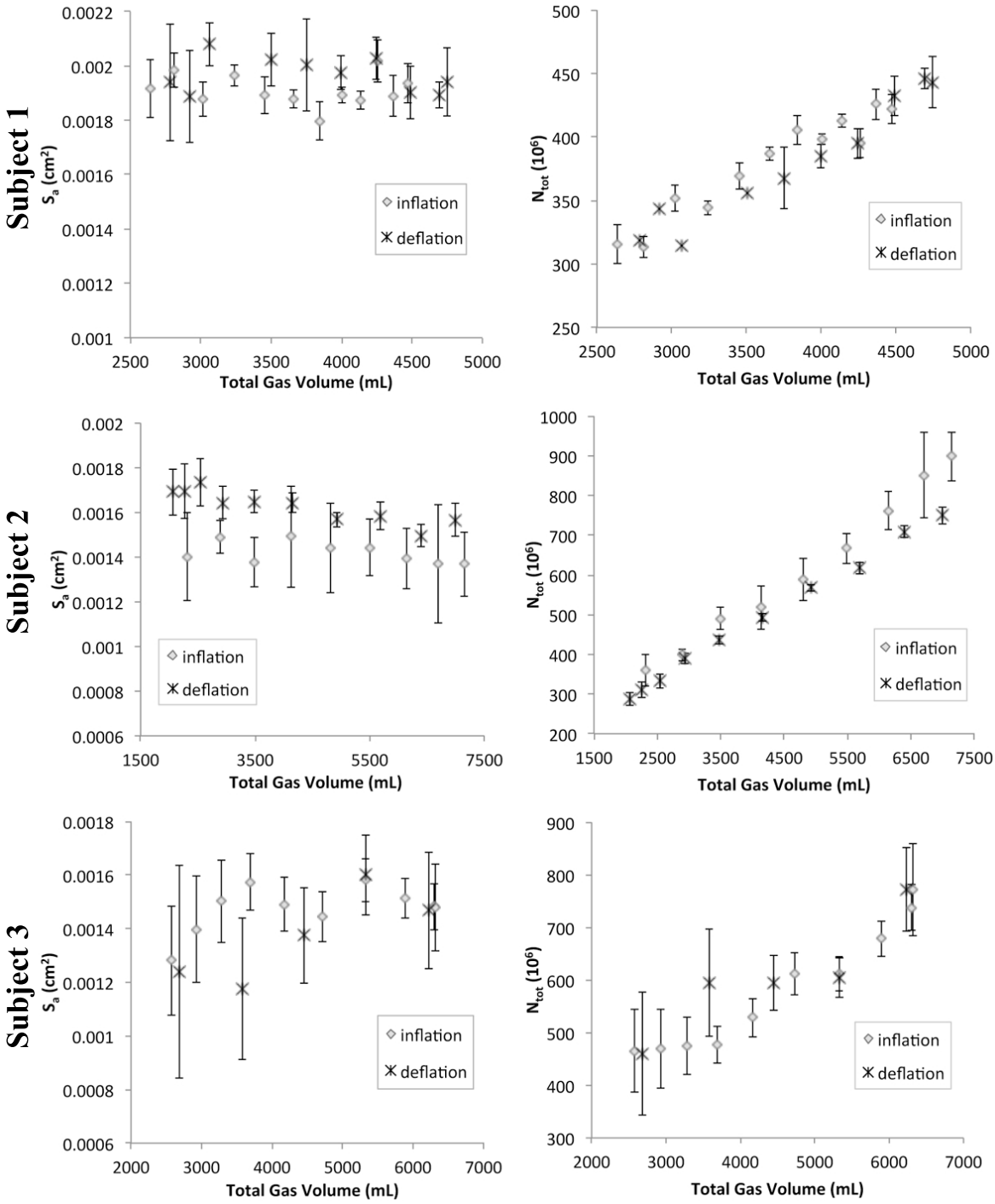

Figure 6.14: Alveolar Surface area, S_a (left), and total number of alveoli, N_{tot} (right), plotted as a function of total lung gas volume for subjects 1-3 (top to bottom). The error bars represent the propagated fitting error for the morphometric parameters R and h.

Chapter 7: Discussion and Conclusions

^{3}He lung morphometry holds many important advantages over both histology and subpleural microscopy in studying lung microstructure. MR data are obtained here from voxels each containing hundreds of acinar airways. Histological measurements, which are generally taken from hundreds of acinar airways over the course of many hours, only represent a relatively few 6-micron slices of tissue, and are naturally not volume averages--in contrast to MRI data. Our model takes into account the signal from all acinar airways within each voxel and accounts for the three-dimensionality of the airway network. Voxels are large enough to contain a sufficient number of airways to ensure a uniform distribution of orientations and to ensure that most voxels contain sufficient signal to fit the appropriate morphometric model to the data. Voxels are also small enough to perform regional analysis from the images and exclude large (non-acinar) airways from the analysis. In addition, because hyperpolarized ^{3}He gas is inert and has a very low solubility in lung tissue, the technique is suitable and safe for *in-vivo* human studies (34).

7.1 Explanted Canine Lungs

The average 18% decrease in R measured with ^{3}He lung morphometry indicates that there is a 40% decrease in alveolar volume from full inflation to deflation. This change in alveolar volume is similar to the average 46% decrease in macroscopic lung volume suggesting that the change in volume of explanted canine lungs during deflation results primarily from a change in the size of the individual alveolar ducts. Additionally, the total number of alveoli at each of the three levels of deflation showed no significant differences

between the three different lung volumes, which implies that derecruitment does not play a significant role in deflation in explanted canine lungs.

These findings are supported by those of Storey and Staub (55) and Forrest (20). Forrest showed that, in guinea pigs, the mean alveolar duct diameter was 29% smaller in nearly collapsed lungs than in fully inflated lungs. Storey reported that, in rapidly frozen cat lungs, alveolar duct diameters were 26% smaller at low levels of lung inflation than at high levels of inflation. Our own histological results showed a 20% decrease and our MR results showed a 18% decrease in alveolar duct diameter from high volume to low volume, which is in good agreement with Forrest's and Storey and Staub's results. Additionally, the 9% increase in *h* during deflation is supported by Macklin's observation that alveoli change "from the shape of a cup to that of a saucer" during inspiration (36). This is consistent with an accordion-like model for acinar airway expansion in which the alveolar ducts become wider and longer while the alveolar depth becomes more shallow (29, 36).

7.2 *In vivo* Human Lungs at Static Volumes

Explanted dog lungs were chosen in the first part of this study because they were available from unrelated cardiac experiments, could be imaged at reproducible pressures, and could be frozen for histological comparison with MR data. However, the explanted canine study still leaves three open questions: 1) how do lung micromechanics differ between canines and humans, 2) what differences exist in lung micromechanics between explanted and *in vivo* lungs, and 3) how do lung micromechanics differ at different points in the breathing cycle? Addressing all of these questions at once, the second part of this study investigates alveolar mechanics in *in vivo* human lung during inflation.

The results in Figure 6.7c show that, in *in vivo* human lungs, alveolar surface area changes very little during lung inflation. This and the decrease in alveolar depth, h, in Figure 6.7a suggest an accordion-like extension of alveolar ducts during lung inflation. This conclusion is in agreement with the explanted canine lung results in which alveolar depth increased during deflation as well as by the observations of Macklin (36) and Klingele and Staub (29). However, this change in alveolar shape results in only a 19% increase in alveolar volume (see Figure 6.7b) while the total lung volume increases by 143%. Based on these results, the small increase in alveolar volume cannot account for the large increase in total lung volume. In fact, our results in Figure 6.7d show a large increase in the number of alveoli, on average from 293 million at RV+1 to 572 million at TLC, suggesting that recruitment of new alveoli plays the more significant role in *in-vivo* lung inflation in humans.

Recall from Chapter 3 that the total alveolar surface area, S_{tot}, can be related to total lung volume, V_{tot}, by the simple power function given in Eq. 3.1, $S_{tot} = kV_{tot}^{n}$, where each of the five mechanisms for lung inflation discussed in Chapter 3 results in a different value of the exponent, n. Isotropic changes in alveolar dimensions would result in $n = 2/3$, "cup-to-saucer" like change in alveolar shape would result in $n < 2/3$, "accordion-like extension" of alveolar ducts would result in $n = 0$, and alveolar recruitment would result in $n = 1$. Recall also that while a given volume change mechanism results in a particular value of the exponent n, the converse is not true. A combination of several volume change mechanisms would result in an intermediate value of n.

Perhaps this flaw in the interpretation of morphometric measurements using Eq. 3.1 explains some of the historical discrepancies in conclusions regarding lung micromechanics. Many of the early studies of pulmonary micromechanics concluded that alveoli expand

isotropically based on surface area measurements determined by the mean linear intercept method (15, 16, 55). Fitting Eq. 3.1 to their data, they obtained values of $n \approx 2/3$ and concluded that alveolar ducts expand isotropically. However, their findings could also be explained by a combination of alveolar recruitment ($n = 1$) and a "cup-to-saucer" like change in the shape of alveolar ducts ($n < 2/3$). The relationship between total lung surface area and total lung volume does not, by itself, distinguish between these two possibilities. For example, fitting Eq. 3.1 to the *in vivo* human ^{3}He lung morphometry results in Figure 6.8 results in $n = 0.69$. This result agrees with results of Dunnill (15), D'Angelo (16), and Flicker and Lee (19) who all conclude that lungs inflate by isotropic expansion of alveolar ducts. However, in *in vivo* human lungs a substantial increase in the total number of open alveoli, a decrease in alveolar depth, and constant alveolar surface area during lung inflation were observed, indicating that the lung inflates by a combination of recruitment and accordion-like expansion of alveolar ducts rather than simply by isotropic expansion of alveolar ducts.

7.3 Explanted Human Lungs

Due to the high demand of healthy human lungs for lung transplantation (and a lack of "purpose bred humans"), healthy explanted human lungs were in short supply. Nevertheless, even the small sample of explanted human lung attained for this study provides a clear distinction between alveolar mechanics in canine lungs and alveolar mechanics in human lungs. The explanted human lungs were prepared, ventilated, and imaged in exactly the same way as the canine lung. The morphometric analysis was also nearly identical differing only in that the canine images were analyzed with the canine model and the human

images with the human model. The human explanted lung results, however, are much more similar to the results obtained from the *in vivo* human lung inflation experiments discussed in the previous section. As with the *in vivo* human results, the relatively small change in the alveolar duct radius suggests a large change in the number of open alveoli, supporting the theory that alveolar recruitment/derecruitment is the dominant mechanism for lung volume change in human lungs.

7.4 Dynamic ^{3}He Lung Morphometry

The results from the dynamic ^{3}He morphometry experiments address the final question concerning difference in lung micromechanics at different points in the breathing cycle. A typical sketch of an explanted lung pressure volume curve is shown in Figure 7.1 (64). The hysteresis in this curve is due to energy lost in the breathing process. If the process of recruitment and derecruitment is triggered by opening and closing pressures, as suggested by Albert *et al* (2), then it would be reasonable to expect that the number of alveoli might follow a similar hysteresis to that of pressure in the pressure-volume curve in Figure 7.1b.

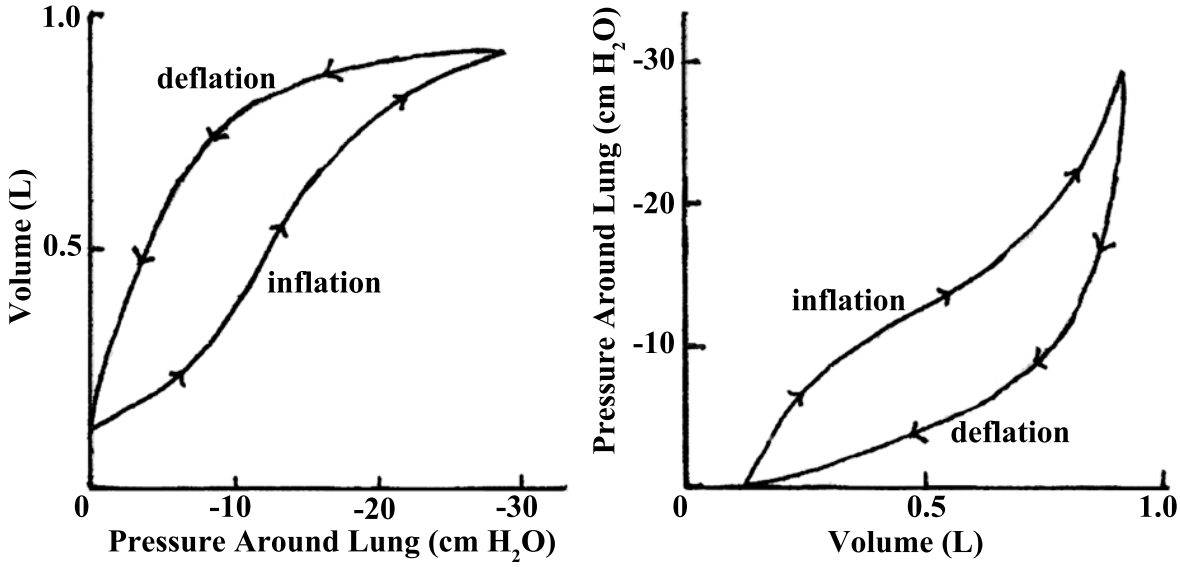

Figure 7.1: Sketch of a typical Pressure-Volume curve (Left). The same Pressure-Volume curve is also plotted on the right with the axes switched so that total lung gas volume is plotted on the horizontal axis.

Additionally, the dynamic ^{3}He lung morphometry results address whether the same mechanism (or combination of mechanisms) responsible for lung volume change at low lung volumes is equally important at medium and high lung volumes. Using stereological measurements and the lung surface area-volume power function of Eq. 3.1, Gil *et al* observed an increasing slope of the log(S)-log(V) curve with increasing lung volume. They thus concluded that the lung expands by 1) accordion-like extension of alveolar ducts at low lung volumes, 2) isotropic expansion of alveolar ducts at medium lung volumes, and 3) alveolar recruitment at high lung volumes (23). Gil's observations are, however, not supported by the dynamic ^{3}He morphometry results presented here. In subjects 1 and 2 the rate of increase in the number of alveoli is nearly constant throughout both the inflation and deflation legs suggesting that recruitment/derecruitment is equally important at all points in the breathing cycle. The fitting error in the results from subject 3 makes it difficult to draw any

conclusions from those results. There is also no consistent change in the alveolar surface area between any points during either inflation or deflation in any of the three subjects, suggesting that accordion-like extension of alveolar ducts is also present throughout the breathing cycle.

The question of hysteresis in alveolar recruitment/derecruitment is not clearly answered by these results. While there appears to be a slight difference in the number of open alveoli between inflation and deflation in subjects 1 and 2, the fitting error is too large to make this conclusion with confidence.

The results presented here represent the first time ^{3}He lung morphometry has been used to investigate alveolar geometry throughout both the inflation and deflation legs of the breathing cycle. After conducting these experiments, a number of potential improvements to the experimental methods became clear.

Firstly, in most cases data collected at the lowest lung volumes were discarded because of poor fitting confidence due to low SNR. The small amount of ^{3}He present in the lungs at these volumes was simply insufficient to provide the required SNR to confidently fit the morphometric model to the data. Starting the inflation scan sequence with larger flip angles and gradually decreasing the flip angle as the lung inflates with ^{3}He (and vice-versa for the deflation scan sequence) would potentially resolve this issue.

Secondly, the second scan sequence (deflation for subjects 1 and 3, inflation for subject 2) always produced lower SNR and correspondingly poorer fitting confidence. As discussed in section 5.1, the non-renewable ^{3}He polarization is depleted with each rf pulse. After the first scan sequence (13 time points x 6 b-values = 65 pulses), the ^{3}He polarization is reduced substantially. A simple solution to this problem would be to use smaller flip angles

for the scan sequence over the first leg of the breathing cycle and larger flip angle for the scan sequence over the second leg of the breathing cycle.

Lastly, error in the volume measurements could be greatly reduced by a better method for synchronizing the pneumotachometer measurement with MR scan times. This could be accomplished by simply having a research assistant start the pneumotachometer simultaneously with the commencement of the first scan sequence.

7.5 Differences Between Human and Canine Lungs

The results from the *in vivo* static human lung inflation images, the explanted human lung deflation images, and the dynamic human lung MR scans during the inflation and deflation legs of the breathing cycle are all in very good agreement with each other. In all cases, changes in lung volume between around RV and around TLC resulted in similar changes in alveolar duct radius, alveolar depth, alveolar volume, and *ADC*. Additionally, all sets of experiments showed no significant change in alveolar surface area across different lung volumes and a large change in the number of open alveoli between RV and TLC. These results clearly indicate the human lungs inflate and deflate predominately by alveolar recruitment/derecruitment as well as, to a smaller extent, by accordion-like extension of alveolar ducts.

While the increase in alveolar depth with decreasing lung volume in canine lungs supports the theory of accordion-like deformations of alveolar ducts, the large increase in alveolar duct radius lends an incongruous piece to the lung micromechanics puzzle. The 40% decrease in alveolar volume from high lung volume to low lung volume suggests that derecruitment is not an important mechanism for deflation in canine lungs.

One possible explanation for the discrepancies in the canine and human results is that lung micromechanics are simply different in the two species. Dunnill, an early pioneer in alveolar mechanics research, studied deflation in explanted canine lungs and also concluded that canine lungs deflate predominantly due to a decrease in alveolar volume (15). Dunnill, however, reached this conclusion after fitting the flawed powered function in Eq. 3.1 to stereological measurements of lung surface area and lung volume. Furthermore, several more recent studies of lung micromechanics in *in vivo* canine lungs strongly support the theory of alveolar recruitment as the dominant mechanism for changes in lung volume (9, 14, 47, 53).

7.6 ^{3}He Costs

One major drawback of ^{3}He NMR is the rising cost and limited availability of ^{3}He gas. For this reason, some hyperpolarized gas researchers are turning to ^{129}Xe as a potential alternative to ^{3}He. While ^{129}Xe may become an adequate substitute for ^{3}He in ventilation and, in some cases, 2-b diffusion experiments, MRI gas diffusion morphometry is one area where the exceedingly high SNR produced with ^{3}He is necessary and, at this time, cannot be matched by ^{129}Xe. While rising costs are an obstacle to the introduction of ^{3}He into clinical environments, vigorous efforts are currently underway to implement ^{3}He recycling programs, and collaborate with other industries which use ^{3}He in order to manage usage and costs. While these efforts will likely have a major impact on the cost and availability of ^{3}He in the future, even now, ^{3}He lung morphometry remains a valuable research tool in furthering our understanding of lung physiology and disease.

7.7 Summary

In the first part of this study, morphological measurements of acinar airways from canine lungs at various levels of deflation were obtained via ^{3}He lung morphometry. In order to substantiate the MR results two pairs of the lungs were frozen, each at different levels of deflation, for histological comparison. The imaging data indicate that in canine lungs alveolar depth, *h*, increases slightly during deflation, and that changes in alveolar duct volume are the primary mechanism affecting macroscopic changes in total lung volume; this is validated via histological finding in the same lungs.

In the second part of this study, ^{3}He lung morphometry was employed to measure changes in alveolar geometry during inflation in *in-vivo* human lungs. The results indicate that in humans during inspiration alveolar duct radii increase only slightly, with a more significant decrease in alveolar depth, and a large increase in the number of open alveoli. These findings suggest that, during inflation, the total lung volume increases largely by alveolar recruitment, with a smaller contribution from accordion-like extension of alveolar ducts. It was also shown that lung volume changes viewed only through the lens of standard morphological techniques could potentially be misinterpreted.

The ^{3}He lung morphometry results from the *in vivo* human experiments are in very good agreement with the ^{3}He lung morphometry experiments in explanted human lungs and with results from a new dynamic ^{3}He lung morphometry technique which measured morphometric parameters throughout both the inflation and deflation legs of a breathing cycle in human subjects. Together these results show that, in human lungs, there is not a significant difference in the mechanism of volume change at the alveolar level between excised and *in vivo* lungs or at different points in the breathing cycle.

These findings help to illuminate the mechanisms for lung volume change within the most fundamental pulmonary unit--- the alveolar ducts.

References

1. **Albert MS, Balamore D**. Development of hyperpolarized noble gas MRI. *Nucl Instrum Methods Phys Res A* 402: 441-53, 1998.

2. **Albert SP, DiRocco J, Allen GB, Bates JH, Lafollette R, Kubiak BD, Fischer J, Maroney S, Nieman GF**. The role of time and pressure on alveolar recruitment. *J Appl Physiol* 106: 757-765, 2009.

3. **Armstrong JD, Gluck EH, Crapo RO, Jones HA, Hughes JM**. Lung tissue volume estimated by simultaneous radiographic and helium dilution methods. *Thorax* 37: 676-679, 1982.

4. **Babcock E**. Spin-exchange optical pumping with alkali-metal vapors. *Exchange Organizational Behavior Teaching Journal* University of Wisconsin. 2005.

5. **Bachofen H, Schürch S, Urbinelli M, Weibel ER**. Relations among alveolar surface tension, surface area, volume, and recoil pressure. *J Appl Physiol* 62: 1878-1887, 1987.

6. **Berg HC**. *Random Walks in Biology*. Princeton University Press, 1993.

7. **Bloch F**. Nuclear Induction. *Physical Review* 70: 460-474, 1946.

8. **Callaghan P**. *Principles of Nuclear Magnetic Resonance Microscopy*. Oxford University Press, USA, 1994.

9. **Carney DE, Bredenberg CE, Schiller HJ, Picone AL, McCann UG, Gatto LA, Bailey G, Fillinger M, Nieman GF**. The Mechanism of Lung Volume Change during Mechanical Ventilation. *Am J Respir Crit Care Med* 160: 1697-1702, 1999.

10. **Chen W, Gentile T, Walker T, Babcock E**. Spin-exchange optical pumping of ^{3}He with Rb-K mixtures and pure K. *Phys Rev A* 75: 1-14, 2007.

11. **Chen XJ, Hedlund LW, Möller HE, Chawla MS, Maronpot RR, Johnson GA**. Detection of emphysema in rat lungs by using magnetic resonance measurements of ^{3}He diffusion. *Proceedings of the National Academy of Sciences of the United States of America* 97: 11478-81, 2000.

12. **Ciullo G., Contalbrigo M. LP**, editor. *Polarized Sources, Targets and Polarimetry: Proceedings of the 13th International Workshop*. World Scientific Publishing Company, 2011.

13. **Deslee G, Woods JC, Moore CM, Liu L, Conradi SH, Milne M, Gierada DS, Pierce J, Patterson A, Lewit RA, Battaile JT, Holtzman MJ, Hogg JC, Pierce RA**. Elastin expression in very severe human COPD. *Eur Respir J* 34: 324-31, 2009.

14. **Dirocco J, Carney D, Nieman G**. The Mechanism of Ventilator-induced Lung Injury : Role of Dynamic Alveolar Mechanics. *Yearbook of Intensive Care and Emergency Medicine* 2005: 80-92, 2005.

15. **Dunnill MS**. Effect of Lung Inflation on Alveolar Surface Area in the Dog. *Nature* 214: 1013-1014, 1967.

16. **D'Angelo E**. Local alveolar size and transpulmonary pressure in situ and in isolated lung. *Respir Physiol* 14: 251–266, 1972.

17. **Farrar TC**. *Introduction to Pulse Nmr Spectroscopy*. Farragut Pr, 1989.

18. **Fichele S, Paley MNJ, Woodhouse N, Griffiths PD, van Beek EJR, Wild JM**. Investigating ^{3}He diffusion NMR in the lungs using finite difference simulations and in vivo PGSE experiments. *J Magn Reson* 167: 1-11, 2004.

19. **Flicker E**. Equilibrium of force of subpleural alveoli: implications to lung mechanics. *J Appl Physiol* 36: 366-374, 1974.

20. **Forrest JB**. The effect of changes in lung volume on the size and shape of avleoli. *J Physiol* 210: 533-547, 1970.

21. **Fukushima E, Roeder S**. *Experimental Pulse NMR: A Nuts and Bolts Approach*. Westview Press, 1993.

22. **Gierada DS, Woods JC, Bierhals AJ, Bartel S-ET, Ritter JH, Choong CK, Das NA, Hong C, Pilgram TK, Chang YV, Jacob RE, Hogg JC, Battafarano RJ, Cooper JD, Meyers BF, Patterson GA, Yablonskiy DA, Conradi MS**. Effects of diffusion time on short-range hyperpolarized ^{3}He diffusivity measurements in emphysema. *J Magn Reson Imaging* 30: 801-808, 2009.

23. **Gil J, Bachofen H, Gehr P, Weibel ER**. Alveolar volume-surface area relation in air- and saline-filled lungs fixed by vascular perfusion. *J Appl Physiol* 47: 990-1001, 1979.

24. **Greaves IA, Hildebrandt J, Hoppin Jr FG**. Micromechanics of the lung. In: *Handbook of Physiology. The Respiratory System Volume 3*. Bethesda, MD: Am Physiol Soc, 1986, p. 217-231.

25. **Haefeli-Bleuer B, Weibel ER**. Morphometry of the Human Pulmonary Acinus. *Anat Rec* 220: 401-414, 1988.

26. **Hajari AJ, Yablonskiy DA, Quirk JD, Sukstanskii AL, Pierce RA, Deslée G, Conradi MS, Woods JC**. Imaging alveolar-duct geometry during expiration via ^{3}He lung morphometry. *J Appl Physiol* 110: 1448-54, 2011.

27. **Hajari AJ, Yablonskiy DA, Sukstanskii AL, Quirk JD, Conradi MS, Woods JC**. Morphometric changes in the human pulmonary acinus during inflation. *J Appl Physiol* 112: 937-43, 2012.

28. **Kittel C**. *Introduction to Solid State Physics*. Wiley, 2004.

29. **Klingele TG, Staub NC**. Alveolar shape changes with volume in isolated, air-filled lobes of cat lung. *J Appl Physiol* 28: 411-414, 1970.

30. **Leawoods JC**. Novel Applications of Hyperpolarized Gases. *Chemical Physics Letters* Washington University. 2002.

31. **Levenberg K**. A method for the solution of certain problems in least squares. *Quarterly of Applied Mathematics* 2: 164 - 168, 1944.

32. **Levitt MH**. *Spin Dynamics: Basics of Nuclear Magnetic Resonance*. Chichester, West Sussex: John Wiley & Sons, 2008.

33. **Lum H, Huang I, Mitzner W**. Morphological evidence for alveolar recruitment during inflation at high transpulmonary pressure. *J Appl Physiol* 68: 2280-6, 1990.

34. **Lutey BA, Lefrak SS, Woods JC, Tanoli T, Quirk JD, Bashir A, Yablonskiy DA, Conradi MS, Bartel S-ET, Pilgram TK, Cooper JD, Gierada DS**. Hyperpolarized ^{3}He MR imaging: physiologic monitoring observations and safety considerations in 100 consecutive subjects. *Radiology* 248: 655-661, 2008.

35. **Macklem PT**. Respiratory mechanics. *Annu Rev Physiol* 40: 157-84, 1978.

36. **Macklin C**. The alveoli of the mammalian lung: An anatomical study with clinical correlations. *Proc Inst Med Chic* 18: 78-95, 1950.

37. **Marquardt DW**. An Algorithm for Least-Squares Estimation of Nonlinear Parameters. *J. Soc. Ind. Appl. Math* 11: 431-441, 1963.

38. **Mata JF, Altes TA, Cai J, Ruppert K, Mitzner W, Hagspiel KD, Patel B, Salerno M, Brookeman JR, de Lange EE, Tobias WA, Wang H-TJ, Cates GD, Mugler JP**. Evaluation of emphysema severity and progression in a rabbit model: comparison of hyperpolarized 3He and 129Xe diffusion MRI with lung morphometry. *J Appl Physiol* 102: 1273-80, 2007.

39. **Matsuoka S, Patz S, Albert MS, Sun Y, Rizi RR, Gefter WB, Hatabu H**. Hyperpolarized gas MR Imaging of the lung: current status as a research tool. *J Thorac Imaging* 24: 181-8, 2009.

40. **Mercer RR, Russell ML, Crapo JD**. Alveolar septal structure in different species. *J Appl Physiol* 77: 1060-1066, 1994.

41. **Milne ML**. Exploring Tissue Microstructure in Healthy and Diseased Lung Tissue. Washington University. 2010.

42. **Ochs M, Nyengaard JR, Jung A, Knudsen L, Voigt M, Wahlers T, Richter J, Gundersen HJG**. The number of alveoli in the human lung. *Am J Respir Crit Care Med* 169: 120-4, 2004.

43. **Osmanagic E, Sukstanskii a L, Quirk JD, Woods JC, Pierce R a, Conradi MS, Weibel ER, Yablonskiy D a**. Quantitative assessment of lung microstructure in healthy mice using an MR-based ^{3}He lung morphometry technique. *J Appl Physiol* 109: 1592-9, 2010.

44. **Patz S, Muradian I, Hrovat M, Ruset I**. Human Pulmonary Imaging and Spectroscopy with Hyperpolarized 129Xe at 0.2T. *Acad Radiol* 15: 713-727, 2008.

45. **Patz S, Muradyan I, Hrovat MI, Dabaghyan M, Washko GR, Hatabu H, Butler JP**. Diffusion of hyperpolarized 129Xe in the lung: a simplified model of 129Xe septal uptake and experimental results. *New J Phys* 13, 2011.

46. **Peces-Barba G, Ruiz-Cabello J, Cremillieux Y, Rodriguez I, Dupuich D, Callot V, Ortega M, Rubio Arbo ML, Cortijo M, Gonzalez-Mangado N**. Helium-3 MRI diffusion coefficient: correlation to morphometry in a model of mild emphysema. *European Respiratory Journal* 22: 14-19, 2003.

47. **Pelosi P, Goldner M, McKibben A, Adams A, Eccher G, Caironi P, Losappio S, Gattinoni L, Marini JJ**. Recruitment and derecruitment during acute respiratory failure: an experimental study. *Am J Respir Crit Care Med* 164: 122-30, 2001.

48. **Quirk JD, Lutey BA, Gierada DS, Woods JC, Senior RM, Lefrak SS, Sukstanskii AL, Conradi MS, Yablonskiy DA**. In vivo detection of acinar microstructural changes in early emphysema with ^{3}He lung morphometry. *Radiology* 260: 866-74, 2011.

49. **Saam BT, Yablonskiy DA, Kodibagkar VD, Leawoods JC, Gierada DS, Cooper JD, Lefrak SS, Conradi MS**. MR imaging of diffusion of ^{3}He gas in healthy and diseased lungs. *Magn Reson Med* 44: 174-9, 2000.

50. **Schreider JP, Raabe OG**. Structure of the human respiratory acinus. *Am J Anat* 162: 221-32, 1981.

51. **Shea DA, Morgan D**. *The Helium-3 Shortage: Supply, Demand, and Options for Congress*. 2010.

52. **Slichter CP**. *Principles of Magnetic Resonance*. Springer, 1990.

53. **Smaldone GC, Mitzner W, Itoh H**. Role of alveolar recruitment in lung inflation: influence on pressure-volume hysteresis. *J Appl Physiol* 55: 1321–1332, 1983.

54. **Stejskal E, Tanner J**. Spin Diffusion Measurements: Spin Echoes in the Presence of a Time-Dependent Field Gradient. *J Chem Phys* 42: 288, 1965.

55. **Storey WF, Staub NC**. Ventilation of terminal air units. *J Appl Physiol* 17: 391-7, 1962.

56. **Sukstanskii AL, Conradi MS, Yablonskiy DA**. ^{3}He lung morphometry technique: accuracy analysis and pulse sequence optimization. *J Magn Reson* 207: 234-41, 2010.

57. **Sukstanskii AL, Yablonskiy DA**. In vivo lung morphometry with hyperpolarized ^{3}He diffusion MRI: theoretical background. *J Magn Reson* 190: 200-210, 2008.

58. **Torrey HC**. Bloch Equations with Diffusion Terms. *Phys Rev* 104: 563, 1956.

59. **Tsunoda S, Fukaya H, Sugihara T, Martin C, Hildebrandt J**. Lung Volume, Thickness of Alveolar Walls, and Microscopic Anisotropy of Expansion. *Respir Physiol* 22: 285–296, 1974.

60. **Wagshul M, Chupp TE**. Laser optical pumping of high-density Rb in polarized ^{3}He targets. *Phys Rev A* 49: 3854-3869, 1994.

61. **Walker TG, Happer W**. Spin-exchange optical pumping of noble-gas nuclei. *Rev Modern Phys* 69: 629-642, 1997.

62. **Wang W, Nguyen NM, Yablonskiy D a, Sukstanskii AL, Osmanagic E, Atkinson JJ, Conradi MS, Woods JC**. Imaging lung microstructure in mice with hyperpolarized ^{3}He diffusion MRI. *Magn Reson Med* 65: 620-6, 2011.

63. **Weibel ER**. *Morphometry of the human lung*. Springer-Verlag, 1963.

64. **West JB**. *Respiratory Physiology - The Essentials*. Baltimore, MD: Williams and Wilkins, 1995.

65. **Woods JC, Choong CK, Yablonskiy DA, Bentley J, Wong J, Pierce JA, Cooper JD, Macklem PT, Conradi MS, Hogg JC**. Hyperpolarized ^{3}He diffusion MRI and histology in pulmonary emphysema. *Magn Reson Med* 56: 1293-1300, 2006.

66. **Woods JC**. *Caught by Surprise : Causes and Consequences of the Helium-3 Supply Crisis*. 2010.

67. **Yablonskiy DA, Sukstanskii AL, Leawoods JC, Gierada DS, Bretthorst GL, Lefrak SS, Cooper JD, Conradi MS**. Quantitative in vivo assessment of lung microstructure at the alveolar level with hyperpolarized ^{3}He diffusion MRI. *Proc Natl Acad Sci* 99: 3111-3116, 2002.

68. **Yablonskiy DA, Sukstanskii AL, Woods JC, Gierada DS, Quirk JD, Hogg JC, Cooper JD, Conradi MS**. Quantification of lung microstructure with hyperpolarized ^{3}He diffusion MRI. *J Appl Physiol* 107: 1258-65, 2009.